FINAL REPORT

NASA GRANT NAG 9-1244

HYBRID PARTICLE-ELEMENT SIMULATION OF IMPACT ON COMPOSITE ORBITAL DEBRIS SHIELDS

submitted by

Eric P. Fahrenthold

Department of Mechanical Engineering
University of Texas
1 University Station C2200
Austin, TX 78712, USA

November 8, 2004

ABSTRACT

This report describes the development of new numerical methods and new constitutive models for the simulation of hypervelocity impact effects on spacecraft. The research has included parallel implementation of the numerical methods and material models developed under the project. Validation work has included both one dimensional simulations, for comparison with exact solutions, and three dimensional simulations of published hypervelocity impact experiments. The validated formulations have been applied to simulate impact effects in a velocity and kinetic energy regime outside the capabilities of current experimental methods. The research results presented here allow for the expanded use of numerical simulation, as a complement to experimental work, in future design of spacecraft for hypervelocity impact effects.

ACKNOWLEDGEMENTS

This work was supported by the Human Exploration Science Office (JSC-SX) of NASA Johnson Space Center. Additional support was provided by the National Science Foundation (CMS 99-12475) and the State of Texas Advanced Research Program (003658-0709-1999). Computer time support was provided NASA Ames Research Center, the Texas Advanced Computing Center at the University of Texas at Austin, and the Arctic Region Supercomputing Center at the University of Alaska Fairbanks.

The numerical methods and material model development work described here was performed in collaboration with graduate students Ravishankar Shivarama (PhD, 2002) and Young-Keun Park (PhD expected, 2004) in the Department of Mechanical Engineering at the University of Texas at Austin. All code development work was performed by the Principal Investigator (Eric P. Fahrenthold).

TABLE OF CONTENTS

INTRODUCTION

The seven chapters which follow describe numerical methods and constitutive modeling work which offers improved capabilities for the simulation of hypervelocity impact effects.

- Chapter 1 describes the development of a new hybrid-particle finite element method for hypervelocity impact simulation.
- Chapter 2 describes validation of the hybrid-particle finite element method developed in the first chapter, in simulations of published hypervelocity impact experiments.
- Chapter 3 describes validation of the hybrid-particle finite element method developed in the first chapter, in simulations of rigid body dynamics problems with known exact solutions.
- Chapter 4 describes an improved formulation of the hybrid-particle finite element method developed in the first chapter, simplifying the method and improving its computational efficiency.
- Chapter 5 describes the development of a new rate dependent elastic-plastic model for Kevlar, and its application in the simulation of hypervelocity impact effects on composite orbital debris shielding, like that deployed on the International Space Station.
- Chapter 6 describes the development of a new rate dependent anisotropic elastic-plastic model for reinforced carbon-carbon, and its application in the simulation of hypervelocity impact effects on the wing leading edge of the Space Shuttle.
- Chapter 7 describes the application of hybrid particle-finite element methods in the simulation of foam impact effects on the Space Shuttle thermal protection system.

The Conclusions section suggests opportunities for future research, and Appendix 1 tabulates some specific simulation data for reinforced carbon-carbon.

CHAPTER 1

AN ELLIPSOIDAL PARTICLE-FINITE ELEMENT METHOD FOR HYPERVELOCITY IMPACT SIMULATION

Ravishankar Shivarama[1] and Eric P. Fahrenthold[2]

Department of Mechanical Engineering, 1 University Station C2200
University of Texas, Austin, TX 78712, USA

[1]Graduate student
[2]Professor, corresponding author, phone: (512) 471-3064, email: epfahren@mail.utexas.edu

AN ELLIPSOIDAL PARTICLE-FINITE ELEMENT METHOD FOR HYPERVELOCITY IMPACT SIMULATION

Ravishankar Shivarama[3] **and Eric P. Fahrenthold**[4]

Department of Mechanical Engineering, 1 University Station C2200
University of Texas, Austin, TX 78712, USA

A number of coupled particle-element and hybrid particle-element methods have been developed for the simulation of hypervelocity impact problems, to avoid certain disadvantages associated with the use of pure continuum based or pure particle based methods. To date these methods have employed spherical particles. In recent work a hybrid formulation has been extended to the ellipsoidal particle case. A model formulation approach based on Lagrange's equations, with particles entropies serving as generalized coordinates, avoids the angular momentum conservation problems which have been reported with ellipsoidal smooth particle hydrodynamics models.

KEYWORDS: particle methods, finite element methods, impact simulation

INTRODUCTION

A review of the literature on hypervelocity impact simulation shows that most research in this field has focused on the development and application of continuum hydrocodes, using either Eulerian, Lagrangian, or Arbitrary Lagrangian-Eulerian (ALE) formulations [1,2,3]. In the last decade attention has shifted towards particle based methods [4], in particular smooth particle hydrodynamics (SPH). Although both continuum and particle based methods have demonstrated excellent results in a range of practical applications, these methods are not without problems. As a result some recent research has formulated coupled particle-element

[3]Graduate student
[4]Professor, corresponding author, phone: (512) 471-3064, email: epfahren@mail.utexas.edu

[5] or hybrid particle-element [6] methods, aimed at avoiding certain disadvantages of the use of pure continuum based methods or pure particle based methods in hypervelocity impact applications [7]. The present paper develops a generalized hybrid method, extending the work of Fahrenthold and Horban [6], presenting for the first time a combined particle-element formulation based on a nonspherical particle geometry. Nonspherical particle formulations are also of interest in certain molecular dynamics [8] and astrophysics [9,10] applications, where material or flowfield geometry has suggested the use of repulsion potentials or interpolation kernels with ellipsoidal forms.

Most previous hypervelocity impact simulation work has employed Eulerian finite volume and Lagrangian finite element methods [1,11] and more recent extensions of these methods to Arbitrary Lagrangian-Eulerian frames [12]. Although continuum hydrocodes are accurate and efficient simulation tools for many important problems, they are not well suited for use in all hypervelocity impact applications. Eulerian codes can accommodate arbitrarily general contact-impact, but their approximate models of material strength effects are best suited to a very high velocity impact regime. Lagrangian codes incorporate very accurate models of material strength effects, but their slideline based contact-impact algorithms are best suited to a relatively low velocity impact regime. ALE methods allow for intelligent tailoring of the mesh, ideally avoiding (but not eliminating) the preceding limitations.

None of the aforementioned continuum formulations is ideally suited to applications where the generation, transport, and contact-impact dynamics of material fragments is of central concern. When material fragments become much smaller than the finite volume cell size, Eulerian flow field interpolations may not accurately represent the physical state of the highly comminuted medium. Hence the adaptive introduction of a high resolution Eulerian mesh is required. Similarly the use of Lagrangian finite elements to represent a highly fragmented medium calls for the introduction of a very extensive and adaptive slideline mesh. It is not surprising that these continuum formulations can be difficult to apply in cases where fragmentation dynamics are of central interest, given the highly discontinuous nature of the

field variables in such systems.

Recognizing the disadvantages of continuum formulations in certain hypervelocity impact applications, a number of different particle methods [13,14,15] have been introduced. In general these methods replace or augment the conventional continuum kinematics with particle based interpolations, to more efficiently represent fragment generation, transport, and contact-impact effects in applications where modeling of the latter physics is of central concern. The overwhelming majority of particle based hypervelocity impact models have employed SPH techniques and spherical kernels. A notable exception is the work of Shapiro and co-workers [9,10], who extended the basic SPH method to ellipsoidal kernels. However those authors indicate that their method fails to conserve angular momentum, and they offer no solutions to the tensile instability, numerical fracture, and other problems which have hindered the effective use of SPH methods in some applications. The formulation presented here does not involve element-to-particle conversion, as discussed for example by Johnson et al. [14], who converted distorted finite elements into SPH particles. The latter conversion, if it occurs before failure of the element, may introduce the aforementioned SPH tensile instability and and numerical fracture problems.

The present paper formulates a hybrid ellipsoidal particle-finite element model for hypervelocity impact simulation. Unlike the coupled particle-element formulations of Hayhurst et al. [16] and other authors, which use particles to model some structures and finite elements to model other structures, the present paper employs particles and elements everywhere. The simultaneous use of particles and elements is not redundant, since they are used to represent distinct physics. The particles model all inertia and contact-impact effects, and are associated with interpolation functions which represent compressed states. The elements model all strength effects, namely tension and elastic-plastic shear. This approach has several advantages. The tensile instability and numerical fracture problems common to SPH formulations are avoided, since interpolation kernels are not used to represent interparticle tension forces, and since material strength effects give rise to interparticle forces only among reference con-

figuration neighbors. Although true Lagrangian kinematics are used to calculate tensile and shear forces, the use of particles in all inertia and contact-impact calculations means that material failure is simply accommodated (without element-to-particle remapping or mass and energy discard) via the loss of element cohesion. Particles not associated with any intact elements translate and rotate as individual fragments, in response to contact-impact loads. No slidelines are used, so that contact-impact of all intact and fragmented material is modeled everywhere. Although the authors do not contend that this numerical approach is best for all impact simulation problems, it offers important advantages in hypervelocity impact applications. In the latter field an interest in multi-structure perforation, erosion, fragmentation, and very general contact-impact modeling is not unusual.

The model formulation work described in the sections which follow is different from that normally employed to develop hydrocode models of either the continuum or particle type. Two particular features should be mentioned. First an energy method (Lagrange's equations) is used to develop the semi-discrete model, so that no reference is made to any partial differential equations. The introduction of entropy variables as generalized coordinates makes it possible to account for very general thermal dynamics while using a discrete Lagrangian approach. Secondly the formulation introduces Euler parameter states [17] to account for the rotational motion of the nonspherical particles. An Euler parameter description of the particle kinematics is desired in order to avoid the singularities of Euler angle based models. Although the use of Euler parameters leads nominally to a differential-algebraic formulation, the development which follows introduces momentum state variables, to reduce the order of the system and thereby eliminate the Lagrange multipliers associated with the Euler parameter constraint. The model formulation work described here therefore generalizes in a geometric sense the particle-element work of Fahrenthold and Horban [6] and generalizes in a thermomechanical sense the Euler parameter based mechanical models of Chang and Chou [18] and others [19,20].

The organization of this paper may be summarized as follows. The second and third

sections define the particle and element kinematics and the interpolations used for all field variables. The fourth and fifth sections develop kinetic energy and thermomechanical potential energy functions for the system. The sixth section describes the dissipative process models, for plastic formation and damage evolution. The seventh and eighth sections present artificial viscosity and artificial heat diffusion models, similar to those used in other shock physics codes, and develop entropy evolution equations which take the place of the energy conservation relations normally employed. The ninth section introduces a virtual work expression, to account for externally applied loads. The tenth section combines the canonical thermomechanical Lagrange equations with the multiple nonholonomic constraints developed in the preceding sections, and derives an unconstrained explicit state space model for the particle-element system. The final section presents two example problems, showing good agreement of simulations performed using the model developed here to published data for three dimensional impact experiments. Additional validation work, for simulations performed using a spherical kernel, are described by Fahrenthold and Shivarama [21], who also provide details on the numerical implementation and test results showing numerical convergence and good parallel speedup.

PARTICLE KINEMATICS

The inertia distribution in the modeled system is represented by a collection of n ellipsoidal particles, with $m^{(i)}$ the mass of the ith particle, whose position and orientation are described by a center of mass position vector ($\mathbf{c}^{(i)}$) and an Euler parameter vector ($\mathbf{e}^{(i)}$) with component forms

$$\mathbf{c}^{(i)} = [\, c_1^{(i)} \; c_2^{(i)} \; c_3^{(i)} \,]^T, \qquad \mathbf{e}^{(i)} = [\, e_0^{(i)} \; e_1^{(i)} \; e_2^{(i)} \; e_3^{(i)} \,]^T \tag{1}$$

where T denotes the transpose. The components of the center of mass position vector are described in a fixed Cartesian coordinate system. The Euler parameters [17] define an orthogonal rotation matrix ($\mathbf{R}^{(i)}$) for each particle

$$\mathbf{R}^{(i)} = \mathbf{H}^{(i)} \, \mathbf{G}^{(i)T} \tag{2}$$

$$\mathbf{H}^{(i)} = \begin{bmatrix} -e_1^{(i)} & e_0^{(i)} & -e_3^{(i)} & e_2^{(i)} \\ -e_2^{(i)} & e_3^{(i)} & e_0^{(i)} & -e_1^{(i)} \\ -e_3^{(i)} & -e_2^{(i)} & e_1^{(i)} & e_0^{(i)} \end{bmatrix} \tag{3}$$

$$\mathbf{G}^{(i)} = \begin{bmatrix} -e_1^{(i)} & e_0^{(i)} & e_3^{(i)} & -e_2^{(i)} \\ -e_2^{(i)} & -e_3^{(i)} & e_0^{(i)} & e_1^{(i)} \\ -e_3^{(i)} & e_2^{(i)} & -e_1^{(i)} & e_0^{(i)} \end{bmatrix} \tag{4}$$

which relates the components of any vector ($\hat{\mathbf{a}}$), described in a body fixed co-rotating coordinate system, to its corresponding components in the fixed Cartesian system, using

$$\mathbf{a} = \mathbf{R}^{(i)}\,\hat{\mathbf{a}} \tag{5}$$

The four Euler parameters may be used to compute three Euler angles for each particle, and are preferred for use in large rotation dynamics problems, since the Euler angles are singular functions. Although the Euler parameters are nonsingular, they must satisfy the constraint

$$\mathbf{e}^{(i)T}\mathbf{e}^{(i)} = 1 \tag{6}$$

which requires that

$$\mathbf{G}^{(i)}\,\mathbf{e}^{(i)} = \mathbf{0}, \qquad \mathbf{G}^{(i)}\,\dot{\mathbf{e}}^{(i)} = -\,\dot{\mathbf{G}}^{(i)}\,\mathbf{e}^{(i)}, \qquad \mathbf{G}^{(i)}\,\mathbf{G}^{(i)T} = \mathbf{I} \tag{7}$$

where $\mathbf{I}$ denotes an identity matrix.

The Euler parameters and their time derivatives are related to the particle angular velocity vectors ($\boldsymbol{\omega}^{(i)}$), with components expressed in the particle's co-rotating frame, by the well known [17] relations

$$\boldsymbol{\omega}^{(i)} = 2\,\mathbf{G}^{(i)}\,\dot{\mathbf{e}}^{(i)}, \qquad \dot{\mathbf{e}}^{(i)} = \frac{1}{2}\,\mathbf{G}^{(i)T}\,\boldsymbol{\omega}^{(i)} \tag{8}$$

Similarly the anti-symmetric matrix $\boldsymbol{\Omega}$, with axial vector $\boldsymbol{\omega}$, which satisfies

$$\boldsymbol{\Omega}^{(i)}\mathbf{v} = \boldsymbol{\omega}^{(i)} \times \mathbf{v} \tag{9}$$

for any vector $\mathbf{v}$, is related to the Euler parameters and their time derivatives by

$$\boldsymbol{\Omega}^{(i)} = 2\,\mathbf{G}^{(i)}\,\dot{\mathbf{G}}^{(i)T} = -2\,\dot{\mathbf{G}}^{(i)}\mathbf{G}^{(i)T} \tag{10}$$

The next section presents a density interpolation associated with the particles just described, and defines Lagrangian finite elements whose nodal coordinates are components of the particle center of mass position vectors.

DENSITY INTERPOLATION AND FINITE ELEMENTS

In the material reference configuration, the ellipsoidal particles are arranged in a packing scheme defined by a mapping from a body centered cubic unit cell, the mapping composed of stretchings in three orthogonal directions, those directions aligned with the principal axes of the ellipsoids. The density interpolation for compressed states is

$$\rho^{(i)} \;=\; \rho_o^{(i)} + \sum_{j\,=\,1}^{n} \rho_o^{(j)}\, W^{(i,j)} \tag{11}$$

where $\rho^{(i)}$ is the continuum density at the centroid of the ith particle, $\rho_o^{(i)}$ is the reference density for the ith particle, and $W^{(i,j)}$ is the interpolation kernel

$$W^{(i,j)} \;=\; \frac{1}{8}\,(1-\delta_{ij}) \quad \left[\left(\frac{1}{\zeta^{(i,j)}}\right)^3 - 1\right] \quad \hat{u}\left(\xi^{(i,j)}\right) \tag{12}$$

$$\xi^{(i,j)} \;=\; \left(\frac{\alpha+\beta}{2}\right)\left(\frac{\rho_o^{(i)}}{\rho^{(i)}}\right)^{\frac{1}{3}} - \zeta^{(i,j)} \tag{13}$$

The symbols δ_{ij} and $\hat{u}$ denote respectively the Dirac delta function and the unit step function

$$\hat{u}(x) = \begin{cases} 0, & x \le 0 \\ 1, & x > 0 \end{cases} \tag{14}$$

The constants α and β are effective separation distances, in a unit cell, measured respectively between body centered particles and between a body centered particle and a particle located at a cell vertex

$$\alpha = \left(\frac{\pi}{3}\right)^{\frac{1}{3}}, \qquad \beta = \frac{\sqrt{3}}{2}\left(\frac{\pi}{3}\right)^{\frac{1}{3}} \tag{15}$$

Note that the lead coefficient in the expression for $W^{(i,j)}$ is due to the presence of eight nearest neighbors in the reference configuration.

The function $\zeta^{(i,j)}$ is an ellipsoidal coordinate, defined in a frame which co-rotates with the jth particle

$$\zeta^{(i,j)} = \left[\left(\mathbf{c}^{(i)} - \mathbf{c}^{(j)}\right)^T \mathbf{R}^{(j)} \mathbf{A}^{(j)} \mathbf{R}^{(j)^T} \left(\mathbf{c}^{(i)} - \mathbf{c}^{(j)}\right) \right]^{\frac{1}{2}} \tag{16}$$

$$\mathbf{A}^{(j)} = \begin{bmatrix} 2\beta h_1^{(j)} & 0 & 0 \\ 0 & 2\beta h_2^{(j)} & 0 \\ 0 & 0 & 2\beta h_3^{(j)} \end{bmatrix}^{-2} \tag{17}$$

where $h_1^{(j)}, h_2^{(j)}, h_3^{(j)}$ are the half-lengths of the principal axes of the jth particle.

Several properties of the density interpolation and kernel functions just described should be noted. The interpolation provides an exact Lagrangian description of the variation of density under uniform compression, and incorporates a lower bound equal to the particle reference density, so that tensile instabilities are avoided. The kernel is singular, so that no two particle centers overlap, avoiding particle streaming effects. In the reference configuration neighbor particles do not contribute to the density calculation, so that no special treatment of surface particles with incomplete neighbor sets is required. The density dependence of the compact kernel support means that particles interact only with near neighbors, and that mechanical interaction with remote neighbors through intervening matter is avoided. Finally note that the dimensionless kernel used here is closer in functional form and physical interpretation to the repulsion potentials used in molecular dynamics, than to the dimensional kernels with cubic spline form used in most SPH formulations.

The center of mass coordinates of vertex centered particles are nodal coordinates for hexahedral finite elements, which are used to account for tension and elastic-plastic shear in cohesive solid materials. These elements are used with one point integration, as described by Hallquist [22], although in the present case the element packing scheme and density interpolation preclude the development of hourglass modes. Since large deformation problems are of interest in hypervelocity impact applications, the element nodal coordinates are used here to compute a Jacobian ($J^{(j)}$) and a Lagrangian deviatoric strain tensor ($\overline{\mathbf{E}}^{(j)}$) for each

element, defined by [23]

$$J^{(j)} = det\, \mathbf{F}^{(j)}, \qquad \overline{\mathbf{E}}^{(j)} = \frac{1}{2}\left(\overline{\mathbf{C}}^{(j)} - \mathbf{I} \right) \tag{18}$$

where $\mathbf{F}^{(j)}$ is the deformation gradient for the jth element and

$$\overline{\mathbf{C}}^{(j)} = \overline{\mathbf{F}}^{(j)T} \overline{\mathbf{F}}^{(j)}, \qquad \overline{\mathbf{F}}^{(j)} = \left(det\, \mathbf{F}^{(j)} \right)^{-\frac{1}{3}} \mathbf{F}^{(j)} \tag{19}$$

The plasticity model discussed in a later section assumes an additive decomposition of the deviatoric strain, with the elastic deviatoric strain tensor ($\mathbf{E}^{e(j)}$) for the jth element defined by

$$\mathbf{E}^{e(j)} = \overline{\mathbf{E}}^{(j)} - \mathbf{E}^{p(j)} \tag{20}$$

so that the evolution equations for the plastic strain tensor ($\mathbf{E}^{p(j)}$) must satisfy the isochoric plastic deformation constraint

$$tr\left(\mathbf{C}^{p(j)-T} \dot{\mathbf{C}}^{p(j)} \right) = 0, \qquad \mathbf{E}^{p(j)} = \frac{1}{2}\left(\mathbf{C}^{p(j)} - \mathbf{I} \right) \tag{21}$$

It should be emphasized that the numerical modeling methodology developed in this paper applies for a wide range of element types and plasticity models. The particular element kinematics and constitutive equations used in this paper are representative formulations which account for large deformation kinematics.

KINETIC ENERGY

The kinetic co-energy for the system is

$$T^* \;=\; \sum_{i\,=\,1}^{n} T^{*(i)} \tag{22}$$

where $T^{*(i)}$ is the kinetic co-energy for the ith particle

$$T^{*(i)} = \frac{1}{2}\, m^{(i)}\, \dot{\mathbf{c}}^{(i)\,T} \dot{\mathbf{c}}^{(i)} \;+\; \frac{1}{2}\, \boldsymbol{\omega}^{(i)\,T}\, \mathbf{J}^{(i)}\, \boldsymbol{\omega}^{(i)} \tag{23}$$

and the components of the inertia matrix $\mathbf{J}^{(j)}$ are calculated in a body fixed frame. Since the components of the angular velocity vector are quasi-velocities, equations (8) are used to

rewrite the second term

$$T^{*(i)} = \frac{1}{2}\, m^{(i)}\, \dot{\mathbf{c}}^{(i)\,T} \dot{\mathbf{c}}^{(i)} \;+\; 2\, \dot{\mathbf{e}}^{(i)\,T} \mathbf{G}^{(i)\,T} \mathbf{J}^{(i)}\, \mathbf{G}^{(i)}\, \dot{\mathbf{e}}^{(i)} \tag{24}$$

which identifies the center of mass coordinates and the Euler parameters as generalized coordinates in Lagrange's equations. Note that the relations (7) allow the rotational kinetic co-energy to be expressed as

$$T^{*(i)}_{rot} = \; 2\, \mathbf{e}^{(i)\,T} \dot{\mathbf{G}}^{(i)\,T} \mathbf{J}^{(i)} \dot{\mathbf{G}}^{(i)}\, \mathbf{e}^{(i)} \tag{25}$$

so that the generalized force associated with the Euler parameter dependence of the kinetic co-energy is

$$\mathbf{k}^{(i)} = \frac{\partial T^{*(i)}}{\partial \mathbf{e}^{(i)}} = 4\, \dot{\mathbf{G}}^{(i)\,T} \mathbf{J}^{(i)} \dot{\mathbf{G}}^{(i)}\, \mathbf{e}^{(i)} \tag{26}$$

The next section develops a potential energy expression for the particle-element system.

POTENTIAL ENERGY

The potential energy of the particle-element system is the sum of the particle internal energies and the element stored energies due to tension and elastic shear, and has the general form

$$V \;\; = \;\; \sum_{i\,=\,1}^{n} m^{(i)}\, u^{(i)} + \sum_{j\,=\,1}^{n_e} \left(U^{ten(j)} + U^{dev(j)} + U^{pen(j)} \right) \tag{27}$$

where $u^{(i)}$ is an internal energy per unit mass, n_e is the number of elements, $U^{ten(j)}$ is a stored energy in tension, $U^{dev(j)}$ is a stored energy in shear, and $U^{pen(j)}$ is a penalty energy used to position the body centered particle in each element. The particle internal energy density is determined by the mass density and entropy density ($s^{(i)}$)

$$u^{(i)} = u^{(i)} \left(\rho^{(i)}, s^{(i)} \right), \qquad\qquad s^{(i)} = \frac{S^{(i)}}{m^{(i)}} \tag{28}$$

where $S^{(i)}$ is the total entropy of the ith particle. The functional form of the internal energy per unit mass depends on the equation of state, and it is not unusual in such calculations to

rely upon tabular data [24]. In any case, the extensive state variables which determine the particle internal energy are

$$u^{(i)} = u^{(i)}\left(\mathbf{c}^{(j)}, \mathbf{e}^{(j)}, S^{(i)}\right) \tag{29}$$

The form of the element stored energy functions depends upon the constitutive assumptions. Although the general method developed here admits a wide range of constitutive models, simple forms are assumed here, and are described as follows. The stored energy in tension is

$$U^{ten(j)} = \frac{1}{2}\left(1 - D^{(j)}\right)\kappa^{(j)}\, V_o^{(j)}\, (J^{(j)} - 1)^2\, \hat{u}(J^{(j)} - 1) \tag{30}$$

where $\kappa^{(j)}$ is a bulk modulus, $D^{(j)}$ is the normal damage, and $V_o^{(j)}$ is the element reference volume. The stored energy in shear is

$$U^{dev(j)} = \left(1 - d^{(j)}\right)\mu^{(j)}\, V_o^{(j)}\, tr\left(\mathbf{E}^{e(j)^T}\mathbf{E}^{e(j)}\right) \tag{31}$$

where $\mu^{(j)}$ is a shear modulus and $d^{(j)}$ is the deviatoric damage. The penalty function is

$$U^{pen(j)} = \frac{1}{2}\left(1 - D^{(j)}\right) K^{(j)}\, (\hat{\mathbf{c}}^{(j)} - \overline{\mathbf{c}}^{(j)})^2 \tag{32}$$

where $\hat{\mathbf{c}}^{(j)}$ is the center of mass position vector for the body centered particle of the jth element, $\overline{\mathbf{c}}^{(j)}$ is the average of the center of mass position vectors for the vertex centered particles (the element nodes), and the penalty stiffness is

$$K^{(j)} = E^{(j)} V_o^{(j)^{\frac{1}{3}}} \tag{33}$$

where $E^{(j)}$ is Young's modulus for the element. The damage variables are used to model the loss of cohesion due to element failure, and are discussed in the next section.

The preceding constitutive assumptions combine with the element kinematic relations

$$J^{(j)} = J^{(j)}\left(\mathbf{c}^{(i)}\right), \qquad \mathbf{E}^{e(j)} = \mathbf{E}^{e(j)}\left(\mathbf{c}^{(i)}, \mathbf{E}^{p(j)}\right) \tag{34}$$

to yield the following state variable dependence for the system potential energy

$$V = V\left(\mathbf{c}^{(i)}, \mathbf{e}^{(i)}, S^{(i)}, \mathbf{E}^{p(j)}, D^{(j)}, d^{(j)}\right) \tag{35}$$

The listed arguments, which include the particle entropies, are by definition Lagrangian generalized coordinates.

The system potential energy function defines the conservative generalized forces

$$\frac{\partial V}{\partial \mathbf{c}^{(i)}} = \mathbf{g}^{(i)}, \qquad \frac{\partial V}{\partial \mathbf{e}^{(i)}} = \mathbf{M}^{(i)}, \qquad \frac{\partial V}{\partial S^{(i)}} = \theta^{(i)} \tag{36}$$

where $\theta^{(i)}$ is a particle temperature, and $\mathbf{g}^{(i)}$ and $\mathbf{M}^{(i)}$ are forces and torques which act on the ellipsoidal particles. The energy conjugates for the dissipative state variables define a deviatoric stress

$$\mathbf{S}^{(j)} = -\frac{1}{V_o^{(j)}} \frac{\partial V}{\partial \mathbf{E}^{p(j)}} \tag{37}$$

as well as the energy release rates

$$\Gamma^{D(j)} = -\frac{\partial V}{\partial D^{(j)}}, \qquad \Gamma^{d(j)} = -\frac{\partial V}{\partial d^{(j)}} \tag{38}$$

The next section discusses evolution equations for the dissipative state variables.

PLASTICITY AND DAMAGE MODELS

The evolution equations for the plastic strain tensor and continuum damage variables will serve as nonholonomic constraints on the system level Lagrange equations. As discussed in the last section, the general formulation developed here admits a wide range of constitutive models. The relatively simple dissipative constitutive models assumed here are described in this section. The plasticity model is adapted from Fahrenthold and Horban [25], and represents the simplest possible accommodation of the isochoric deformation constraint (21). The damage evolution relations are adapted from the Eulerian hydrocode work of Silling [26].

The flow rule for the plastic strain is

$$\dot{\mathbf{E}}^{p(j)} = \frac{\dot{\lambda}^{(j)}}{\Pi^{(j)}} \left(\mathbf{C}^{p(j)} \, \mathbf{W}^{(j)} + \mathbf{W}^{(j)} \, \mathbf{C}^{p(j)} \right) \tag{39}$$

$$\mathbf{W}^{(j)} = \mathbf{C}^{p(j)} \, \mathbf{S}^{p(j)} + \mathbf{S}^{p(j)} \, \mathbf{C}^{p(j)} - \frac{1}{3} tr \left(\mathbf{C}^{p(j)} \, \mathbf{S}^{p(j)} + \mathbf{S}^{p(j)} \, \mathbf{C}^{p(j)} \right) \mathbf{I} \tag{40}$$

where $\dot{\lambda}^{(j)}$ is a scalar multiplier and

$$\Pi^{(j)} = (1 + \eta^{(j)} \epsilon^{p(j)})^{N^{(j)}} \left[\frac{1}{2} \, tr \left(\mathbf{W}^{(j)T} \mathbf{W}^{(j)} \right) \right]^{1/2} \tag{41}$$

$$\dot{\epsilon}^{p(j)} = \left[\frac{1}{2}\, tr\left(\dot{\mathbf{E}}^{p(j)T}\dot{\mathbf{E}}^{p(j)}\right)\right]^{1/2} \tag{42}$$

with $\eta^{(j)}$ a strain hardening modulus, $N^{(j)}$ a strain hardening exponent, and $\epsilon^{p(j)}$ the accumulated plastic strain. The effective stress tensor which appears in the flow rule is

$$\mathbf{S}^{p(j)} = (1+\eta^{(j)}\epsilon^{p(j)})^{-N^{(j)}}\,\mathbf{S}^{(j)}, \qquad \mathbf{S}^{(j)} = -\frac{1}{V_o^{(j)}}\,\frac{\partial V}{\partial \mathbf{E}^{p(j)}} = (1-d^{(j)})\,2\,\mu^{(j)}\,\mathbf{E}^{e(j)} \tag{43}$$

where the indicated deviatoric stress is power density conjugate to the plastic strain rate, in the entropy equality for the solid medium.

The yield condition is

$$f^{(j)} = \tau^{(j)} - Y^{(j)}, \qquad \tau^{(j)} = \left[\frac{1}{2} tr\left(\mathbf{S}^{p(j)T}\mathbf{S}^{p(j)}\right)\right]^{1/2} \tag{44}$$

where $\tau^{(j)}$ is the second invariant of the effective stress. The yield stress Y is

$$Y^{(j)} = Y_0^{(j)}\,(1-d^{(j)})\,\left(1-\gamma^{(j)}\theta^{H(j)}\right) \tag{45}$$

where $Y_0^{(j)}$ is the reference yield stress, $\gamma^{(j)}$ is a thermal softening modulus, and $\theta^{H(j)}$ is the maximum historical homologous temperature. The plastic strain increment at each time step is determined using a one step iteration procedure [22] with

$$\Delta\lambda^{(j)} = \frac{(\tau^{(j)} - Y^{(j)})\,\hat{u}(\tau^{(j)} - Y^{(j)})}{(1-d^{(j)})\,2\,\mu^{(j)}} \tag{46}$$

The final evolution equations for the plastic strain have the functional form

$$\dot{\mathbf{E}}^{p(j)} = \dot{\mathbf{E}}^{p(j)}\left(\mathbf{c}^{(i)}, S^{(i)}, \mathbf{E}^{p(j)}, d^{(j)}\right) \tag{47}$$

and are nonholonomic constraints on the particle-element model.

Hypervelocity impact problems normally involve perforation and fragmentation effects, so that the ability to model such physics is essential. In the present case normal and deviatoric damage variables are introduced, to model the transition from a cohesive solid, characterized by intact finite elements, to a comminuted medium, described by the free flow of particles.

Free particles interact with cohesive material and with other fragments under general contact-impact loads.

The damage evolutions applied here are

$$\dot{D}^{(j)} = \frac{\Lambda^{(j)}}{\hat{n}\,\Delta t}\,\hat{u}(1 - D^{(j)}), \qquad \dot{d}^{(j)} = \frac{\Lambda^{(j)}}{\hat{n}\,\Delta t}\,\hat{u}(1 - d^{(j)}) \tag{48}$$

where Δt is the time step, $\hat{n}$ is the number of time steps used to model the transition from an intact to a failed element, and

$$\Lambda^{(j)} = \; max\{\, \hat{u}(\epsilon^{p(j)} - \epsilon_f^{p(j)}),\; \hat{u}(\theta_{max}^{(j)} - \theta_m^{(j)}),\; \hat{u}(J_c^{(j)} - J_{min}^{(j)}),\; \hat{u}(\sigma_{max}^{(j)} - \sigma_s^{(j)})\,\} \tag{49}$$

The function just defined initiates damage evolution in an element when when the accumulated plastic strain $\epsilon^{p(j)}$, maximum temperature θ_{max}, minimum element Jacobian $J_{min}^{(j)}$, or maximum eigenvalue of the deviatoric stress $\sigma_{max}^{(j)}$ reach corresponding critical values for the failure strain $(\epsilon_f^{p(j)})$, melt temprature $(\theta_m^{(j)})$, maximum compression $(J_c^{(j)})$, or spall stress $(\sigma_s^{(j)})$. More sophisticated damage evolution relations may be introduced without change to the general modeling framework. The damage evolution equations are nonholonomic constraints which apply to the system level Lagrange equations.

ARTIFICIAL VISCOSITY AND HEAT DIFFUSION

The shock physics problems of interest here call for the introduction of artificial viscosity and artificial heat diffusion effects. The standard formulation used here takes the viscosity force $\mathbf{f}^{v(i)}$ on the ith particle to be

$$\mathbf{f}^{v(i)} = \sum_{j\,=\,1}^{n} \nu^{(i,j)}\; max\left(0, v^{(i,j)}\right)\; \mathbf{r}^{(i,j)}, \qquad \mathbf{r}^{(i,j)} = \frac{\left(\,\mathbf{c}^{(i)} - \mathbf{c}^{(j)}\,\right)}{|\,\mathbf{c}^{(i)} - \mathbf{c}^{(j)}\,|} \tag{50}$$

where the velocity difference $v^{(i,j)}$ is positive for converging particles

$$v^{(i,j)} = -\left(\,\dot{\mathbf{c}}^{(i)} - \dot{\mathbf{c}}^{(j)}\,\right) \cdot \mathbf{r}^{(i,j)} \tag{51}$$

The damping coefficient $\nu^{(i,j)}$ is

$$\nu^{(i,j)} = \frac{1}{2}\,\left(\rho^{(i)}\; c_s^{(i)} V_o^{(i)\,\frac{2}{3}} + \rho^{(j)}\; c_s^{(j)} V_o^{(j)\,\frac{2}{3}}\right)\left[\, c_o + \frac{2\,c_1 |v^{(i,j)}|}{(c_s^{(i)} + c_s^{(j)})}\,\right]\,\hat{u}(1 - \zeta^{(i,j)}) \tag{52}$$

where $c_s^{(i)}$ is the sound speed for the ith particle and the parameters c_o and c_1 are dimensionless linear and quadratic numerical viscosity coefficients.

The numerical heat diffusion model assumed here takes the thermal power flow for the ith particle to be

$$\dot{Q}^{con(i)} = \sum_{j=1}^{n} R^{(i,j)} \left(\theta^{(i)} - \theta^{(j)} \right) \tag{53}$$

$$R^{(i,j)} = \frac{1}{2} \left(\rho^{(i)} \, c_s^{(i)} c_v^{(i)} V_o^{(i)\,\frac{2}{3}} + \rho^{(j)} \, c_s^{(j)} c_v^{(j)} V_o^{(j)\,\frac{2}{3}} \right) k_o \, \hat{u} (1 - \zeta^{(i,j)}) \tag{54}$$

where $c_v^{(i)}$ is the specific heat for the ith particle and the parameter k_o is a dimensionless numerical heat diffusion coefficient.

ENTROPY EVOLUTION EQUATIONS

The introduction of entropy state variables, which facilitates the use of an energy based modeling approach, means that the conservation of energy relations normally incorporated in shock physics models are replaced here by evolution equations for the particle entropies. These evolution equations are

$$\dot{S}^{(i)} = \dot{S}^{irr(i)} - \dot{S}^{con(i)} \tag{55}$$

where the irreversible entropy production ($\dot{S}^{irr(i)}$) is due to plastic deformation, damage evolution, and viscous disspation

$$\dot{S}^{irr(i)} = \theta^{(i)-1} \left[\mathbf{f}^{v(i)^T} \dot{\mathbf{c}}^{(i)} + \sum_{j=1}^{n_e} \phi^{(i,j)} \left\{ \Gamma^{D(j)} \dot{D}^{(j)} + \Gamma^{d(j)} \dot{d}^{(j)} + V_o^{(j)} \, tr \left(\mathbf{S}^{(j)T} \dot{\mathbf{E}}^{p(j)} \right) \right\} \right] \tag{56}$$

and $\phi^{(i,j)}$ is the fraction of the dissipation in element j associated with the ith particle. The conduction entropy flow ($\dot{S}^{con(i)}$) is due to artificial heat diffusion

$$\dot{S}^{con(i)} = \theta^{(i)-1} \, \dot{Q}^{con(i)} = \sum_{j=1}^{n} R^{(i,j)} \left(1 - \frac{\theta^{(j)}}{\theta^{(i)}} \right) \tag{57}$$

Since the dissipated energy is not lost but rather transduced to the thermal domian, the entropy evolution equations are nonholonomic constraints in the thermomechanical Lagrangian formulation.

VIRTUAL WORK

Although external loads are normally not considered in hypervelocity impact applications, for completeness this section develops a virtual work expression. The virtual work for the system is a summation over the particles

$$\delta W \;=\; \sum_{i=1}^{n} \delta W^{(i)} \tag{58}$$

In this case the particle angular velocities are the time derivatives of rotational quasi-coordinates ($\mathbf{q}^{(i)}$)

$$\dot{\mathbf{q}}^{(i)} = \boldsymbol{\omega}^{(i)} \tag{59}$$

so that the virtual work for the ith particle is

$$\delta W^{(i)} = \mathbf{f}^{(i)T} \delta \mathbf{c}^{(i)} + \mathbf{T}^{(i)T} \delta \mathbf{q}^{(i)} \tag{60}$$

where $\mathbf{f}^{(i)}$ and $\mathbf{T}^{(i)}$ are externally applied forces and torques. In view of equation (8), virtual changes in the quasi-coordinates and the Euler parameters are related by

$$\delta \mathbf{q}^{(i)} = 2\, \mathbf{G}^{(i)}\, \delta \mathbf{e}^{(i)} \tag{61}$$

so that the particle virtual work expression is

$$\delta W^{(i)} = \mathbf{f}^{(i)T} \delta \mathbf{c}^{(i)} + 2 \left[\, \mathbf{G}^{(i)T} \mathbf{T}^{(i)} \,\right]^{T} \delta \mathbf{e}^{(i)} \tag{62}$$

The coefficients of the virtual changes in the generalized coordinates are by definition generalized nonconservative forces in the system level Lagrange equations.

LAGRANGE'S EQUATIONS

The stored energy functions, constraint equations, and virtual work expression developed in the preceding sections may be combined with the canonical Lagrange equations, to obtain an ODE model for the particle-element system.

The canonical Lagrange equations are

$$\frac{d}{dt}\left(\frac{\partial T^*}{\partial \dot{\mathbf{c}}^{(i)}}\right) - \frac{\partial T^*}{\partial \mathbf{c}^{(i)}} + \frac{\partial V}{\partial \mathbf{c}^{(i)}} \;=\; \mathbf{Q}^{c(i)} \tag{63}$$

$$\frac{d}{dt}\left(\frac{\partial T^*}{\partial \dot{\mathbf{e}}^{(i)}}\right) - \frac{\partial T^*}{\partial \mathbf{e}^{(i)}} + \frac{\partial V}{\partial \mathbf{e}^{(i)}} \;=\; \mathbf{Q}^{e(i)} \tag{64}$$

$$\frac{\partial V}{\partial S^{(i)}} = Q^{s(i)}, \qquad \frac{\partial V}{\partial \mathbf{E}^{p(j)}} = \mathbf{Q}^{p(j)} \tag{65}$$

$$\frac{\partial V}{\partial d^{(j)}} = Q^{d(j)}, \qquad \frac{\partial V}{\partial D^{(j)}} = Q^{D(j)} \tag{66}$$

where $\mathbf{Q}^{c(i)}$, $\mathbf{Q}^{e(i)}$, $Q^{s(i)}$, $Q^{d(i)}$, $Q^{D(i)}$, and $\mathbf{Q}^{p(j)}$ are generalized forces determined by the constraints and the virtual work. Note that the rate form of the Euler parameter constraint for the ith particle is

$$\dot{\mathbf{e}}^{(i)T}\mathbf{e}^{(i)} \;=\; 0 \tag{67}$$

Introducing a Lagrange multiplier $\gamma^{e(i)}$ for each Euler parameter constraint as well as Lagrange multipliers $\gamma^{s(i)}$, $\gamma^{d(i)}$, $\gamma^{D(i)}$, and $\mathbf{X}^{p(i)}$ for the entropy, normal damage, deviatoric damage, and plastic strain evolutions equations, the generalized nonconservative forces are found to be

$$\mathbf{Q}^{c(i)} \;=\; \mathbf{f}^{(i)} - \frac{\gamma^{s(i)}}{\theta^{(i)}}\,\mathbf{f}^{v(i)} \tag{68}$$

$$\mathbf{Q}^{e(i)} \;=\; 2\,\mathbf{G}^{(i)T}\mathbf{T}^{(i)} + \gamma^{e(i)}\mathbf{e}^{(i)} \tag{69}$$

$$Q^{s(i)} \;=\; \gamma^{(i)} \tag{70}$$

$$Q^{d(j)} \;=\; \gamma^{d(j)} - \sum_{i=1}^{n} \frac{\gamma^{s(i)}}{\theta^{(i)}}\,\phi^{(i,j)}\,\Gamma^{d(j)} \tag{71}$$

$$Q^{D(j)} \;=\; \gamma^{D(j)} - \sum_{i=1}^{n} \frac{\gamma^{s(i)}}{\theta^{(i)}}\,\phi^{(i,j)}\,\Gamma^{D(j)} \tag{72}$$

$$\mathbf{Q}^{p(j)} \;=\; \mathbf{X}^{p(j)} - \sum_{i=1}^{n} \frac{\gamma^{s(i)}}{\theta^{(i)}}\,\phi^{(i,j)}\,V_o^{(j)}\,\mathbf{S}^{(j)} \tag{73}$$

If these results and the degenerate Lagrange equations (65) and (66) are combined with the previously derived expression for the kinetic co-energy, the momentum balance relations take the form

$$\frac{d}{dt}\left(m^{(i)}\,\dot{\mathbf{c}}^{(i)}\right) + \frac{\partial V}{\partial \mathbf{c}^{(i)}} \;=\; \mathbf{f}^{(i)} - \mathbf{f}^{v(i)} \tag{74}$$

$$\frac{d}{dt}\left(4\,\mathbf{G}^{(i)\,T}\mathbf{J}^{(i)}\,\mathbf{G}^{(i)}\,\dot{\mathbf{e}}^{(i)}\right) - \mathbf{k}^{(i)} + \frac{\partial V}{\partial \mathbf{e}^{(i)}} \;=\; 2\,\mathbf{G}^{(i)T}\mathbf{T}^{(i)} + \gamma^{e(i)}\mathbf{e}^{(i)} \tag{75}$$

Introducing the momentum variables

$$\mathbf{p}^{(i)} = m^{(i)}\,\dot{\mathbf{c}}^{(i)}\,, \qquad\qquad \mathbf{h}^{(i)} = \mathbf{J}^{(i)}\,\boldsymbol{\omega}^{(i)} \tag{76}$$

and premultiplying the angular momentum balance expression (75) by $\frac{1}{2}\,\mathbf{G}^{(i)}$, which [using equation (7)] removes the last term, yields the final state space formulation

$$\dot{\mathbf{p}}^{(i)} \;=\; -\mathbf{g}^{(i)} - \mathbf{f}^{v(i)} + \mathbf{f}^{(i)} \tag{77}$$

$$\dot{\mathbf{h}}^{(i)} \;=\; -\boldsymbol{\Omega}^{(i)}\mathbf{h}^{(i)} - \frac{1}{2}\mathbf{G}^{(i)}\mathbf{M}^{(i)} + \mathbf{T}^{(i)} \tag{78}$$

$$\dot{\mathbf{c}}^{(i)} \;=\; m^{(i)-1}\,\mathbf{p}^{(i)} \tag{79}$$

$$\dot{\mathbf{e}}^{(i)} \;=\; \frac{1}{2}\mathbf{G}^{(i)T}\mathbf{J}^{(i)-1}\mathbf{h}^{(i)} \tag{80}$$

Augmented by the evolution equations for $S^{(i)}$, $D^{(j)}$, $d^{(j)}$, and $\mathbf{E}^{p(j)}$, these are explicit first order equations for the particle-element system. With appropriate initial conditions they may be integrated to obtain solutions for a wide range of hypervelocity impact problems.

EXAMPLE SIMULATIONS

This section compares the results of simulations performed using a numerical implementation [27] of the model developed here, to published experimental results for two hypervelocity impact problems. The simulations employed a Mie-Grunsisen equation of state and

$$c_o = 0.001, \qquad c_1 = 0.0, \qquad k_o = 0.1, \qquad \epsilon_f^p = 1.0 \tag{81}$$

with material properties taken from Steinberg [28].

The first example involves the impact of a uranium alloy rod on a steel plate, 0.64 cm in thickness, in an experiment described by Hertel [29]. The cylindrical projectile is 0.767 cm in diameter, with a length to diameter ratio of ten, and impacts the plate at an obliquity of 73.5 degrees and a velocity of 1.21 kilometers per second. The velocity of the target plate is 0.217 kilometers per second. The simulation employed 712,929 particles, with the projectile composed of spherical particles and the target plate composed of ellipsoidal particles with aspect ratios of 1.5:1.5:1.0. Figure 1 shows an element plot of the initial configuration, while Figure 2 shows a particle plot of the simulation results at 100 microseconds after impact. The simulation results for the rod erosion (27.5 percent) and residual rod velocity (1.10 km/s) show good agreement with the corresponding experimental values (27.6 percent and 1.07 km/s).

The second example involves the impact of a tungsten rod on a steel plate, 0.95 cm in thickness, in an experiment described by Yatteau et al. [30]. The cylindrical projectile is 0.475 cm in diameter, with a length to diameter ratio of twenty, and impacts the plate at an obliquity of 75 degrees and a velocity of 1.83 kilometers per second. The target plate is stationary. The simulation employed 671,176 particles, with the projectile composed of spherical particles and the target plate composed of ellipsoidal particles with aspect ratios of 1.5:1.5:1.0. Figure 3 shows an element plot of the initial configuration, while Figure 4 shows a particle plot of the simulation results at 150 microseconds after impact. The simulation results for the rod erosion (37.9 percent) and residual rod velocity (1.60 km/s) show good agreement with the corresponding experimental values (40 percent and 1.78 km/s).

In the preceding problems the vast majority of the particles are associated with the target plates, so that the use of ellipsoidal particles reduces the total particle count by a factor of approximately 2.25, equal to the product of the three indicated aspect ratios. It should be noted that the computational advantages of a reduced particle count can in part be offset by an increase in the average number of nominal neighbors per particle. This increase is

due to the fact that the neighbor search for each particle must consider a spatial volume proportional to the cube of the major ellipsoidal axis, despite the fact that a closer approach without contact can occur when particle minor axes are appropriately aligned. Experience to date indicates that the use of ellipsoidal particles leads to a reduction in memory requirements which is proportional to the reduction in particle count, but to a cpu time requirement similar to that measured in corresponding simulations with spherical particles.

CONCLUSION

The present paper has developed an ellipsoidal particle-finite element method for hypervelocity impact problems, and demonstrated its use in the simulation of three dimensional impact experiments. The hybrid particle-element kinematic scheme allows for the use of true Lagrangian strength models, while incorporating a completely general description of contact-impact effects. Tensile instability, numerical fracture, and angular momentum balance problems, often associated with particle formulations, are avoided. Material remaps, mass or energy discard, slideline algorithms, and adaptive mesh refinement, often associated with continuum models, are also avoided. Derivation of the model is based on a thermomechanical form of Lagrange's equations, with entropy variables as generalized coordinates. The use of an energy based modeling approach facilitates the systematic integration of diverse particle based and element based interpolations. Work to date suggests that the method provides a numerically robust and accurate approach to the simulation of hypervelocity impact problems.

ACKNOWLEDGEMENTS

This work was supported by NASA Johnson Space Center (NAG9-1244), the National Science Foundation (CMS99-12475), and the State of Texas Advanced Research Program (003658-0709-1999). Computer time support was provided by the NASA Advanced Supercomputing Division (ARC) and the Texas Advanced Computing Center (UTA).

REFERENCES

[1] Anderson CE. An overview of the theory of hydrocodes. *International Journal of Impact Engineering*, 1987; **5**: 33-60.

[2] McGlaun JM, Thompson SL, Elrick MG. CTH: A three dimensional shock wave physics code. *International Journal of Impact Engineering*, 1990; **10**: 351-360.

[3] Wallin BK, Tong C, Nichols AL, Chow ET. Large multiphysics simulations in ALE3D. Presented at the Tenth SIAM Conference on Parallel Processing for Scientific Computing, Portsmouth, Virginia, March 12-14, 2001.

[4] Faraud M, Destefanis R, Palmieri D, Marchetti M. SPH Simulations of debris impacts using two different computer codes. *International Journal of Impact Engineering*, 1999; **23**: 249-260.

[5] Hayhurst CJ, Livingstone IHG, Clegg, RA, Destefanis R, Faraud M. Ballistic limit evaluation of advanced shielding using numerical simulations. *International Journal of Impact Engineering*, 2001; **26**: 309-320.

[6] Fahrenthold EP, Horban BA. An improved hybrid particle-element method for hypervelocity impact simulation. *International Journal of Impact Engineering*, 2001; **26**: 169-178.

[7] Fahrenthold EP. Numerical simulation of impact on hypervelocity shielding. Proceedings of the Hypervelocity Shielding Workshop, 1998, Galveston, Texas, pp. 47-50.

[8] Rapaport DC. Molecular dynamics simulation using quaternions. *Journal of Computational Physics*, 1985; **41**: 306-314.

[9] Shapiro PR, Martel H, Villumsen JV, Owen JM. Adaptive smoothed particle hydrodynamics with application to cosmology: methodology. *The Astrophysical Journal Supplement Series*, 1996; **103**: 269-330.

[10] Owen JM, Villumsen JV, Shapiro PR, Martel H. Adaptive smoothed particle hydrodynamics with application to cosmology: methodology II. *The Astrophysical Journal Supplement Series*, 1998; **116**: 155-209.

[11] Benson DJ. Computational methods in Lagrangian and Eulerian hydrocodes. *Computer Methods in Applied Mechanics and Engineering*, 1992; **99**: 235-394.

[12] Carroll DE, Hertel ES, Trucano TG. Simulation of armor penetration by tungsten rods: ALEGRA validation report, 1997, SAND97-2765, Sandia National Laboratories.

[13] Stellingwerf RF, Wingate CA. Impact modeling with smooth particle hydrodynamics. *International Journal of Impact Engineering*, 1993; **14**: 707-718.

[14] Johnson GR, Petersen EH, Stryk RA. Incorporation of an SPH option into the EPIC code for a wide range of high velocity impact computations. *International Journal of Impact Engineering*, 1993; **14**: 385-394.

[15] Belytschko T, Krongauz Y, Organ D, Fleming M, Krysl P. Meshless methods: an overview and recent developments. *Computer Methods in Applied Mechanics and Engineering*, 1996; **139**: 3-47.

[16] Hayhurst CJ, Livingstone IH, Clegg RA, Fairlie GE, Hiermaier SH, Lambert M. Numerical simulation of hypervelocity impacts on aluminum and Nextel/Kevlar Whipple shields. Proceedings of the Hypervelocity Shielding Workshop, 1998, Galveston, Texas, pp. 61-72.

[17] Haim Baruh. Analytical Dynamics, 1999, McGraw Hill, New York.

[18] C.O. Chang and C.S. Chou. Design of a viscous ring nutation damper for a freely precessing body. *Journal of Guidance, Control and Dynamics*, 1991; **14**: 1136-1144.

[19] P.E. Nikravesh, R.A. Wehage, and O.K. Kwon. Euler parameters in computational kinematics and dynamics. part 1. *Journal of Mechanisms, Transmissions and Automation Design*, 1985; **107**: 358-365.

[20] P.E. Nikravesh, O.K. Kwon, and R.A. Wehage. Euler parameters in computational kinematics and dynamics. part 2. *Journal of Mechanisms, Transmissions and Automation Design*, 1985; **107**: 366-369.

[21] Fahrenthold EP, Shivarama R. Extension and validation of a hybrid particle-element method for hypervelocity impact simulation. *International Journal of Impact Engineering*, accepted for publication.

[22] Hallquist JO. Theoretical Manual for DYNA3D, 1983, Lawrence Livermore National Laboratory, Livermore, California.

[23] Lubliner J. Plasticity theory, 1990, Macmillan, New York

[24] Lyon SP, Johnson JD, editors. SESAME: The Los Alamos National Laboratory Equation of State Database, LA-UR-92-3407, Los Alamos National Laboratory, Los Alamos, New Mexico.

[25] Fahrenthold EP, Horban BA. Thermodynamics of continuum damage and fragmentation models for hypervelocity impact. *International Journal of Impact Engineering*, 1997; **20**: 241-252.

[29] Silling SA. CTH Reference Manual: Johnson-Holmquist Ceramic Model, 1992, SAND92-0576, Sandia National Laboratories.

[27] Fahrenthold EP. User's Guide for EXOS, 2001, University of Texas, Austin.

[28] Steinberg DJ. Equation of State and Strength Properties of Selected Materials, 1996, Lawrence Livermore National Laboratory, UCRL-MA-106439.

[29] Hertel ES. A Comparison of the CTH Hydrodynamics Code With Experimental Data, 1992, SAND92-1879, Sandia National Laboratories.

[30] Yatteau JD, Recht GW, Edquits KT. Transverse loading and response of long rod penetrators during high velocity plate perforation. *International Journal of Impact Engineering*, 1999; **23**: 967-980.

LIST OF FIGURES

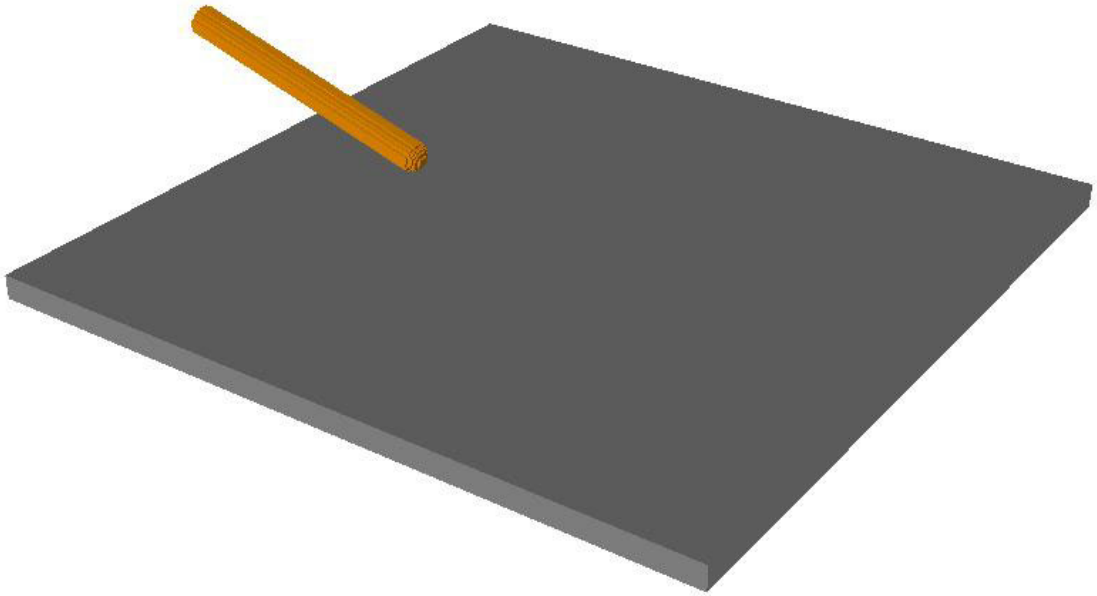

Figure 1: Uranium alloy long rod impact on a steel plate, element plot of the initial configuration

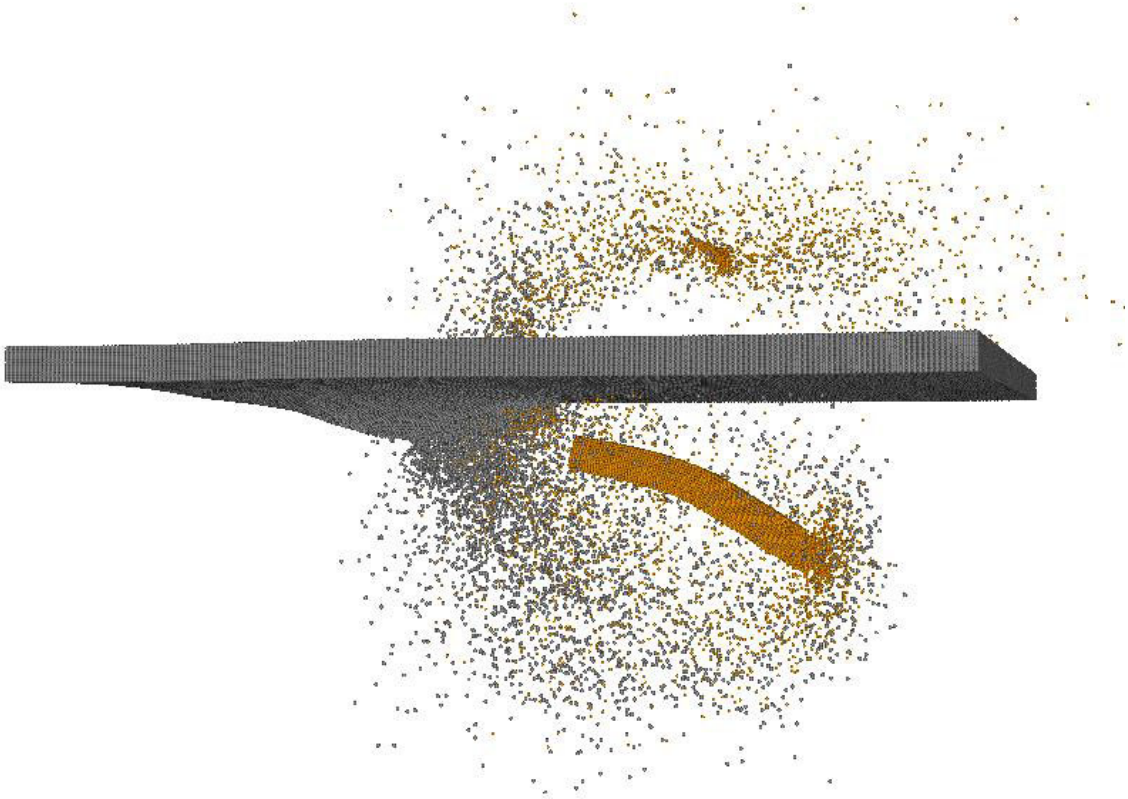

Figure 2: Uranium alloy long rod impact on a steel plate, particle plot at 100 microseconds after impact

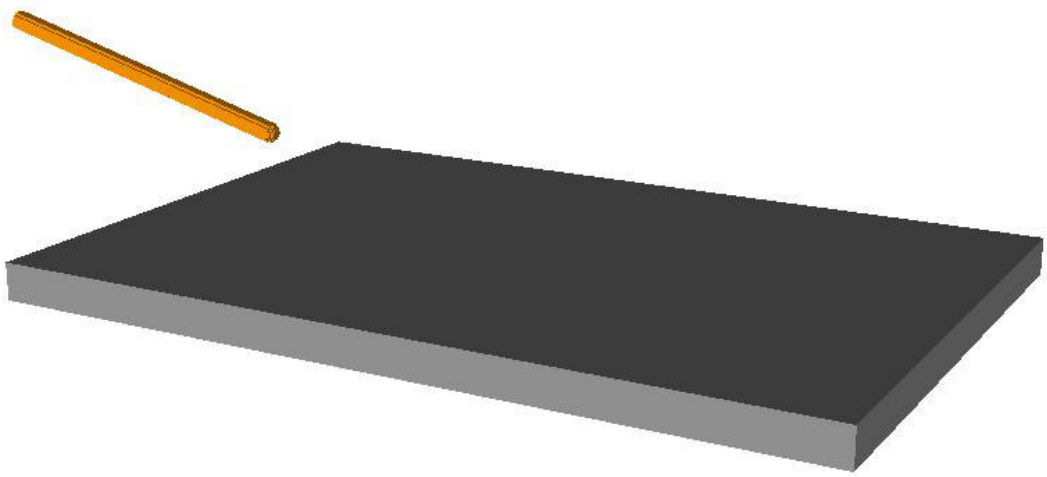

Figure 3: Tungsten long rod impact on a steel plate, element plot of the initial configuration

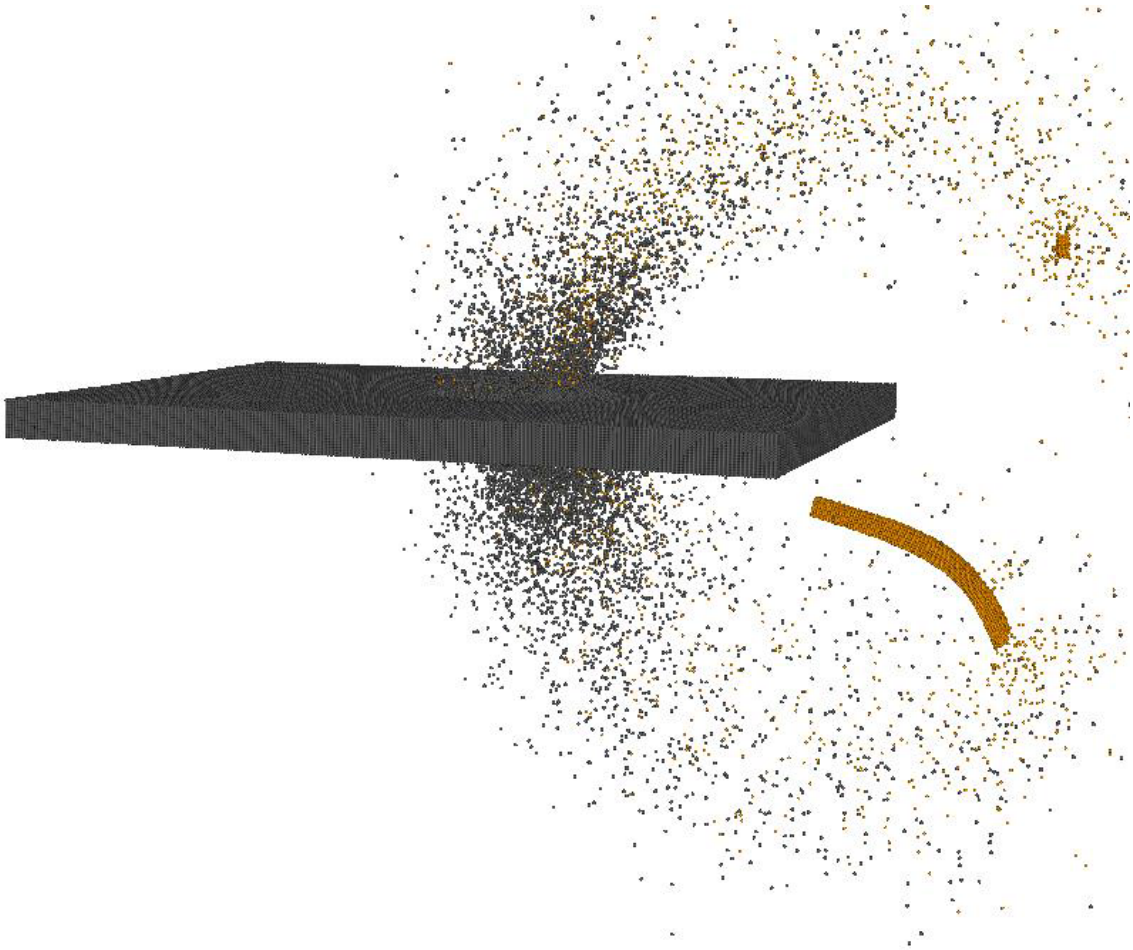

Figure 4: Tungsten long rod impact on a steel plate, particle plot at 150 microseconds after impact

CHAPTER 2

EXTENSION AND VALIDATION OF A HYBRID PARTICLE-FINITE ELEMENT METHOD FOR HYPERVELOCITY IMPACT SIMULATION

Eric P. Fahrenthold[1] **and Ravishankar Shivarama**[2]

Department of Mechanical Engineering, 1 University Station C2200
University of Texas, Austin, TX 78712, USA

[1]Professor, corresponding author, phone: (512) 471-3064, email: epfahren@mail.utexas.edu
[2]Graduate student

Extension and Validation of a Hybrid Particle-Finite Element Method for Hypervelocity Impact Simulation

Eric P. Fahrenthold and Ravishankar Shivarama

Department of Mechanical Engineering, 1 University Station C2200, University of Texas, Austin, TX 78712, USA

Abstract

The hybrid particle-finite element method of Fahrenthold and Horban [1], developed for the simulation of hypervelocity impact problems, has been extended to include new formulations of the particle-element kinematics, additional constitutive models, and an improved numerical implementation. The extended formulation has been validated in three dimensional simulations of published impact experiments. The test cases demonstrate good agreement with experiment, good parallel speedup, and numerical convergence of the simulation results.

Keywords: impact simulation, numerical methods

1. Introduction

In previous work Fahrenthold and Horban [1] developed a hybrid particle-finite element method for hypervelocity impact simulation, and applied that formulation in the analysis of several three dimensional problems. The referenced modeling methodolody employs Lagrangian finite elements to represent material strength effects, namely tension and elastic-plastic shear, and Lagrangian particles to represent inertia, compressed states, and contact-impact effects. Particles and elements are used in tandem throughout the simulation, for all materials, so that no element-to-particle transformations are required. The introduction of both particles and elements is not redundant, since they are employed to account for distinct physical effects. A systematic approach to the formulation of this hybrid numerical scheme is provided by Hamiltonian mechanics. General thermomechanical dynamics are represented,

via the introduction of entropy variables as generalized Hamiltonian coordinates.

Development of the particle-element method just outlined has been motivated by difficulties encountered in the application of pure Eulerian, Lagrangian, or particle based methods to the problem of orbital debris shielding design [2]. The latter application calls for simulation of shock loading and perforation at very high velocities, accurate characterization of strength-dependent structural response, efficient modeling of fragment transport, and general descriptions of contact-impact. Recent research suggests that hybrid [3] or coupled [4] numerical methods are best suited to simulate orbital debris impact on space structures. Numerical methods developed for the latter application may also have application in related problems, such as research on the effects of behind armor debris.

2. Extended Formulation

The hybrid particle-finite element model of Fahrenthold and Horban [1] has been extended to include alternative formulations of the particle-element kinematics, additional constitutive models, and an improved numerical implementation. The extended formulation described in this section has been evaluated for accuracy, numerical convergence, and parallel speedup in a series of three dimensional simulations of published experiments, as described in the sections which follow.

The density interpolation of reference [1] used distinct kernels for reference configuration nearest neighbors and for all other particles. A simplified alternative is the implicit interpolation

$$\rho^{(i)} = {\rho_o}^{(i)} + \frac{1}{8} \sum_{j=1}^{n-1} {\rho_o}^{(j)} \left(\left[\frac{2\alpha h^{(j)}}{r_{ij}} \right]^3 - 1 \right) \Lambda \left(\frac{2\beta h^{(j)}}{r_{ij}} \left[\frac{{\rho_o}^{(i)}}{\rho^{(i)}} \right]^{\frac{1}{3}} - 1 \right) \qquad (1)$$

where $\rho^{(i)}$ is the interpolated density, ${\rho_o}^{(i)}$ is a reference density, $h^{(j)}$ is a particle radius, r_{ij} is a particle center of mass separation distance, the constants α and β are determined by the body centered cubic particle packing scheme, n is the number of particles, Λ denotes the unit step function, and the summation applies for $j \neq i$. Note that the preceding interpolation yields exact results for hydrostatic compression of a particle set arranged in the selected packing scheme, and that in general all neighbor particles interact in the same fashion.

The particle packing scheme used in the present work leads to eight nearest neighbors for body centered particles in the reference configuration. Fahrenthold and Horban [1] used the body centered particle associated with each hexahedral element to define subelement domains. The volumes of these subdomains may be used to determine the interparticle tensile forces associated with material dilatation. This six point integration scheme is computationally expensive, and leads to hexahedral elements which are stiffer than those employed for example in some very successful Lagrangian codes [5]. In the present work the potential energy contribution due to tension is written

$$U^{ten} = \sum_{j=1}^{n_e} \frac{1}{2} (1 - D^{(j)}) \{ V^{(j)} \kappa^{(j)} (J^{(j)} - 1)^2 \Lambda(J^{(j)} - 1) + 2h^{(j)} E^{(j)} \mid \mathbf{c}^{(j)} - \mathbf{c}^{avg(j)} \mid^2 \} \qquad (2)$$

where n_e is the number of elements, $V^{(j)}$ is the element reference volume, $\kappa^{(j)}$ is the element bulk modulus, $E^{(j)}$ is the element Young's modulus, $J^{(j)}$ is the element Jacobian, $D^{(j)}$ is the element normal damage, $\mathbf{c}^{(j)}$ is the position vector of the body centered particle, and $\mathbf{c}^{avg(j)}$ is the average position vector of the particles which define the element nodes. This potential function represents a one point integration of the element, to quantify tension effects, along with a penalty term which positions the body centered particle. Note that interparticle tension is (neglecting surface tension) a strength effect, and is therefore associated with relative motion of a reference configuration neighbor set (in this case the finite elements) and not a time varying neighbor set of the type used to quantify collision forces [6].

Shock physics codes can include options for the treatment of energy conservation errors which may occur during integration or transformation of the system level model. Examples are a default energy discard used in the remap step of CTH [7] and energy errors which may arise from contact-impact calculations in ALE [8] or SPH [9,10] formulations. Although precise energy conservation can be demonstrated in simple benchmark problems, it can be computationally expensive to achieve the same result in the simulation of more complex practical problems. For the hybrid particle-element formulation described here, an optional energy correction term has been added to the particle entropy evolution equations

$$\Delta S^{err} = \epsilon \, \Delta H^{err} \left(\sum_{j=1}^{n} \theta^{(j)} \right)^{-1} \tag{3}$$

where ΔH^{err} is the error in the system Hamiltonian, $\theta^{(j)}$ is a particle temperature, and with $\epsilon = 0.1$ the error correction is introduced over ten time steps. The effect of this term is to satisfy global energy conservation by introducing an internal energy correction for each particle which is proportional to the current particle temperature.

Simulation results obtained using particle based models are in general influenced by the choice of particle packing scheme. The locations and properties of nearest neighbor particles define in general a local stiffness distribution for the medium which is anisotropic, as in the case of pure crystals [11]. In addition the choice of a particle packing scheme determines an effective void ratio for the medium. Hence it is not surprising that particle packing can influence simulation results. The preprocessor used in the present work employs a random number generator to delete a user specified fraction of body centered particles from the original perfect lattice structure. The introduction of these flaws mimics the influence of grain orientations, dislocations, and other defects on the mechanical response of real materials.

The simulations described in references [1] and [3] employed analytic equations of state. Extension of the code described in the latter work has included the introduction of interpolation routines, to accommodate tabulated equations of state in two independent variables. Currently the SESAME tables [12] are used for simulations at very high velocities, and are accessed in their default form, with pressure and internal energy defined on a density and temperature grid. Iteration is therefore used to converge on an internal energy calculated from the Gibbs relation

$$\dot{U}^{int(i)} = \theta^{(i)} \, \dot{S}^{(i)} + \frac{m^{(i)} P^{(i)}}{{\rho^{(i)}}^2} \left(\sum_{j=1}^{n} \frac{\partial \rho^{(i)}}{\partial \mathbf{c}^{(j)}} \, \dot{\mathbf{c}}^{(j)} \right) \tag{4}$$

where $m^{(i)}$ is a particle mass and $P^{(i)}$ is a particle pressure. An initial call to the SESAME routines is used to establish the reference internal energy associated with the simulation initial conditions.

In addition to the preceding work, significant extensions and applications of the hybrid particle-element method discussed here are reported elsewhere. First, Shivarama [13] has extended the basic formulation to include ellipsoidal particles, introducing a nonspherical kernel, rotational motion of the particles, and Euler parameters as state variables. This extension makes possible for example the modeling of thin plate structures at greatly reduced particle counts. It should be noted that previous work on nonspherical particle models for shock physics problems has been very limited [14,15]. Second, application of the method to composite orbital debris shielding problems is reported by Fahrenthold and Park [16], including development and numerical implementation of a rate-dependent material model for Kevlar.

3. Validation Simulations

A series of three dimensional simulations was performed to evaluate the extended formulation just described. The simulations modeled published experiments conducted at impact velocities ranging from one to eleven kilometers per second. Each example problem was modeled at two different mesh densities, to investigate numerical convergence of the simulation results. The selected problems have been previously studied by various investigators, to evaluate other numerical methods and computer codes. Tables 1 and 2 provide details on the problem parameters and material properties for all the validation simulations. Material properties were estimated using data from Steinberg [23]. The first two example problems used a Mie-Gruneisen equation of state, while the third example problem used the SESAME tables.

Table 1. Parameters of the example problems

Parameter	*Sphere*	*Long rod*	*Debris shield*
Projectile material	Aluminum	DU 0.75% Ti	Aluminum
Target/shield/wall material	Aluminum	Steel	Aluminum
First shield thickness (cm)	na	na	0.25
Second shield thickness (cm)	na	na	0.25
Target/wall plate thickness (cm)	0.1143	0.64	0.50
Shield spacing (cm)	na	na	6.0
Projectile velocity (km/sec)	6.56	1.21	11.0
Impact obliquity (deg)	45	73.5	45
Projectile diameter (cm)	0.953	0.767	0.5062
Projectile length-to-diameter ratio	na	10	4.36

na = not applicable

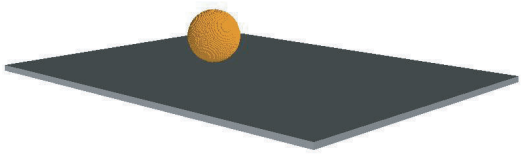

Fig. 1. Element plot of the initial configuration for the sphere impact problem.

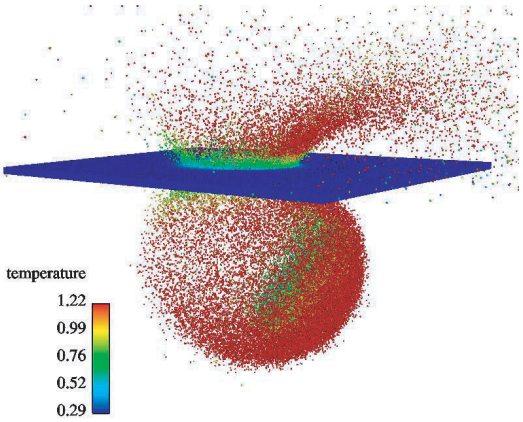

Fig. 2. Particle plot of the simulation results for the sphere impact problem.

Table 2. Material properties used in the example problems

Material property	*Aluminum*	*DU 0.75% Ti*	*Steel*
Shear modulus (Mbar)	0.271	0.74	0.801
Reference density (g/cc)	2.7	18.62	7.842
Initial yield stress (Mbar)	0.0029	0.0095	0.012
Maximum yield stress (Mbar)	0.0058	0.0220	0.025
Strain hardening exponent	0.1	0.095	0.5
Strain hardening modulus	125.0	1000.0	2.0
Melt temperature (degrees Kelvin)	1,220	1,710	2,310
Specific heat (Mbar-cm^3 per g-kilodeg Kelvin)	0.00884	0.00111	0.00448
Spall stress (Mbar)	0.012	0.028	0.032
Plastic failure strain	1.0	1.0	1.0

The first example problem involves the oblique (45 degree) impact of an 0.953 cm diameter aluminum sphere on a thin (0.1143 cm) plate, at 6.56 kilometers per second, and is representative of typical Whipple shield design problems. Figure 1 shows an element plot of the initial configuration of the projectile and target, while Figure 2 shows a particle plot of the simulation results at 6.6 microseconds after impact. The simulation results show good agreement with the experimental radiograph [17]. This problem was run on 16 processors of an IBM Regatta at two different mesh densities, with models composed of 0.67 million and 3.20 million particles. The dimensions of the plate perforation were compared to determine the effect of model resolution on the simulation results. Table 3 shows that an increase in the particle count by nearly a factor of five produced only a small variation in the predicted dimensions of the plate perforation.

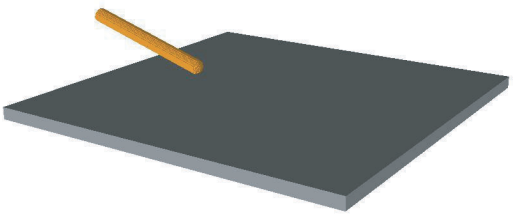

Fig. 3. Element plot of the initial configuration for the long rod impact problem.

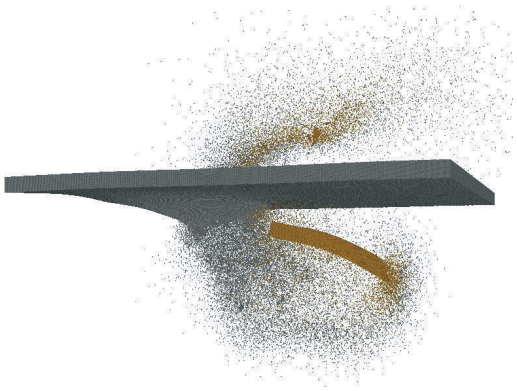

Fig. 4. Particle plot of the simulation results for the long rod impact problem.

Table 3. Simulation results for the sphere impact problem

Problem size (particles)	*Wall clock time (hours)*	*Perforation width (cm)*	*Perforation length (cm)*
0.673 million	4.04	1.90	2.43
3.196 million	39.6	1.81	2.39

The second example problem involves the oblique (73.5 degree) impact of an 0.767 cm diameter uranium alloy rod (L/D = 10) on a steel plate target (thickness 0.64 cm), at a rod velocity of 1.21 kilometers per second (target velocity was 0.217 km/s). This problem is representative of typical armor-antiarmor design applications. Figure 3 shows an element plot of the initial configuration of the projectile and target, while Figure 4 shows a particle plot of the simulation results at 100 microseconds after impact. The simulation results provided in Table 4 show good agreement with the corresponding experimental values [18] of residual rod length (5.55 cm) and residual rod velocity (1.07 km/sec). This problem was run on 16 processors of an IBM Regatta at two different mesh densities, with models composed of 1.56 million and 5.06 million particles. Table 4 shows that a factor of more than three increase in the particle count produced only a small variation in the simulation results.

Table 4. Simulation results for the long rod impact problem

Problem size (particles)	*Wall clock time (hours)*	*Residual length (cm)*	*Residual velocity (km/s)*
1.566 million	13.8	5.74	1.09
5.060 million	74.4	5.78	1.09

The third example problem involves the oblique (45 degree) impact of an aluminum shaped charge projectile (0.5062 cm diameter, 2.2046 cm length) on an aluminum plate target protected by a dual plate aluminum debris shield. The projectile velocity was 11.0 kilometers per second, while the wall plate thickness (0.50 cm), shield thickness (0.25 cm), and total

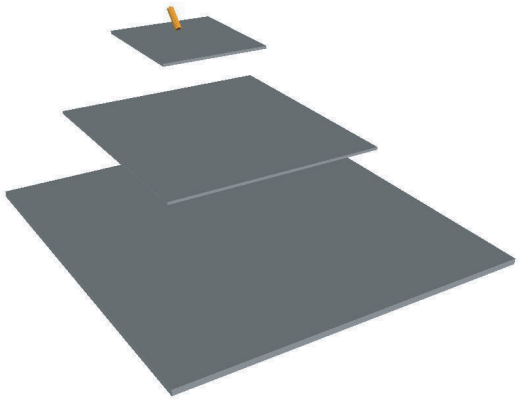

Fig. 5. Element plot of the initial configuration for the dual plate shield problem.

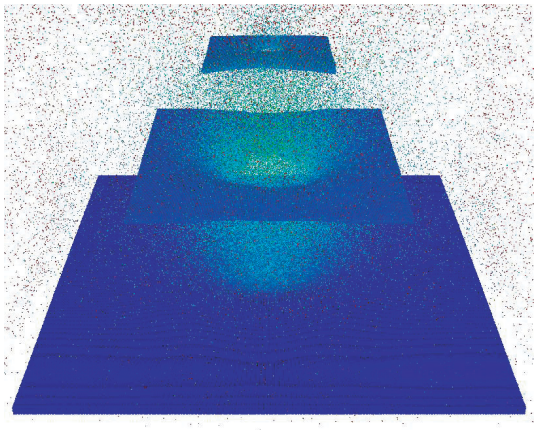

Fig. 6. Particle plot of the simulation results for the dual plate shield problem.

standoff distance (12.0 cm) are representative of orbital debris shielding design applications. This problem has been designated a benchmark for use in the numerical analysis of spacecraft protection systems [19]. Figure 5 shows an element plot of the initial configuration of the system, while Figure 6 shows a particle plot of the simulation results at 150 microseconds after impact. Consistent with the corresponding experiment, the simulation results show bulging but no perforation of the wall plate. This problem was run on SGI Origin systems at two different mesh densities, with models composed of 4.27 million and 12.90 million particles. The smaller model required 56.8 wall clock hours on 256 (400MHz) processors, while the larger model required 332 wall clock hours on an average of 502 (600Mhz) processors. The two simulations indicated very similar wall plate damage. Figures 7 through 9 show details of the shield perforations and wall plate damage, in element plots made at 150 microseconds after impact. This problem illustrates that the hybrid numerical method used here is well suited to represent both the very general contact-impact dynamics illustrated in Figure 6 and the large deformation plasticity illustrated in Figures 7 through 9.

4. Parallel Speedup Tests

The simulations described in the preceding section illustrate that three dimensional hypervelocity impact simulation can be very computer resource intensive. Hence the parallel performance characteristics of the relevant algorithm and numerical implementation is of considerable interest. This section discusses several algorithmic and implementation issues and presents measured parallel speedup data. Parallel implementation [20] of the hybrid method discussed here is based on the OpenMP standard [21], a set of portable compiler directives which may be simply applied to achieve loop level parallelism. Although an OpenMP implementation does not manage distributed memory, the effects of nonuniform memory access on code performance can in some cases be observed and influenced, through changes in the initial data placement scheme.

The hybrid nature of the present numerical formulation requires that both finite element

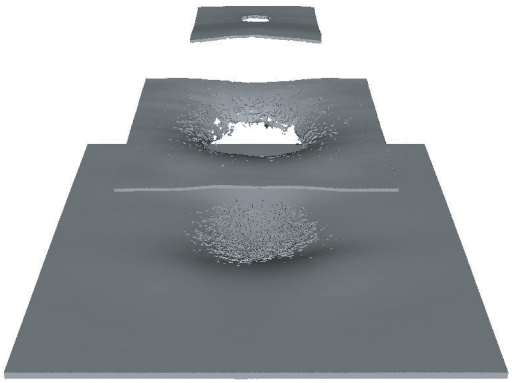

Fig. 7. Element plot of the simulation results for the dual plate shield problem.

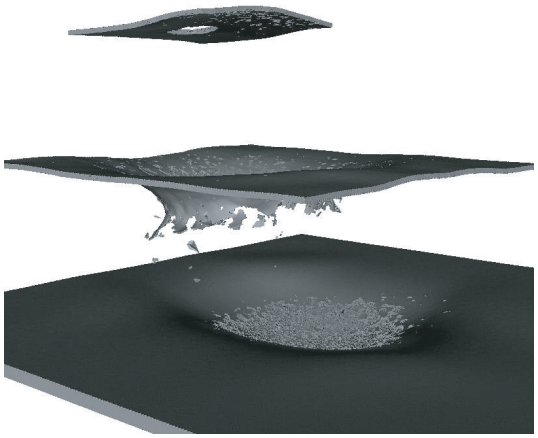

Fig. 8. Oblique view of the simulation results for the dual plate shield problem.

based and particle based computation take place throughout the simulation. The Lagrangian finite element calculations involve an invariant neighbor set for each particle, known at the start of the calculation. This allows for a very efficient parallel implementation, and suggests the use of a material based domain decomposition technique on distributed memory systems. Unfortunately a Lagrangian description of contact-impact and fragmentation effects, applied here and represented using the particle kinematics, involves a second (and time varying) neighbor set for each particle. Calculations involving this neighbor set are relatively inefficient, since a significant number of nominal neighbors identified by a search algorithm will turn out to be outside the effective mechanical or thermal interaction range. This portion of the calculation suggests the use of a geometry based domain decomposition technique, like that used in Eulerian codes, for distributed memory systems. However in this case, unlike Eulerian models, the membership of the contact-impact neighbor set for a given particle is time varying. This can present significant problems with load balancing and communications overhead.

The aforementioned considerations are reflected in the results of performance testing on the code used here, which indicates that: (a) particle based calculations largely determine the required wall clock time, (b) most wall clock time is spent in the routines which calculate the densities and particle interaction forces, via summations over the contact-impact neighbor set, and (c) round-robin (or maximum entropy) initial data placement provides the best overall performance on nonuniform memory access systems.

The authors provided in reference [3] speedup data for test cases run on as many as 128 processors of an SGI Origin, applying a hybrid particle-element modeling methodology to problems as large as 0.5 million particles. As noted in the last section, more recent work has focused on much larger models, hence speedup tests have recently been performed at larger processor counts. These tests employed a 1024 processor SGI Origin and problem sizes as large as fifteen million particles. The test problem used for speedup measurements was the oblique sphere impact problem discussed in the section on validation simulations. Tables 5 and 6 show the results of test cases run for two different model sizes (4.7 and 14.6 million

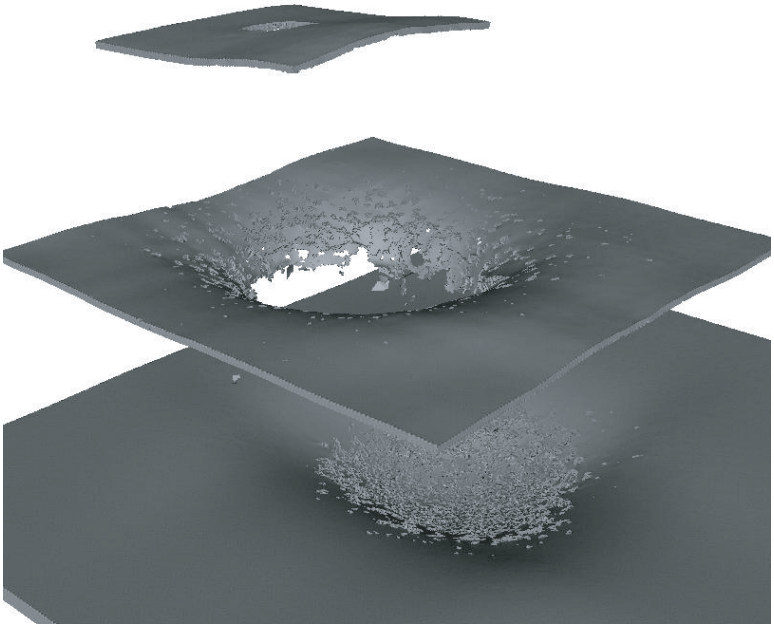

Fig. 9. Second oblique view of the simulation results for the dual plate shield problem.

particles), at various processor counts, ranging from 256 to approximately one thousand. In both cases speedup is measured relative to the wall clock time required for the test problem on 256 processors, and efficiency is defined as the ratio of measured to ideal relative speedup. The wall clock times shown are those required to complete 100 time steps of the simulation.

Table 5 shows good relative efficiency for the smaller test problem, when moving from 256 to 504 cpus, but very poor performance (in fact an increase in wall clock time) when the cpu count is then increased to 1008. Note that in the 1008 processor simulation each cpu is allocated approximately 5,000 particles, a load level apparently too light to allow for efficient parallel performance. Table 6 provides results for the larger test problem, where a minimum load level of nearly 15,000 particles per processor is maintained. In this case parallel performance is significantly improved, with a relative efficiency of almost seventy percent measured as the processor count is increased from 256 to 976. The preceding results indicate that the numerical method and OpenMP implementation tested here can efficiently address rather large scale problems. A dependence of parallel efficiency on processor load, observed here, is not unusual for engineering applications [22].

Table 5. Speedup measurements for a 4.7 million particle test problem

Number of processors	*Particles per processor*	*Wall clock time (hours)*	*Speedup (relative)*	*Efficiency (relative)*
256	18,281	0.7858	1.000	1.000
504	9,286	0.4858	1.618	0.822
1008	4,643	0.5008	1.569	0.400

Table 6. Speedup measurements for a 14.8 million particle test problem

Number of processors	*Particles per processor*	*Wall clock time (hours)*	*Speedup (relative)*	*Efficiency (relative)*
256	57,031	1.8439	1.000	1.000
512	28,516	1.0391	1.775	0.887
640	22,813	0.8803	2.095	0.838
976	14,959	0.7031	2.623	0.688

5. Conclusion

A number of new numerical methods based entirely or in part on particle kinematics are currently under development. They emphasize the fact that some important engineering problems are dominated by noncontinuum physics, such as fragmentation and contact-impact. Such problems may not fit easily into a classical continuum mechanics modeling framework. The present paper has described recent work aimed at extending and validating a hybrid numerical method for hypervelocity impact simulation. The results suggest that the method is accurate, numerically robust, and suitable for large scale parallel computation.

Acknowledgements

This work was supported by the Space Science Branch of NASA Johnson Space Center (NAG9-1244) and the National Science Foundation (CMS99-12475). Computer time support was provided by the Advanced Supercomputing Division of NASA Ames Research Center and the Texas Advanced Computing Center at the University of Texas at Austin.

References

[1] Fahrenthold EP, Horban BA. An improved hybrid particle-element method for hypervelocity impact simulation. *International Journal of Impact Engineering*, 2001; **26**: 169-178.

[2] Fahrenthold EP. Numerical simulation of impact on hypervelocity shielding. Proceedings of the Hypervelocity Shielding Workshop, 1998, Galveston, Texas, pp. 47-50.

[3] Fahrenthold EP, Shivarama R. Orbital debris impact simulation using a parallel hybrid particle-element code. *International Journal of Impact Engineering*, 2001; **26**: 179-188.

[4] Hayhurst CJ, Livingstone IH, Clegg RA, Fairlie GE, Hiermaier SH, Lambert M. Numerical simulation of hypervelocity impacts on aluminum and Nextel/Kevlar Whipple shields. Proceedings of the Hypervelocity Shielding Workshop, 1998, Galveston, Texas, pp. 61-72.

[5] Hallquist JO. Theoretical Manual for DYNA3D, 1983, Lawrence Livermore National Laboratory, Livermore, California.

[6] Fahrenthold EP, Koo JC. Hybrid particle-element bond graphs for impact dynamics simulation. *Journal of Dynamic Systems, Measurement, and Control*, 2000; **122**: 306-313.

[7] McGlaun JM, Thompson SL, Elrick MG. CTH: A three dimensional shock wave physics code. *International Journal of Impact Engineering*, 1990; **10**: 351-360.

[8] Wallin BK, Tong C, Nichols AL, Chow ET. Large multiphysics simulations in ALE3D. Presented at the Tenth SIAM Conference on Parallel Processing for Scientific Computing, Portsmouth, Virginia, March 12-14, 2001.

[9] Birnbaum NK, Francis NJ, Berber BI. Coupled techniques for the simulation of fluid-structure and impact problems. Structures Under Extreme Loading Conditions, ASME PVP-Vol. 361, 1998, San Diego, California, pp. 91-99.

[10] Faraud M, Destefanis R, Palmieri D, Marchetti M. SPH Simulations of debris impacts using two different computer codes. *International Journal of Impact Engineering*, 1999; **23**: 249-260.

[11] VanVlack LH. Elements of Materials Science and Engineering, 1975, Addison-Wesley, Inc., Reading, Massachusetts.

[12] Lyon SP, Johnson JD, editors. SESAME: The Los Alamos National Laboratory Equation of State Database, LA-UR-92-3407, Los Alamos National Laboratory, Los Alamos, New mexico.

[13] Shivarama RA. Hamilton's equations with Euler parameters for hybrid particle-element simulation of hypervelocity impact, PhD dissertation, Department of Mechanical Engineering, University of Texas at Austin, August, 2002.

[14] Shapiro PR, Martel H, Villumsen JV, Owen JM. Adaptive smoothed particle hydrodynamics with application to cosmology: methodology. *The Astrophysical Journal Supplement Series*, 1996; **103**: 269-330.

[15] Owen JM, Villumsen JV, Shapiro PR, Martel H. Adaptive smoothed particle hydrodynamics with application to cosmology: methodology II. *The Astrophysical Journal Supplement Series*, 1998; **116**: 155-209.

[16] Fahrenthold EP, Park Y-K. Simulation of hypervelocity impact on aluminum-Nextel-Kevlar orbital debris shields. *International Journal of Impact Engineering*, accepted for publication.

[17] Piekutowski AJ. Formation and Description of Debris Clouds Produced by Hypervelocity Impact, 1996, NASA Contractor Report 4707.

[18] Hertel ES. A Comparison of the CTH Hydrodynamics Code With Experimental Data, 1992, SAND92-1879, Sandia National Laboratories.

[19] Lambert M. Presentation at the 15th Inter-Agency Debris Committee Conference, European Space Agency (ESTEC), December 9-12, 1997.

[20] Fahrenthold EP. User's Guide for EXOS, 1999, University of Texas, Austin.

[21] Chandra R, Dagum L, Kohr D, Maydan D, McDonald J, Menon R. Parallel Programming in OpenMP, 2001, Academic Press, London.

[22] Gardner DR, Vaughan CT. The Optimization of a Shaped-Charge Design Using Parallel Computers, 1999, SAND99-2953, Sandia National Laboratories.

[23] Steinberg DJ. Equation of State and Strength Properties of Selected Materials, 1996, Lawrence Livermore National Laboratory, UCRL-MA-106439.

CHAPTER 3

HAMILTON'S EQUATIONS WITH EULER PARAMETERS FOR RIGID BODY DYNAMICS MODELING

Ravishankar Shivarama[1] **and Eric P. Fahrenthold**[2]

Department of Mechanical Engineering, 1 University Station C2200
University of Texas, Austin, TX 78712, USA

[1]Graduate student

[2]Professor, corresponding author, phone: (512) 471-3064, email: epfahren@mail.utexas.edu

HAMILTON'S EQUATIONS WITH EULER PARAMETERS FOR RIGID BODY DYNAMICS MODELING

Ravishankar Shivarama[3] **and Eric P. Fahrenthold**[4]

Department of Mechanical Engineering, University of Texas, Austin, TX 78712

A combination of Euler parameter kinematics and Hamiltonian mechanics provides a rigid body dynamics model well suited for use in strongly nonlinear problems involving arbitrarily large rotations. The model is unconstrained, free of singularities, includes a general potential energy function and a minimum set of momentum variables, and takes an explicit state space form convenient for numerical implementation. The general formulation may be specialized to address particular applications, as illustrated in several three dimensional example problems.

INTRODUCTION

A variety of rigid body dynamics modeling problems demand consideration of very large rotations. Some of the best known examples involve aircraft [1] and spacecraft [2,16], although the analysis of large rotation dynamics is of generic interest in a wide range of applications, including mechanism and machine theory [3,4] and molecular dynamics [12]. Most models of rigid body dynamics problems employ Euler angles [5]. Such formulations lead to equations of motion which are unconstrained, but which contain singularities [1]. Other singular three parameter methods have been developed, including for example those of Laning-Bortz-Stuelpnagel [11] and Rodriguez [13]. The presence of singularities in all these methods has motivated the development of alternative four parameter modeling schemes [11], including Euler parameters [15]. Such formulations replace the three Euler angles with four

[3]Graduate research assistant
[4]Professor

parameters and an algebraic constraint. This avoids the Euler angle singularities but leads nominally to a system level model in differential-algebraic form.

In an attempt to avoid both singular equations of motion and differential-algebraic systems, several authors have presented reformulations of Euler parameter based models, for use in three dimensional rigid body dynamics problems. Chang et al. [2], Nikravesh and co-workers [7,8,9,10], and Vadali [17] present alternative formulations based on Lagrange's equations. Since Lagrange's method defines the solution as a path in configuration space, and since the Euler parameters are taken as generalized coordinates, this approach starts with a differential system of order eight (four second order equations for the rotational dynamics of a single rigid body) augmented with a single algebraic constraint. Nikravesh and co-workers begin from this starting point and proceed to find a closed form solution for the Lagrange multiplier associated with the algebraic constraint, resulting in an unconstrained formulation of order eight. They do not include a potential energy function in the system Lagrangian. Similar results are obtained by Vadali. Proceeding in a different manner, Chang et al. introduce as quasi-velocity variables the rigid body angular velocities in the body fixed frame, and project the original order eight Lagrange equations onto an order seven subspace. In the process they eliminate the unknown Lagrange multiplier.

As an alternative to Lagrange's equations, a Hamiltonian formulation of rigid body dynamics with Euler parameters has been proposed by Morton [6]. However his final formulation is of order eight, and includes a superfluous momentum variable as well as a 'generally arbitrary' unspecified scalar parameter. It appears that no previous work has attempted to revise or improve upon the Morton formulation.

The usefulness of formulations based on Hamilton's canonical equations is well recognized [3]. They offer an explicit state space description of system dynamics problems which is: (a) convenient for numerical integration, (b) well suited for coupling to automatic control system models, and (c) energy based and hence providing clear physical insight. Recognizing these strengths, a revision and extension of existing Hamiltonian formulations for rigid body

dynamics is of generic interest. The present paper presents such work, deriving unconstrained Hamilton's equations for the three dimensional dynamics of a rigid body in terms of Euler parameters, and hence suitable for use in simulations involving arbitrary rotational motion. The derivation avoids any requirement to determine the Lagrange multiplier associated with the Euler parameter constraint. No arbitrary parameters are introduced, and the final rotational formulation is of order seven. A general potential energy function and nonpotential virtual work effects are included in the model. Validation and application of the method is illustrated here in several three dimensional example problems.

KINEMATICS

This section defines the kinematic variables of interest, and recalls a number of well known kinematic relations [1], for use in succeeding sections.

The position and orientation of an arbitrary rigid body is described here in terms of seven generalized coordinates, namely the Cartesian components of the center of mass vector ($\mathbf{c}$) and a four component vector of Euler parameters ($\mathbf{e}$)

$$\mathbf{c} = [\, c_1 \; c_2 \; c_3 \,]^T, \qquad \mathbf{e} = [\, e_0 \; e_1 \; e_2 \; e_3 \,]^T \tag{1}$$

Knowledge of the Euler parameters determines a (nonunique) set of Euler angles (ϕ, θ, ψ) for the body, associated with a 3-1-3 rotation sequence, via the relations

$$\phi = tan^{-1}\left(\frac{e_3}{e_0}\right) + tan^{-1}\left(\frac{e_2}{e_1}\right) \tag{2}$$

$$\psi = tan^{-1}\left(\frac{e_3}{e_0}\right) - tan^{-1}\left(\frac{e_2}{e_1}\right) \tag{3}$$

$$\theta = 2\, sin^{-1}\left(\sqrt{{e_1}^2 + {e_2}^2}\right) \tag{4}$$

The Euler parameters define an orthogonal rotation matrix ($\mathbf{R}$) which relates the vector of components ($\mathbf{a}$) of a first order tensor described in a fixed Cartesian coordinate system to a corresponding vector of components ($\hat{\mathbf{a}}$) described in a body fixed co-rotating frame, using

$$\mathbf{a} = \mathbf{R}\, \hat{\mathbf{a}} \tag{5}$$

where

$$\mathbf{R} = \mathbf{E}\,\mathbf{G}^T \tag{6}$$

with

$$\mathbf{E} = \begin{bmatrix} -e_1 & e_0 & -e_3 & e_2 \\ -e_2 & e_3 & e_0 & -e_1 \\ -e_3 & e_2 & e_1 & e_0 \end{bmatrix} \tag{7}$$

$$\mathbf{G} = \begin{bmatrix} -e_1 & e_0 & e_3 & -e_2 \\ -e_2 & -e_3 & e_0 & e_1 \\ -e_3 & -e_2 & -e_1 & e_0 \end{bmatrix} \tag{8}$$

The four Euler parameters are not independent, and satisfy the constraint equation

$$\mathbf{e}^T\mathbf{e} = 1 \tag{9}$$

which then implies

$$\mathbf{G}\,\mathbf{G}^T = \mathbf{I} \tag{10}$$

where $\mathbf{I}$ is an order three identity matrix. In addition, $\mathbf{G}$ and $\mathbf{e}$ and their time derivatives satisfy the identities

$$\mathbf{G}\,\mathbf{e} = \mathbf{0}, \qquad \mathbf{G}\,\dot{\mathbf{e}} = -\,\dot{\mathbf{G}}\,\mathbf{e} \tag{11}$$

The kinematic equations [1] which relate the time derivatives of the Euler parameters to the components of the angular velocity vector ($\boldsymbol{\omega}$) of the rigid body, expressed in the body-fixed co-rotating frame, are

$$\boldsymbol{\omega} = 2\,\mathbf{G}\,\dot{\mathbf{e}}, \qquad \dot{\mathbf{e}} = \frac{1}{2}\,\mathbf{G}^T\,\boldsymbol{\omega} \tag{12}$$

Finally note that the skew-symmetric matrix $\boldsymbol{\Omega}$, with axial vector $\boldsymbol{\omega}$, which satisfies

$$\boldsymbol{\Omega}\mathbf{v} = \boldsymbol{\omega} \times \mathbf{v} \tag{13}$$

for any vector $\mathbf{v}$, is related to the Euler parameters and their time derivatives by

$$\boldsymbol{\Omega} = 2\,\mathbf{G}\,\dot{\mathbf{G}}^T = -2\dot{\mathbf{G}}\mathbf{G}^T \tag{14}$$

The next section defines kinetic and potential energy functions and hence the Hamiltonian for the system of interest.

KINETIC AND POTENTIAL ENERGY

The complementary kinetic energy for the rigid body may be expressed as

$$T^* = \frac{1}{2}\, m\, \dot{\mathbf{c}}^{\,T} \dot{\mathbf{c}} \;+\; \frac{1}{2}\, \boldsymbol{\omega}^{\,T}\, \mathbf{J}\, \boldsymbol{\omega} \tag{15}$$

where m is the mass and $\mathbf{J}$ is a constant matrix of components for the moment of inertia tensor of the body, referred to the co-rotating frame. In terms of the Euler parameters and their time derivatives,

$$T^* = \frac{1}{2}\, m\, \dot{\mathbf{c}}^{\,T} \dot{\mathbf{c}} \;+\; 2\, \dot{\mathbf{e}}^{\,T} \mathbf{G}^{\,T} \mathbf{J}\, \mathbf{G}\, \dot{\mathbf{e}} \tag{16}$$

which has the form $T^* = T^*\,(\,\dot{\mathbf{c}}, \dot{\mathbf{e}}, \mathbf{e}\,)$. It follows that the generalized momenta are

$$\mathbf{p} = \frac{\partial T^*}{\partial \dot{\mathbf{c}}} = m\, \dot{\mathbf{c}}\,, \qquad\qquad \mathbf{g} = \frac{\partial T^*}{\partial \dot{\mathbf{e}}} = 4\, \mathbf{G}^{\,T} \mathbf{J}\, \mathbf{G}\, \dot{\mathbf{e}} \tag{17}$$

Note that the identities (10) through (12) require

$$\mathbf{g} = 2\, \mathbf{G}^T \mathbf{J}\, \boldsymbol{\omega}, \qquad\qquad \boldsymbol{\omega} = \frac{1}{2}\, \mathbf{J}^{-1} \mathbf{G}\, \mathbf{g} \tag{18}$$

Since the complimentary rotational kinetic energy may also be expressed, using equation (11), as

$$T^*_{rot} = \; 2\, \mathbf{e}^{\,T} \dot{\mathbf{G}}^{\,T} \mathbf{J} \dot{\mathbf{G}}\, \mathbf{e} \tag{19}$$

then the Euler parameter dependence of T^* defines the partial derivative

$$\mathbf{k} = \frac{\partial T^*}{\partial \mathbf{e}} = 4\, \dot{\mathbf{G}}^{\,T} \mathbf{J} \dot{\mathbf{G}}\, \mathbf{e} \tag{20}$$

The kinetic energy of the body is defined via the Legendre transform

$$T = \mathbf{p}^T \dot{\mathbf{c}} + \mathbf{g}^T \dot{\mathbf{e}} - T^* \tag{21}$$

so that the preceding results lead to the canonical form $T = T\,(\,\mathbf{p}, \mathbf{g}, \mathbf{e}\,)$ which is

$$T = \frac{1}{2}\, m^{-1}\, \mathbf{p}^{\,T} \mathbf{p} \;+ \frac{1}{8}\, \mathbf{g}^T \mathbf{G}^T \mathbf{J}^{-T} \mathbf{G}\, \mathbf{g} \tag{22}$$

and require that (see the appendix)

$$-\mathbf{k} = \frac{\partial T}{\partial \mathbf{e}} \tag{23}$$

For the mechanical systems considered here, the potential energy function has the general form

$$V = V(\mathbf{c}, \mathbf{e}) \tag{24}$$

and the system Hamiltonian is

$$H = T + V \tag{25}$$

The next section introduces a virtual work expression, to account for nonpotential effects.

NONPOTENTIAL VIRTUAL WORK

The quasi-coordinates $\mathbf{q}$ associated with the co-rotating components of the angular velocity vector are defined by

$$\dot{\mathbf{q}} = \boldsymbol{\omega} \tag{26}$$

In terms of the latter coordinates, and the center of mass coordinates, the nonpotential virtual work due to the imposed forces $\mathbf{f}(t)$ and torques $\mathbf{T}(t)$ is

$$\delta W_{nc} = \mathbf{f}(t)^T \delta \mathbf{c} + \mathbf{T}(t)^T \delta \mathbf{q} \tag{27}$$

Since

$$\delta \mathbf{q} = 2\, \mathbf{G}\, \delta \mathbf{e} \tag{28}$$

the virtual work expression which defines the generalized nonpotential forces is

$$\delta W_{nc} = \mathbf{f}(t)^T \delta \mathbf{c} + 2 \left[\mathbf{G}^T \mathbf{T}(t) \right]^T \delta \mathbf{e} \tag{29}$$

Note that damping effects may contribute additional terms to the nonpotential virtual work, in which case the nonpotential forces may depend on the generalized coordinates and velocities. In addition the presence of nonholonomic constraints may introduce terms which depend on unknown Langrange multipliers. The last problem discussed in the examples section illustrates the effects of both damping and nonholonomic constraints.

The next section derives Hamilton's equations for the system.

HAMILTON'S EQUATIONS

The system Hamiltonian has the form $H = H\,(\,\mathbf{p}, \mathbf{c}, \mathbf{g}, \mathbf{e}\,)$ and the canonical Hamilton's equations are

$$\dot{\mathbf{p}} = -\frac{\partial H}{\partial \mathbf{c}} + \mathbf{f}^p, \qquad \dot{\mathbf{c}} = \frac{\partial H}{\partial \mathbf{p}} \tag{30}$$

and

$$\dot{\mathbf{g}} = -\frac{\partial H}{\partial \mathbf{e}} + \mathbf{f}^g, \qquad \dot{\mathbf{e}} = \frac{\partial H}{\partial \mathbf{g}} \tag{31}$$

where $\mathbf{f}^p$ and $\mathbf{f}^g$ are the nonpotential generalized forces associated with the virtual work and any applied constraints. The Euler parameter constraint has the rate form

$$\dot{\mathbf{e}}^T\mathbf{e} \;=\; 0 \tag{32}$$

Introducing a Lagrange multiplier λ, the latter constraint combines with the virtual work expression to yield

$$\mathbf{f}^p \;=\; \mathbf{f}(t) \tag{33}$$

$$\mathbf{f}^g \;=\; 2\,\mathbf{G}^T\mathbf{T}(t) + \lambda\mathbf{e} \tag{34}$$

so that for the derived Hamiltonian the momentum balance equations are

$$\dot{\mathbf{p}} \;=\; -\frac{\partial V}{\partial \mathbf{c}} + \mathbf{f}(t) \tag{35}$$

$$\dot{\mathbf{g}} \;=\; -\frac{\partial V}{\partial \mathbf{e}} + \mathbf{k} + 2\,\mathbf{G}^T\mathbf{T}(t) + \lambda\mathbf{e} \tag{36}$$

The last equation includes an unknown Lagrange multiplier and a superfluous momentum variable. These variables are eliminated by introducing the three-momentum vector

$$\mathbf{h} = \mathbf{J}\,\boldsymbol{\omega} \tag{37}$$

whose time derivative is

$$\dot{\mathbf{h}} = \frac{1}{2}\mathbf{G}\dot{\mathbf{g}} + \frac{1}{2}\dot{\mathbf{G}}\mathbf{g} \tag{38}$$

With equations (11) and (36) this yields

$$\dot{\mathbf{h}} = \frac{1}{2}\dot{\mathbf{G}}\mathbf{g} + \frac{1}{2}\mathbf{G}\mathbf{k} + \mathbf{T}(t) - \frac{1}{2}\mathbf{G}\frac{\partial V}{\partial \mathbf{e}} \tag{39}$$

or

$$\dot{\mathbf{h}} = -\frac{1}{2}\boldsymbol{\Omega}\mathbf{h} + \frac{1}{2}\mathbf{G}\mathbf{k} + \mathbf{T}(t) - \frac{1}{2}\mathbf{G}\frac{\partial V}{\partial \mathbf{e}} \tag{40}$$

which eliminates both λ and the four component momentum vector.

The final unconstrained Hamiltonian model is

$$\dot{\mathbf{p}} = -\frac{\partial V}{\partial \mathbf{c}} + \mathbf{f}(t) \tag{41}$$

$$\dot{\mathbf{h}} = -\boldsymbol{\Omega}\mathbf{h} - \frac{1}{2}\mathbf{G}\frac{\partial V}{\partial \mathbf{e}} + \mathbf{T}(t) \tag{42}$$

$$\dot{\mathbf{c}} = m^{-1}\,\mathbf{p} \tag{43}$$

$$\dot{\mathbf{e}} = \frac{1}{2}\mathbf{G}^T\mathbf{J}^{-1}\mathbf{h} \tag{44}$$

Given a potential function and the virtual work, the preceding explicit equations may be integrated to simulate the system response.

As outlined in the introduction, the rigid body dynamics formulation derived here combines the advantages of Hamiltonian mechanics and Euler parameter kinematics. Hamiltonian and Lagrangian methods generally simplify the model formulation process, in particular when geometric nonlinearities are important. Such nonlinearities arise for example when large rotations or hyperelastic devices are of interest. As compared to Lagrangian methods, Hamiltonian methods offer an explicit state space description of the system dynamics, normally most convenient for numerical integration. Euler parameters offer a singularity free description of rotational displacements, and are therefore preferred over Euler angle models in large rotation applications. The cost is of course the need to integrate an additional state equation for each rigid body, since the Euler parameters are a quaternion. The present combination of Hamiltonian mechanics and Euler parameter kinematics is therefore of most interest in the formulation and numerical integration of models for strongly nonlinear mechanical systems. The model developed here is unique in its combination of features:

unconstrained, free of singularities, incorporating a general potential energy function, employing a minimum set of momentum variables, and taking an explicit state space form convenient for numerical implementation.

EXAMPLE PROBLEMS

Application of the Hamiltonian formulation developed here is illustrated in four examples. The first example compares an Euler angle based model of a rotating disk problem to the present Hamiltonian formulation, both to validate the present approach and to illustrate in a simple case an Euler parameter description of rotational displacement. The second example solves a classical rigid body dynamics problem for the three dimensional motion of a torque-free body, for comparison to the published numerical solution of Morton [6] and to the partial analytical solution of Thompson [16]. This problem again validates the present approach, and compares a discontinuous Euler angle description of three dimensional rigid body motion to the continuous Euler parameter characterization adopted here. The third example models a spinning top in a uniform gravitational field, a problem described in many advanced dynamics tests, and validates the present formulation in a three dimensional rigid body motion involving both translation and rotation. Here a numerical solution for the last cited problem is obtained using a time step identical to that employed by Simo and Wong [14], but without resort to their symplectic integration algorithm. The last example considers a problem of practical importance in the design of gyroscopic seekers, namely the motion of a freely precessing body with a viscous ring nutation damper [2]. This example calls for the application of nonholonomic constraints. Here we develop an explicit state space model, as compared to the implicit Lagrangian formulation [2] of Chang et al.

The first example models the free vibration of a rigid circular disk of radius r, rotating about a fixed point, and attached to a linear spring of stiffness k (see Figure 1). The potential energy function is

$$V = \frac{1}{2}\, k\, y_p^2 = \frac{1}{2}\, k\, r^2\, [\, 2e_1e_2 + 2e_0e_3\,]^2 \tag{45}$$

where y_p denotes the vertical displacement of the point of attachment of the spring, measured in a Cartesian coordinate system whose origin lies at the center of the disk. Note that the indicated Euler parameter dependence of the potential energy is obtained using equation (5). Assuming the model parameters and initial conditions listed in Table 1, the motion was simulated by integration of a Newtonian model based on the Euler angle ϕ

$$J\ddot{\phi} + \frac{1}{2}\, k\, r\, sin(2\phi) = 0 \tag{46}$$

and by integration of the Hamiltonian relations (42) and (44). The two computed results for the angular momentum are compared in Figure 2, showing excellent agreement of the Euler angle based and Euler parameter based solutions. Figure 3 shows the computed variation of the Euler parameters with time.

The second example models the torque free motion of a rigid body, for the inertial properties and initial conditions listed in Table 2. A partial analytical solution for this classic problem is known and can be expressed in terms of elliptic functions [6,16]. Figures 4 and 5 shown the time variation of the angular momenta and Euler parameters computed using the present Hamiltonian formulation. Figure 6 plots the implied Euler angles, emphasizing the discontinuous nature of the latter variables. Table 3 shows excellent agreement of the analytical and numerical solutions for the amplitudes and periods of the angular momenta, in three dimensional motion.

The third example models the translational and rotational motion of a spinning top in a uniform gravitational field. This problem is described in many advanced dynamics texts [4], and is used by Simo and Wong [14] to evaluate their symplectic numerical integration scheme. The potential energy for the system is

$$V = W\, z_c \tag{47}$$

where W is the weight of the top and z_c is the vertical coordinate of the center of mass. The simulation parameters and initial conditions for the problem are listed in Table 4. Figures 7

and 8 show numerical results for the normalized angular momentum components and center of mass coordinates, obtained by integration of Hamilton's equations (41) through (44), using a fourth order Runge-Kutta method. Table 5 compares an approximate analytical estimate of the nutation and precession frequencies for the top, provided by Goldstein [4], to the present numerical results. The present numerical results are identical to those plotted by Simo and Wong [14], and are obtained using the same time step, but without resort to their symplectic integration scheme.

The fourth example considers the rotational motion of a rigid rotor damped by a partially filled mercury ring damper. The reader is referred to Chang et al. [2] for a detailed discussion of this problem, and its application in the analysis of gyroscopic seekers. We focus here on the formulation of a dynamic model for the system analyzed in reference [2]. The paragraphs which follow develop an explicit Hamiltonian model for this system, an alternative to the implicit Lagrangian model of Chang et al., adopting their stipulated assumptions on stored energy functions, energy dissipation, and kinematic constraints.

The rotor is modeled as a rigid circular cylinder with a fixed center of mass located at the origin of a global XYZ coordinate system. The partially filled mercury ring damper is a cylinder of mean radius R, co-axial with and external to the rotor, with a centroid displaced a distance L along the rotor axis from the rotor center of mass location. Body-fixed coordinate systems for the rotor (xyz) and ring (uvz) are co-located at the centroid of the damper, where the z direction is aligned with the rotor axis. The partial mercury ring is free to rotate about the rotor axis, subject to a damping torque which is linear in the axial angular velocity difference between the rotor and the ring, but is otherwise constrained to move with the rotor. Hence the orientations of the body-fixed axes systems which co-rotate with the rotor and the ring differ only by an angle β, which describes the axial rotation of the ring with respect to the rotor.

The assumed complimentary kinetic energy for the system is [2]

$$T^* = \frac{1}{2}\,\boldsymbol{\omega}^T \mathbf{J}^T\,\boldsymbol{\omega} + \frac{1}{2}\,\boldsymbol{\omega}_m^T \mathbf{J}_m^T\,\boldsymbol{\omega}_m \tag{48}$$

where $\boldsymbol{\omega}$ and $\boldsymbol{\omega}_m$ are angular velocities for the rotor and ring and

$$\mathbf{J} = \begin{bmatrix} J_1 & 0 & 0 \\ 0 & J_2 & 0 \\ 0 & 0 & J_3 \end{bmatrix}, \qquad \mathbf{J}_m = \begin{bmatrix} J_{m1} & 0 & -J_{m4} \\ 0 & J_{m2} & 0 \\ -J_{m4} & 0 & J_{m3} \end{bmatrix} \tag{49}$$

are constant moment of inertia matrices for the rotor and ring. All four quantities are described in the respective rotor and ring body-fixed co-rotating coordinate systems.

The assumed potential energy for the system, due to the gravitational potential of the mercury, is [2]

$$V = -\,m\,\mathbf{g}_c\,\mathbf{R}^T\,\mathbf{B}^T\mathbf{r}_c, \qquad \mathbf{r}_c = [R\,sin(\gamma/2)/(\gamma/2), 0, L]^T \tag{50}$$

where m is the mass of the mercury, $\mathbf{g}_c$ is a constant gravity acceleration vector described in the fixed XYZ frame, $\mathbf{R}$ is the rotation matrix of equation (6), whose Euler parameters ($\mathbf{e}$) refer to the rotor-fixed frame, $\mathbf{r}_c$ is a constant vector which locates the mercury center of mass, γ is the angle which subtends the mercury arc (symmetric about the u axis), and $\mathbf{B}$ is an orthogonal matrix which defines the transformation of vector components from the rotor-fixed to the ring-fixed frame

$$\mathbf{B} = \begin{bmatrix} cos(\beta) & sin(\beta) & 0 \\ -sin(\beta) & cos(\beta) & 0 \\ 0 & 0 & 1 \end{bmatrix} \tag{51}$$

Note that $V = V(\mathbf{e}, \beta)$. The virtual work for the system, due to damping at the ring-rotor interface, is [2]

$$\delta W = -\,C_d\,R^2\,\dot{\beta}\,\delta\beta \tag{52}$$

where C_d is an empirical dimensionless damping coefficient.

Given the preceding modeling assumptions, Hamilton's equations for the rotor and ring

system are

$$\dot{\mathbf{h}} = -\mathbf{\Omega h} - \frac{1}{2}\mathbf{G}\frac{\partial V}{\partial \mathbf{e}} + \mathbf{T} \tag{53}$$

$$\dot{\mathbf{h}}_m = -\mathbf{\Omega}_m \mathbf{h}_m + \mathbf{T}_m \tag{54}$$

$$\dot{\mathbf{e}} = \frac{1}{2}\mathbf{G}^T \mathbf{J}^{-1} \mathbf{h} \tag{55}$$

$$0 = -\frac{\partial V}{\partial \beta} + T_\beta \tag{56}$$

where $\mathbf{h}$ and $\mathbf{h}_m$ are angular momenta for the rotor and ring

$$\mathbf{h} = \mathbf{J}\,\boldsymbol{\omega}, \qquad \mathbf{h}_m = \mathbf{J}_m\,\boldsymbol{\omega}_m \tag{57}$$

and $\mathbf{T}$, $\mathbf{T}_m$, and T_β are nonpotential forces due to damping and kinematic constraints. Note that the degenerate form of Hamilton's equation for β is due to the fact that the latter generalized coordinate, which appears in the potential energy function, is not associated with a corresponding generalized momentum variable. The kinematic constraints are [2]

$$\omega_{m1} = cos(\beta)\,\omega_1 + sin(\beta)\,\omega_2, \qquad \omega_{m2} = -sin(\beta)\,\omega_1 + cos(\beta)\,\omega_2, \tag{58}$$

and

$$\dot{\beta} = \omega_{m3} - \omega_3 \tag{59}$$

They quantify the aforementioned modeling assumption that the ring moves relative to the rotor only in axial rotation.

An explicit state space model may be obtained by application of the constraints, as follows. Introducing a Lagrange multiplier μ for the constraint (59), and accounting for the virtual work, requires

$$T_\beta = \mu - C_d\,R^2\,\dot{\beta}, \qquad \mathbf{T} = \mu\,\mathbf{c}, \qquad \mathbf{T}_m = -\mu\,\mathbf{c} \tag{60}$$

where $\mathbf{c}$ denotes the vector $[0, 0, 1]^T$. The degenerate Hamilton's equation for β therefore determines the Lagrange multiplier as

$$\mu = C_d\,R^2\,\dot{\beta} + \frac{\partial V}{\partial \beta} \tag{61}$$

Hamilton's equation (54) for the ring angular momentum may now be written in the form

$$\dot{\boldsymbol{\omega}}_m = -\mathbf{J}_m^{-1}\boldsymbol{\Omega}_m\mathbf{J}_m\boldsymbol{\omega}_m - \mu\,\mathbf{J}_m^{-1}\mathbf{c} \tag{62}$$

Since the constraints specify both $\dot{\beta}$ and the first two components of the ring angular velocity vector as functions of the set $(\beta, \omega_1, \omega_2, \omega_{m3})$, the third of equations (62) is an evolution relation for the unknown ω_{m3}. Combining the third of equations (62) with the constraint equation (59), the constitutive relations (57), and Hamilton's equations (53) and (55), the result is an explicit state space model of order nine for the ring-rotor system. The final state equations are

$$\dot{\mathbf{h}} = -\boldsymbol{\Omega}\mathbf{h} - \frac{1}{2}\mathbf{G}\frac{\partial V}{\partial \mathbf{e}} + \left[C_d\,R^2\,\left(\omega_{m3} - \frac{h_3}{J_3}\right) + \frac{\partial V}{\partial \beta}\right]\mathbf{c} \tag{63}$$

$$\dot{\mathbf{e}} = \frac{1}{2}\mathbf{G}^T\mathbf{J}^{-1}\mathbf{h} \tag{64}$$

$$\dot{\beta} = \omega_{m3} - \frac{h_3}{J_3} \tag{65}$$

$$\dot{\omega}_{m3} = -\mathbf{c}^T\left(\mathbf{J}_m^{-1}\boldsymbol{\Omega}_m\mathbf{J}_m\boldsymbol{\omega}_m\right) - \left[C_d\,R^2\,\left(\omega_{m3} - \frac{h_3}{J_3}\right) + \frac{\partial V}{\partial \beta}\right]\mathbf{c}^T\mathbf{J}_m^{-1}\mathbf{c} \tag{66}$$

where

$$\boldsymbol{\Omega} = \boldsymbol{\Omega}(\mathbf{h}), \qquad \mathbf{G} = \mathbf{G}(\mathbf{e}), \qquad \boldsymbol{\Omega}_m = \boldsymbol{\Omega}_m(\boldsymbol{\omega}_m) \tag{67}$$

with

$$\omega_{m1} = cos(\beta)\,\frac{h_1}{J_1} + sin(\beta)\,\frac{h_2}{J_2}, \qquad \omega_{m2} = -sin(\beta)\,\frac{h_1}{J_1} + cos(\beta)\,\frac{h_2}{J_2} \tag{68}$$

Note that implicit model of reference [2] is also of order nine but employs a different set of state variables.

CONCLUSION

The present paper has derived and applied a new Hamiltonian formulation of rigid body dynamics problems, based on Euler parameter kinematics. Euler parameter kinematics provide a singularity free description of three dimensional rigid body motion, accommodating arbitrarily large rotations. When combined with Hamiltonian mechanics, the result is an

energy based modeling approach well suited to address problems with complex geometric nonlinearities. As compared to previous work, the formulation derived here offers a unique combination of features. It avoids the introduction of algebraic constraints and unspecified parameters, includes a general potential energy function, incorporates a minimum set of momentum variables, and takes an explicit state space form convenient for use in control related applications.

ACKNOWLEDGEMENTS

This work was supported by NASA Johnson Space Center (NAG9-1244), the National Science Foundation (CMS99-12475), and the State of Texas Advanced Research Program (003658-0709-1999). Computer time support was provided by the NASA Advanced Supercomputing Division (ARC) and the Texas Advanced Computing Center (UTA).

APPENDIX

A complimentary kinetic energy expression (T^*) with the functional form

$$T^* = T^*(\mathbf{e}, \mathbf{f}), \qquad \mathbf{f} = \dot{\mathbf{e}} \tag{69}$$

has the total differential

$$dT^* = \mathbf{g}^T d\mathbf{f} + \frac{\partial T^*}{\partial \mathbf{e}}^T d\mathbf{e}\,, \qquad \mathbf{g} = \frac{\partial T^*}{\partial \mathbf{f}} \tag{70}$$

The corresponding kinetic energy function (T) is determined by the Legendre transform

$$T = \mathbf{g}^T \mathbf{f} - T^* \tag{71}$$

and has a total differential defined by

$$dT = \mathbf{g}^T d\mathbf{f} + \mathbf{f}^T d\mathbf{g} - dT^* = \mathbf{f}^T d\mathbf{g} - \frac{\partial T^*}{\partial \mathbf{e}}^T d\mathbf{e} \tag{72}$$

as well as the canonical form

$$dT = \frac{\partial T}{\partial \mathbf{g}}^T d\mathbf{g} + \frac{\partial T}{\partial \mathbf{e}}^T d\mathbf{e} \tag{73}$$

It follows that

$$\mathbf{f} = \frac{\partial T}{\partial \mathbf{g}}\,, \qquad \frac{\partial T}{\partial \mathbf{e}} = -\frac{\partial T^*}{\partial \mathbf{e}} \tag{74}$$

REFERENCES

[1] Baruh, Haim, 1999, Analytical Dynamics, McGraw Hill, New York.

[2] Chang C.O., Chou, C.S., and Wang, S.Z., 1991, Design of a viscous ring nutation damper for a freely precessing body, *Journal of Guidance, Control and Dynamics*, **14**, pp. 1136-1144.

[3] Ginsberg, J.H., 1988, Advanced Engineering Dynamics, Harper and Row, New York.

[4] Goldstein, Herbert, 1965, Classical Mechanics, Addison-Wesley Publishing Company, New York.

[5] Greenwood, Donald T., 1988, Principles of Dynamics, Prentice Hall, Englewood Cliffs, New Jersey.

[6] Morton, Harold S., Jr., 1993, Hamiltonian and lagrangian formulations of rigid body rotational dynamics based on euler parameters, *The Journal of Astronautical Sciences*, **41**, pp. 561-5991.

[7] Nikravesh, P.E., and Chung, I.S., 1982, Application of euler parameters to the dynamic analysis of three dimensional constrained mechanical systems, *Journal of Mechanical Design*, **104**, pp. 785-791.

[8] Nikravesh, P.E., Wehage, R.A., and Kwon, O.K., 1985, Euler parameters in computational kinematics and dynamics: part 1, *Journal of Mechanisms, Transmissions and Automation Design*, **107**, pp. 358-365.

[9] Nikravesh, P.E., Kwon, O.K., and Wehage, R.A., 1985, Euler parameters in computational kinematics and dynamics: part 2, *Journal of Mechanisms, Transmissions and Automation Design*, **107**, pp. 366-369.

[10] Nikravesh, P.E., 1988, Computer aided analysis of Mechanical Systems, Prentice Hall, Englewood Cliffs, New Jersey.

[11] Nitschke, M., and Knickmeyer, E.H., 2000, Rotation parameters- a survey of techniques, *Journal of Surveying Engineering*, **126**, pp. 83-105.

[12] Rapaport, D.C., 1985, Molecular dynamics simulation using quaternions, *Journal of Computational Physics*, **41**, pp. 306-314.

[13] Shuster, M.D., 1993, A survey of attitude representations, *Journal of Astronautical Sciences*, **41**, pp. 531-543.

[14] Simo, J.C., and Wong, K.K., 1991, Unconditionally stable algorithms for rigid body dynamics that exactly preserve energy and momentum, *International Journal of Numerical methods in Engineering*, **31**, pp. 19-52.

[15] Spring, K.W., 1986, Euler parameters and the use of quaternion algebra in the manipulation of finite rotations: a review, *Mechanism and Machine Theory*, **21**, pp. 365-373.

[16] Thompson, W.T., 1961, Introduction to Space Dynamics, John Wiley and Sons, New York.

[17] Vadali, S.R., 1988, On the euler parameter constraint, *The Journal of Astronautical Sciences*, **36**, pp. 259-265.

Parameter	value
Mass moment of inertia $(kg\,m^2)$	$J = 2$
Radius of the disk (m)	$r = 1$
Stiffness of the spring (N/m)	$k = 10$
Initial displacement $(degrees)$	$\phi = 30$
Initial momentum $(kg\,m^2 rad/s)$	$h = 0$

Table 1: Model parameters and initial conditions for the first example problem

Parameter	value
Mass moments of inertia $(kg\,m^2)$	$J_1 = 400,\ J_2 = 307.808385,\ J_3 = 200$
Initial Euler parameters	$e_0 = 1,\ e_1 = e_2 = e_3 = 0$
Initial momenta $(kg\,m^2\,rad/s)$	$h_1 = 346.4101616,\ h_2 = 0,\ h_3 = -200$

Table 2: Model parameters and initial conditions for the second example problem

Variable	exact solution	numerical solution
Magnitude of h_1 $(kg\,m^2 rad/s)$	346.4102	346.38
Magnitude of h_2 $(kg\,m^2 rad/s)$	365.447	365.44
Magnitude of h_3 $(kg\,m^2 rad/s)$	200.0	199.975
Period of h_1 (s)	9.3393	9.35
Period of h_2 (s)	18.6786	18.68
Period of h_2 (s)	18.6786	18.68
Minimum of h_1 $(kg\,m^2 rad/s)$	162.6296	162.6342

Table 3: Exact versus numerical results for the second example problem

Parameter	value
Weight $(kg\,m/s^2)$	$W = 20$
Mass moment of inertia $(kg\,m^2)$	$J_1 = 5,\ J_2 = 5,\ J_3 = 1$
Initial Euler parameters	$e_0 = \cos(0.15),\ e_1 = \sin(0.15),\ e_3 = 0,\ e_4 = 0$
Initial angular momenta $(kg\,m^2 rad/s)$	$h_1 = 0,\ h_2 = 0,\ h_3 = 50$

Table 4: Simulation parameters and initial conditions for the third example problem

Variable	analytical approximation	numerical simulation
Nutation frequency (rad/s)	10.00	9.24
Precession frequency (rad/s)	0.40	0.4136

Table 5: Approximate analytical versus numerical results for the third example problem

LIST OF FIGURES

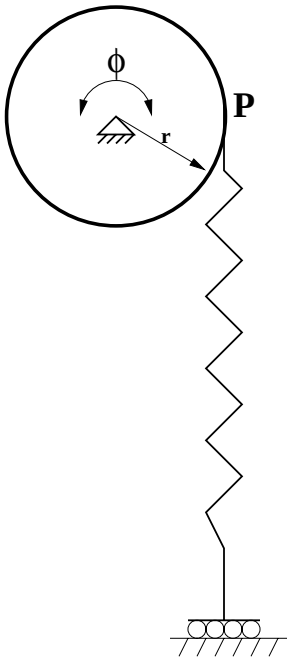

Figure 1: First example problem, rotating disk with a translational spring suspension

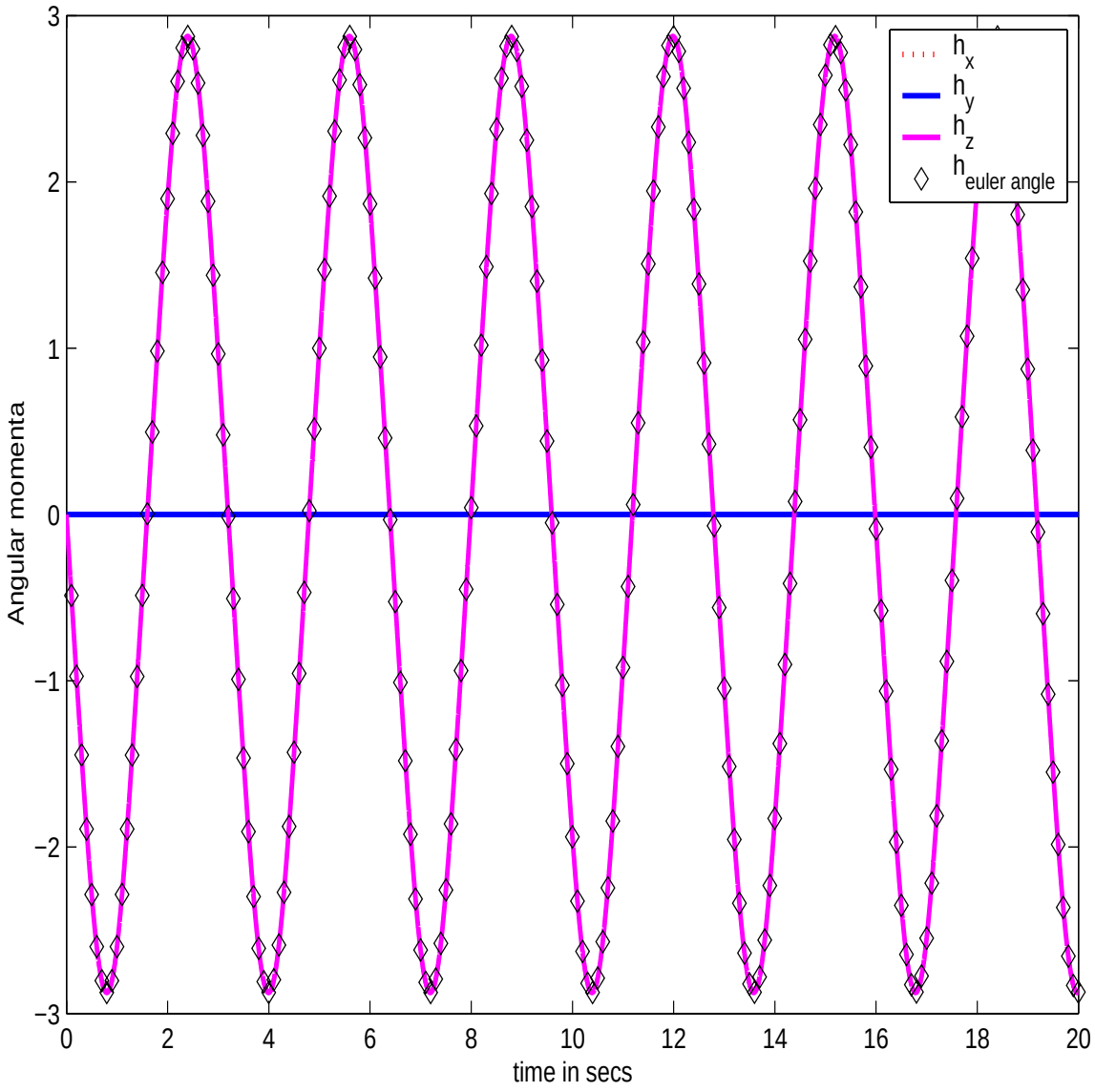

Figure 2: First example problem, comparison of Euler angle based and Hamiltonian solutions for the angular momenta versus time; the computed Hamiltonian component h_z agrees with the Euler angle solution (diamond symbols) obtained using equation (46), while the Hamiltonian components h_x and h_y are identically zero

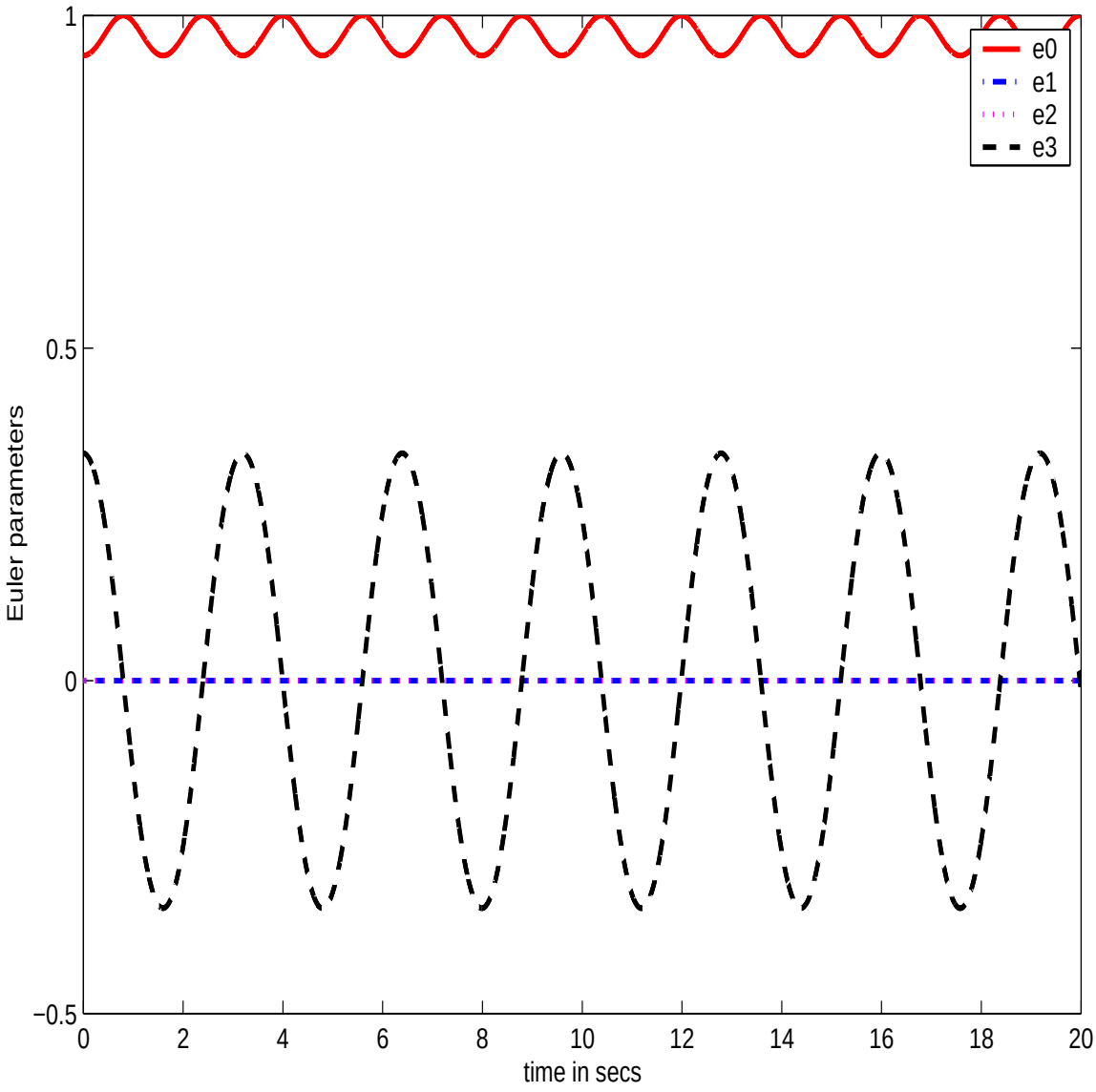

Figure 3: First example problem, numerical solution for the Euler parameters versus time; note that the Euler parameters e_1 and e_2 are identically zero, and along with the computed solutions for e_0 and e_3 determine the nonzero Euler angle in accordance with equation (2)

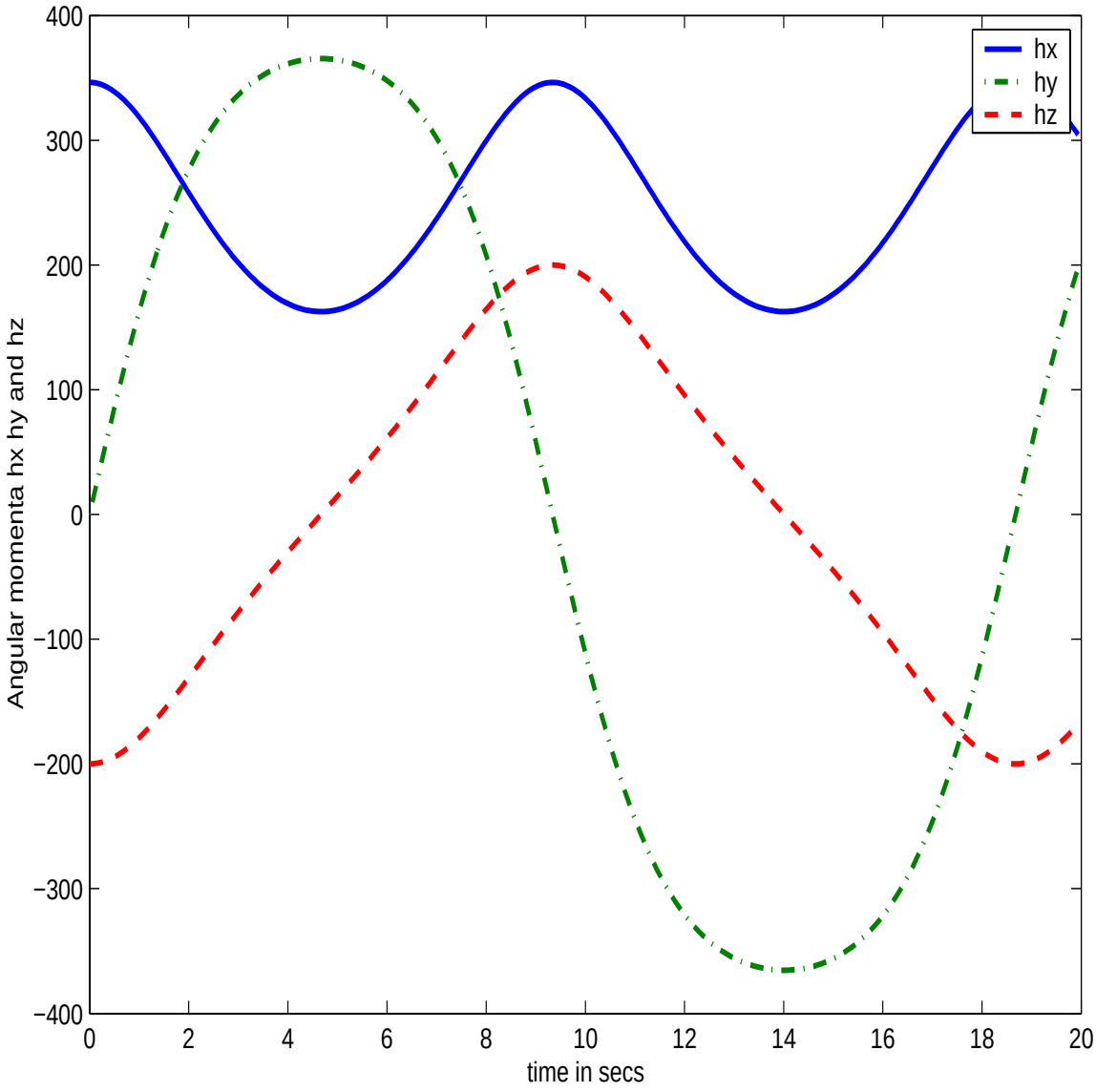

Figure 4: Second example problem, torque free motion of a rigid body, numerical solution for the angular momenta versus time

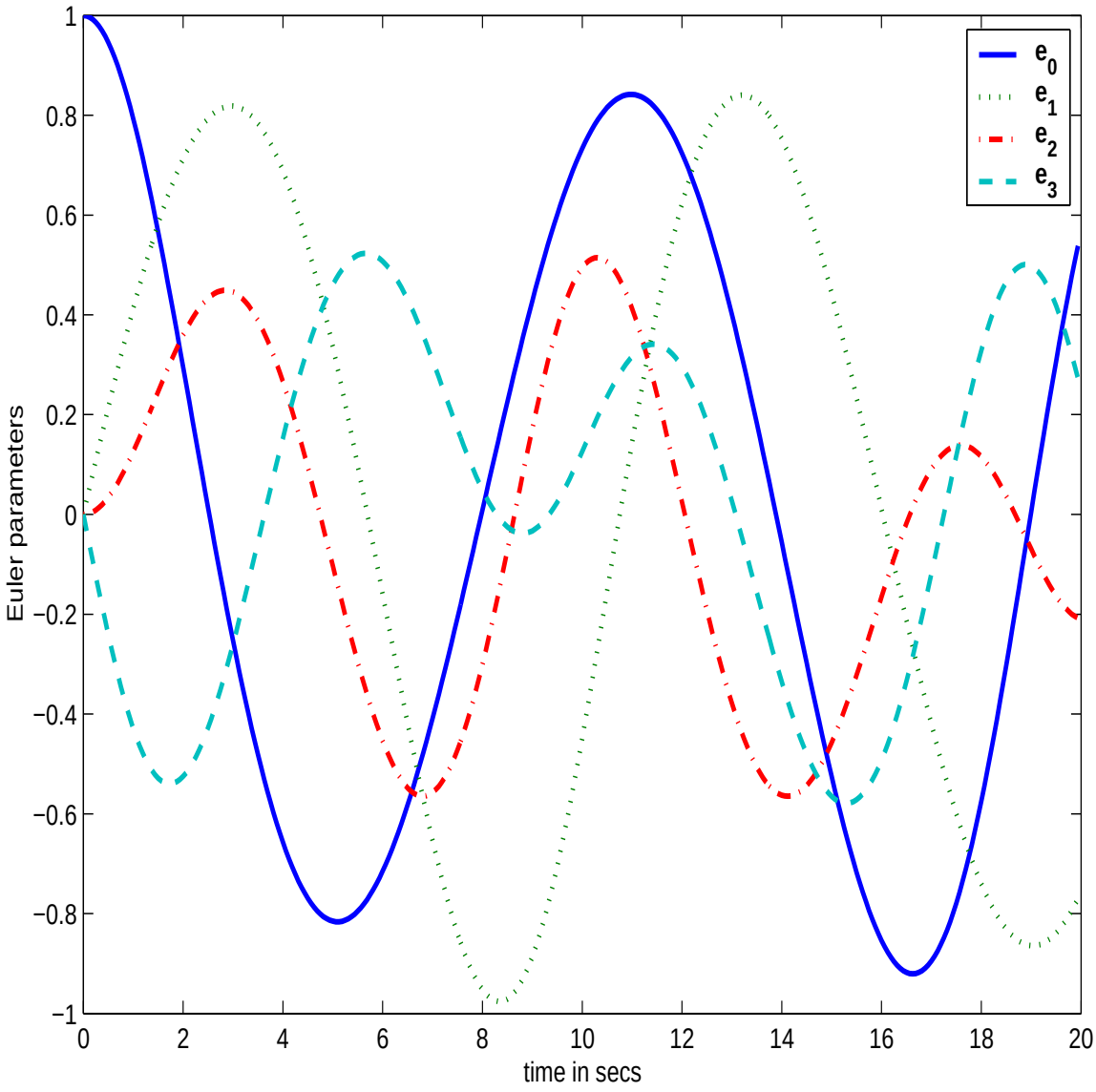

Figure 5: Second example problem, torque free motion of a rigid body, numerical solution for the Euler parameters versus time; note that the Euler parameters are continuous functions

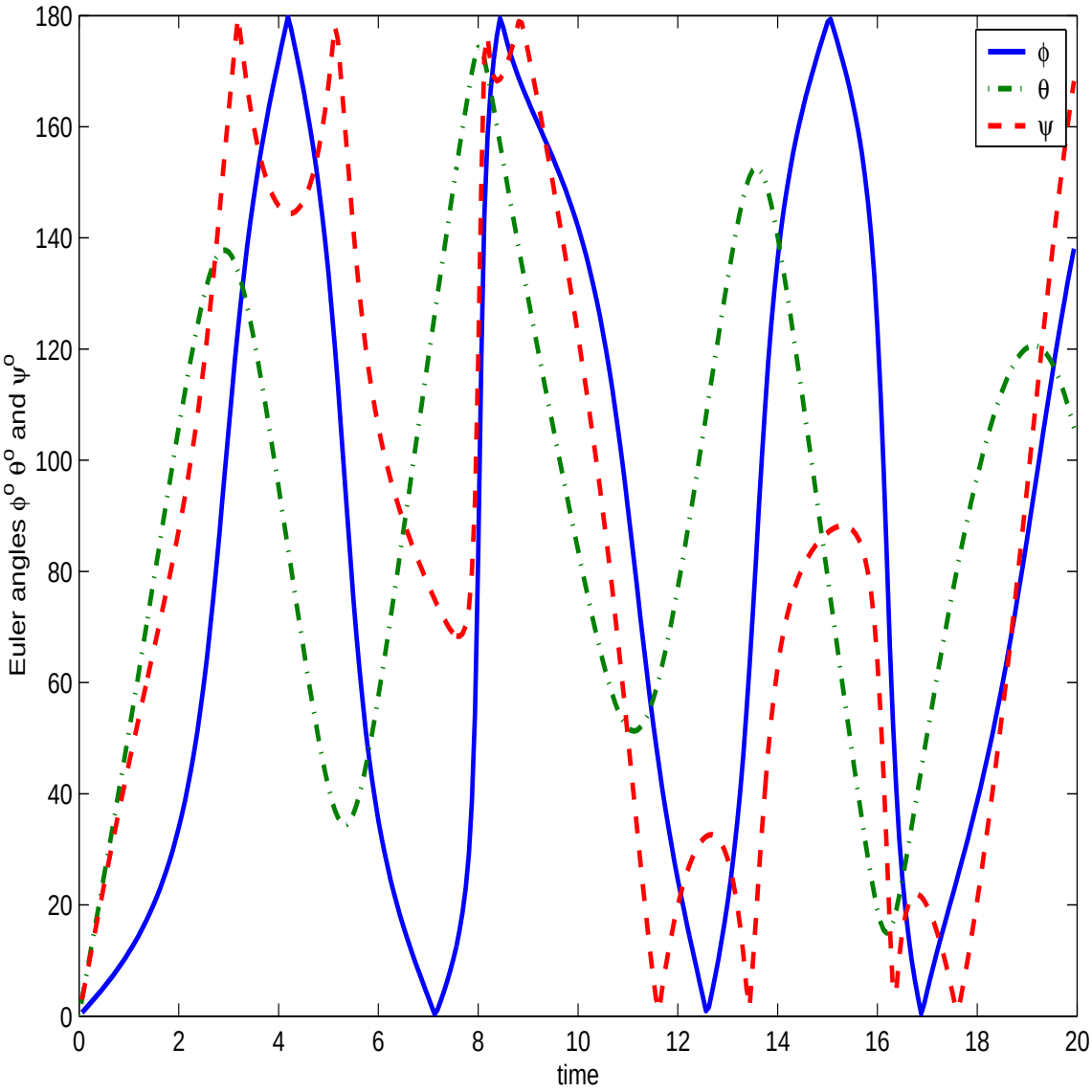

Figure 6: Second example problem, torque free motion of a rigid body, computed Euler angles versus time; note the discontinuities in the Euler angles

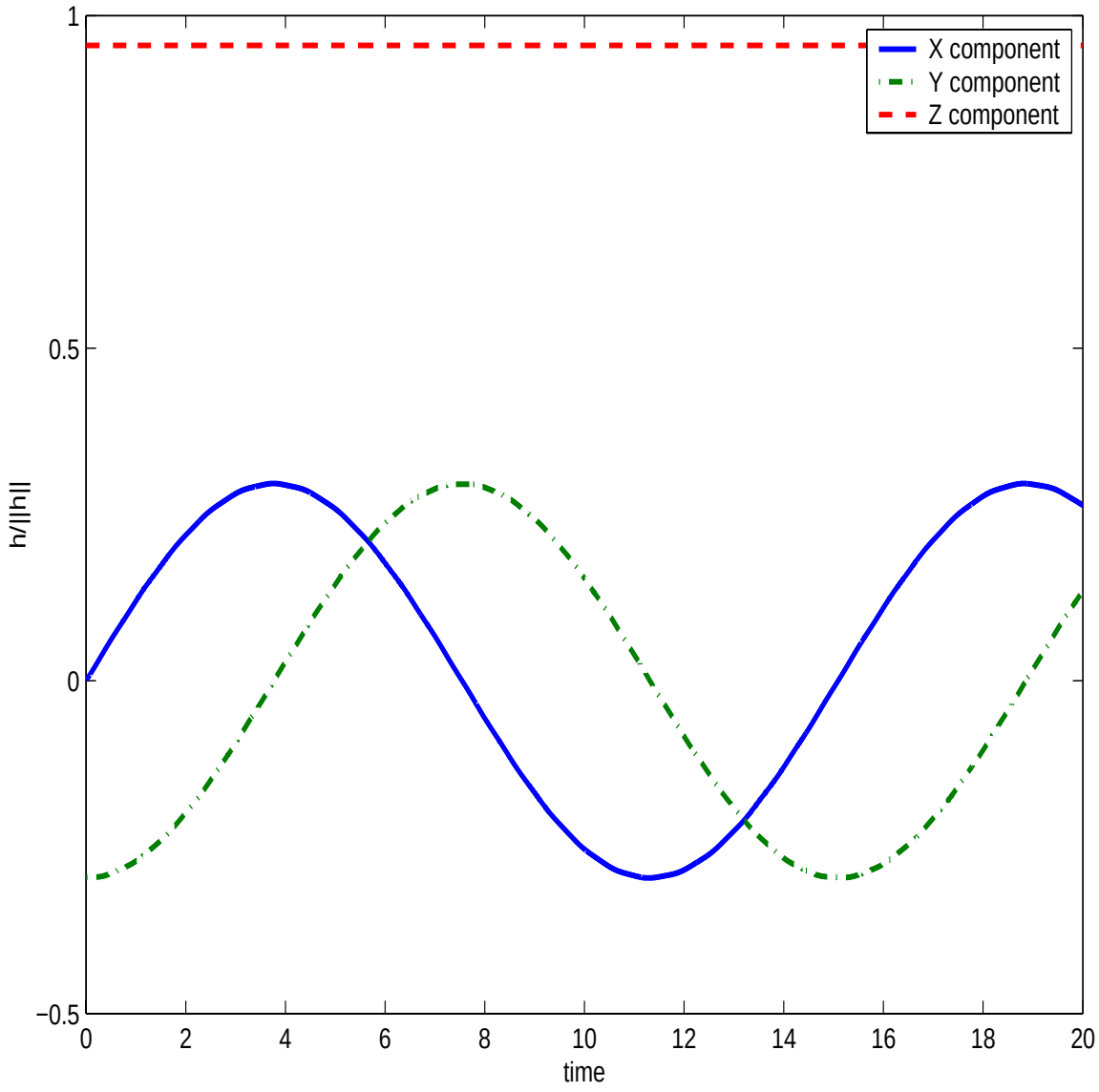

Figure 7: Third example problem, translation and rotation of a spinning top, numerical solution for the normalized components of the angular momentum versus time

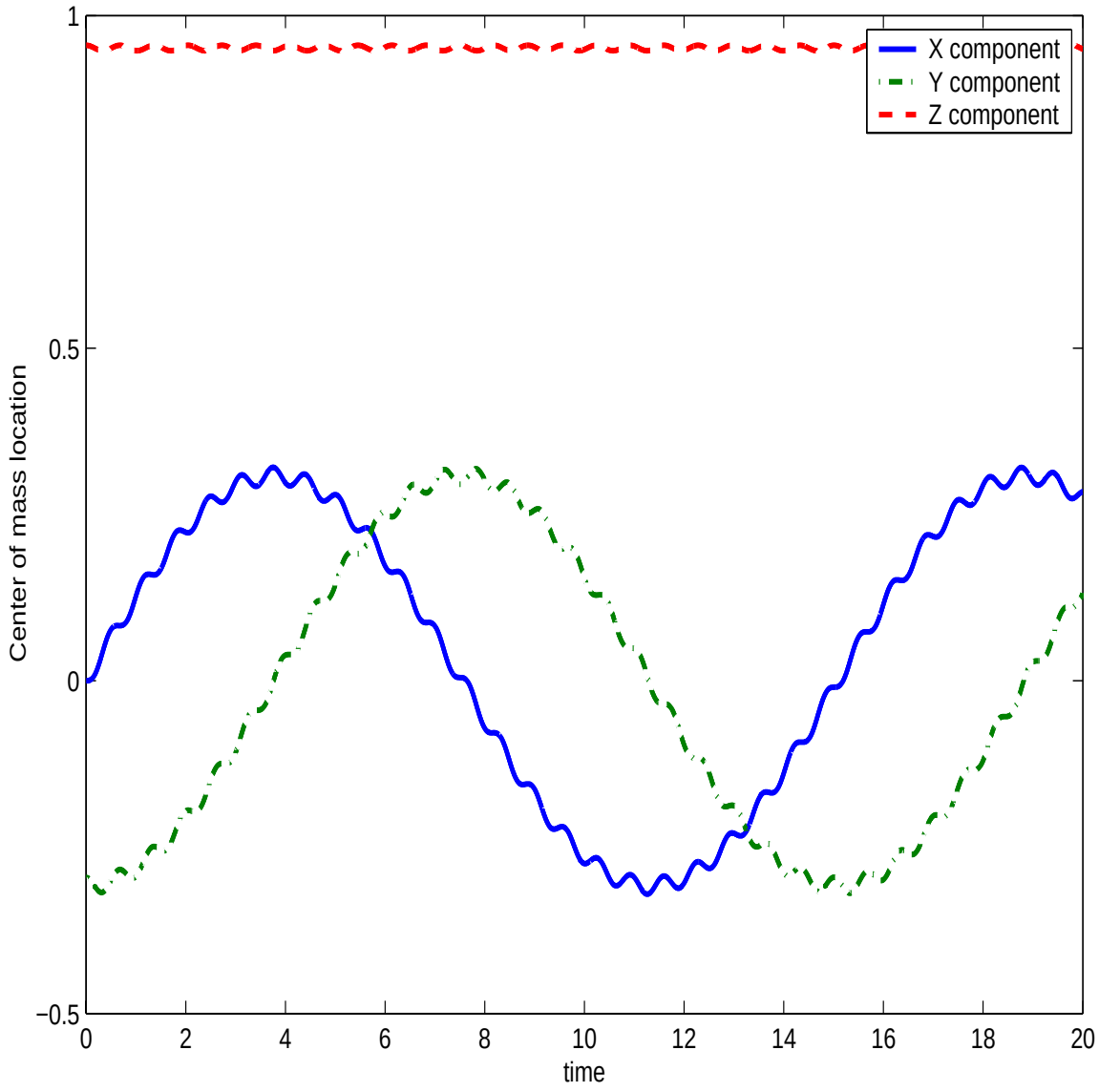

Figure 8: Third example problem, translation and rotation of a spinning top, numerical solution for the center of mass position versus time

CHAPTER 4

A KERNEL-FREE PARTICLE-FINITE ELEMENT METHOD FOR HYPERVELOCITY IMPACT SIMULATION

Young-Keun Park[1] **and Eric P. Fahrenthold**[2]

Department of Mechanical Engineering, 1 University Station C2200
University of Texas, Austin, TX 78712, USA

[1]Graduate student
[2]Professor, corresponding author, phone: (512) 471-3064, email: epfahren@mail.utexas.edu

A KERNEL FREE PARTICLE-FINITE ELEMENT METHOD FOR HYPERVELOCITY IMPACT SIMULATION

Young-Keun Park[3] **and Eric P. Fahrenthold**[4]

Department of Mechanical Engineering, 1 University Station C2200
University of Texas, Austin, TX 78712, USA

An improved hybrid particle-finite element method has been developed for the simulation of hypervelocity impact problems. Unlike alternative methods, the revised formulation computes the density without reference to any kernel or interpolation functions, for either the density or the rate of dilatation. This simplifies the state space model and leads to a significant reduction in computational cost. The improved method introduces internal energy variables as generalized coordinates in a new formulation of the thermomechanical Lagrange equations. Example problems show good agreement with exact solutions in one dimension and good agreement with experimental data in a three dimensional simulation.

KEYWORDS: particle methods, finite element methods, impact simulation

INTRODUCTION

Studies of hypervelocity impact phenomena are motivated by a variety of science and engineering applications [1]. Examples include scientific research on planetary impacts [2] and equations of state [3] and engineering research on the design of spacecraft shielding [4] and kinetic energy penetrators [5]. The proceedings of a recent international symposium [1] show that the use of computer simulation in this field is increasing, as improvements in numerical methods and computing power make it possible to address problems of greater complexity and larger scale. Simulation is of particular importance, as an adjunct to experimental work, when material costs are high [6] or when impact velocities beyond the range of light gas guns are of interest [7].

Simulation work in this field has applied a number of different numerical methods, based on continuum mechanics, particle dynamics, or mixed kinematic schemes. Continuum methods [8] employ either an Eulerian hydrodynamic [9,10] or a Lagrangian finite element [11]

[3]Graduate research assistant
[4]Professor, corresponding author, phone: (512) 471-3064, email: epfahren@mail.utexas.edu

approach, or some Arbitrary Lagrangian-Eulerian (ALE) based generalization of these techniques [12,13]. A large majority of particle codes employ a smooth particle hydrodynamics (SPH) technique [14,15,16], although some alternative particle based methods have been proposed [17]. Some disadvantages of pure continuum or pure particle based methods [18] have motivated the development of mixed continuum-particle formulations [4,19,20]. The most widely used mixed method is a coupled particle-finite element technique [19]. This technique initializes distinct material regions with either SPH particles or or Lagrangian finite elements, then quantifies subsequent material interactions using a particle-to-surface contact-impact algorithm. The alternative coupled particle-element method of Johnson and co-workers [20] maps damaged or failed elements into particles, and again quantifies particle-element interaction using a special contact algorithm. Both these methods are subject to tensile instability and numerical fracture problems.

The alternative mixed method of Fahrenthold and co-workers [21] is based on a hybrid particle-finite element formulation. This method in not subject to tensile instability and numerical fracture problems and eliminates the requirement for special treatment of particle-to-element contact-impact. It avoids both the mass diffusion problems of Eulerian methods and the mass and energy discard associated with Lagrangian element erosion algorithms. It is labeled a hybrid (versus coupled) method since it introduces both elements and particles for all material control volumes, then employs the elements and particles in tandem to represent distinct physics. The particles model all inertia, contact-impact, and thermomechanical response in compressed states, while the elements model tension and elastic-plastic shear. The method incorporates both ellipsoidal particles and time varying particle volumes and as a result can represent large density variations with relatively small neighbor counts. Previous work employing nonspherical evolving kernels has been rather limited and most particle simulations represent high densities using spherical particles, a fixed contact length, and relatively large neighbor sets.

The preceding formulation combines a true Lagrangian description of material strength

effects with a general particle based model of contact-impact dynamics, and has been validated in simulations of impact experiments conducted at velocities ranging from one to ten kilometers per second [22]. In the hypervelocity impact regime, where large strain plasticity, perforation, fragmentation, melting, and complex multi-structure contact-impact effects are often present, this formulation provides a particular combination of advantageous features not offered by alternative numerical methods. The present paper describes an improved hybrid particle-finite element method, modifying the formulation of Ravishankar and Fahrenthold [21] in two respects. First, the density is determined by integrating nonholonomic constraints imposed on the system level thermomechanical model. Second, the entropy states used previously to model the thermal domain are replaced by particle internal energies. These modifications simplify the method, reduce its computational cost, and incorporate equations of state expressed in standard functional form.

Unlike alternative methods, the revised formulation eliminates entirely the use of kernel or interpolation functions to represent the density or rate of dilatation fields. The density evolution equations are developed by direct reference to large deformation kinematics, avoiding any requirement to specify the functional dependence of an interaction potential on the particle coordinates. The latter task has proven to be quite difficult in an SPH context and is a principal focus of the general particle dynamics literature. The revised method introduces the use of internal energy variables as generalized coordinates in a new thermomechanical formulation of the discrete Lagrange equations. This avoids the requirement to construct Legendre transforms of the internal energy function, in order to express the dependence of pressure and temperature on entropy.

The present paper is organized as follows. First the particle and element kinematics are defined, followed by the kinetic co-energy and thermomechanical potential energy functions for the particle-element system. Second the evolution equations for the density are developed, followed by the evolution equations for the plastic and damage variables, all of these relations representing nonholonomic constraints on the system level model. Third the numerical

viscosity and numerical heat diffusion models are introduced, and evolution equations for the internal energy state variables are described, the latter states serving as generalized coordinates in a thermomechanical Lagrangian formulation. Fourth the discrete Lagrange equations for the particle-element system are derived, taking an explicit state space form convenient for numerical implementation. Finally application of the method is illustrated in one dimensional problems with exact solutions and in three dimensional simulations of representative hypervelocity impact problems.

PARTICLE KINEMATICS

The inertia of the modeled system is represented by a collection of n ellipsoidal particles, with $m^{(i)}$ the mass of particle i and $h_1^{(j)}, h_2^{(j)}, h_3^{(j)}$ the half-lengths of its major axes. The position and orientation of each particle is determined by its center of mass position vector ($\mathbf{c}^{(i)}$) and an Euler parameter [23,24] vector ($\mathbf{e}^{(i)}$)

$$\mathbf{c}^{(i)} = [\, c_1^{(i)}\; c_2^{(i)}\; c_3^{(i)}\,]^T, \qquad \mathbf{e}^{(i)} = [\, e_0^{(i)}\; e_1^{(i)}\; e_2^{(i)}\; e_3^{(i)}\,]^T \tag{1}$$

where a superscript T denotes the transpose.

It is convenient to note here certain properties of Euler parameters, and to cite a number of well known [23] kinematic relations associated with their use. The Euler parameters provide a singularity free description of arbitrary particle rotations. They define a rotation matrix ($\mathbf{R}^{(i)}$) for each particle

$$\mathbf{R}^{(i)} = \mathbf{A}^{(i)}\, \mathbf{G}^{(i)T} \tag{2}$$

$$\mathbf{A}^{(i)} = \begin{bmatrix} -e_1^{(i)} & e_0^{(i)} & -e_3^{(i)} & e_2^{(i)} \\ -e_2^{(i)} & e_3^{(i)} & e_0^{(i)} & -e_1^{(i)} \\ -e_3^{(i)} & -e_2^{(i)} & e_1^{(i)} & e_0^{(i)} \end{bmatrix} \tag{3}$$

$$\mathbf{G}^{(i)} = \begin{bmatrix} -e_1^{(i)} & e_0^{(i)} & e_3^{(i)} & -e_2^{(i)} \\ -e_2^{(i)} & -e_3^{(i)} & e_0^{(i)} & e_1^{(i)} \\ -e_3^{(i)} & e_2^{(i)} & -e_1^{(i)} & e_0^{(i)} \end{bmatrix} \tag{4}$$

which relates vector components $\mathbf{v}$ described in a fixed global Cartesian coordinate system to corresponding components $\hat{\mathbf{v}}$ described in a co-rotating system aligned with the particle major axes, using

$$\mathbf{v} = \mathbf{R}^{(i)}\,\hat{\mathbf{v}} \tag{5}$$

The Euler parameters and their time derivatives are related to the angular velocity vector of the particle ($\boldsymbol{\omega}^{(i)}$), described in the co-rotating frame, by

$$\dot{\mathbf{e}}^{(i)} = \frac{1}{2}\,\mathbf{G}^{(i)T}\,\boldsymbol{\omega}^{(i)} \tag{6}$$

Similarly the antisymmetric matrix $\boldsymbol{\Omega}^{(i)}$ with axial vector $\boldsymbol{\omega}^{(i)}$, which satisfies

$$\boldsymbol{\Omega}^{(i)}\mathbf{v} = \boldsymbol{\omega}^{(i)} \times \mathbf{v} \tag{7}$$

for all vectors $\mathbf{v}$, is related to the Euler parameters and their time derivatives by the relations

$$\boldsymbol{\Omega}^{(i)} = 2\,\mathbf{G}^{(i)}\,\dot{\mathbf{G}}^{(i)T} = -2\,\dot{\mathbf{G}}^{(i)}\mathbf{G}^{(i)T} = \mathbf{R}^{(i)T}\,\dot{\mathbf{R}}^{(i)} \tag{8}$$

For ellipsoidal particles it is convenient to describe the separation distance of the mass centers for particles i and j using the ellipsoidal coordinate

$$\zeta^{(i,j)} \;=\; \left[\, \left(\mathbf{c}^{(i)} - \mathbf{c}^{(j)}\right)^T \hat{\mathbf{H}}^{(j)} \left(\mathbf{c}^{(i)} - \mathbf{c}^{(j)}\right) \,\right]^{\frac{1}{2}} \tag{9}$$

defined in the co-rotating system of particle j using

$$\hat{\mathbf{H}}^{(j)} = \mathbf{R}^{(j)}\mathbf{H}^{(j)}\mathbf{R}^{(j)^T} \tag{10}$$

$$\mathbf{H}^{(j)} = \begin{bmatrix} 2\beta h_1^{(j)} & 0 & 0 \\ 0 & 2\beta h_2^{(j)} & 0 \\ 0 & 0 & 2\beta h_3^{(j)} \end{bmatrix}^{-2} \tag{11}$$

where the constant β allows for close packing at the reference density. The time derivative of this ellipsoidal coordinate , defined for $i \neq j$, is

$$\dot{\zeta}^{(i,j)} = \frac{1}{\zeta^{(i,j)}} \left[\left(\hat{\mathbf{H}}^{(j)}\mathbf{r}^{(i,j)}\right)^T \dot{\mathbf{r}}^{(i,j)} + \left(\mathbf{H}^{(j)}\hat{\mathbf{r}}^{(i,j)} \times \hat{\mathbf{r}}^{(i,j)}\right)^T \boldsymbol{\omega}^{(j)} \right] \tag{12}$$

where

$$\mathbf{r}^{(i,j)} = \mathbf{c}^{(i)} - \mathbf{c}^{(j)}, \qquad \hat{\mathbf{r}}^{(i,j)} = \mathbf{R}^{(j)T}\mathbf{r}^{(i,j)} \tag{13}$$

and may be used to quantify the rate of compression for an array of ellipsoidal particles.

The preceding results will be used in later sections to account for rotational inertia and particle kinematics not present in the vast majority of particle models, which assume a spherical particle geometry.

FINITE ELEMENT KINEMATICS

This section describes the finite element kinematics employed in the present paper. The elements used here are eight noded hexahedra, well known and described in detail by Hallquist [11] and others. Since all inertia effects are represented by the particles, no mass matrix is defined.

Each structure in the model is subdivided into uniform hexahedra with orthogonal faces, with ellipsoidal particles located at each node and at the centroid of each element. The center of mass coordinates for particles located at element vertices are also nodal coordinates for the hexahedra, and are used to compute the shearing strain. The center of mass coordinates for particles located at the element centroids are used, in combination with the nodal coordinates, to define six subelements for each hexahedron. The volumes of these subelements are used to compute interparticle tension forces.

The following Lagrangian finite strain deformation measures [25] are used in the stored energy functions for the elements, associated with tension and shear, and in the plastic constitutive relations. The shear strain for element j is

$$\overline{\mathbf{E}}^{(j)} = \frac{1}{2}\left(\overline{\mathbf{C}}^{(j)} - \mathbf{I}\right) \tag{14}$$

where

$$\overline{\mathbf{C}}^{(j)} = \overline{\mathbf{F}}^{(j)T}\overline{\mathbf{F}}^{(j)}, \qquad \overline{\mathbf{F}}^{(j)} = \left(det\,\mathbf{F}^{(j)}\right)^{-\frac{1}{3}}\mathbf{F}^{(j)} \tag{15}$$

and $\mathbf{F}^{(j)}$ is an element deformation gradient computed using one point integration [11]. The

elastic shear strain is defined as

$$\mathbf{E}^{e(j)} = \overline{\mathbf{E}}^{(j)} - \mathbf{E}^{p(j)} \tag{16}$$

where $(\mathbf{E}^{p(j)})$ is a plastic stain tensor whose flow rule satisfies the isochoric plastic deformation constraint

$$tr\left(\mathbf{C}^{p(j)-T}\dot{\mathbf{C}}^{p(j)}\right) = 0, \qquad \mathbf{E}^{p(j)} = \frac{1}{2}\left(\mathbf{C}^{p(j)} - \mathbf{I}\right) \tag{17}$$

The subelement Jacobians are denoted by $J^{(j,k)}$, where the index k designates one of six subelements for the jth hexahedron.

KINETIC CO-ENERGY AND POTENTIAL ENERGY

An energy method (Lagrange's equations) is adopted here, to facilitate the systematic integration of diverse particle and element based modeling concepts. The stored energy functions considered here are a kinetic co-energy function for the particles, an internal energy function for the particles, and element potential energy functions which account for tension and shear. Damage variables are introduced to model element failure in a thermodynamically consistent fashion. Constitutive assumptions different from those adopted here may be introduced without change to the underlying methodology.

The system kinetic co-energy is the sum of the particle co-energies

$$T^* \;=\; \sum_{i=1}^{n} T^{*(i)} \tag{18}$$

where $T^{*(i)}$ is the co-energy for particle i, due to translation and rotation

$$T^{*(i)} = \frac{1}{2}\, m^{(i)}\, \dot{\mathbf{c}}^{(i)\,T} \dot{\mathbf{c}}^{(i)} \;+\; \frac{1}{2}\, \boldsymbol{\omega}^{(i)\,T}\, \mathbf{J}^{(i)}\, \boldsymbol{\omega}^{(i)} \tag{19}$$

with $\mathbf{J}^{(i)}$ a constant moment of inertia matrix described in the co-rotating particle frame. The system kinetic co-energy function defines the generalized momenta

$$\mathbf{p}^{(i)} = \frac{\partial T^*}{\partial \dot{\mathbf{c}}^{(i)}} = m^{(i)}\, \dot{\mathbf{c}}^{(i)}\,, \qquad \mathbf{h}^{(i)} = \frac{\partial T^*}{\partial \boldsymbol{\omega}^{(i)}} = \mathbf{J}^{(i)}\, \boldsymbol{\omega}^{(i)} \tag{20}$$

where $\mathbf{p}^{(i)}$ and $\mathbf{h}^{(i)}$ are translational and angular momentum vectors for the ith particle.

The system potential energy has the general form

$$V = \sum_{i=1}^{n} U^{(i)} + \sum_{j=1}^{n_e} V_o^{e(j)}\, \psi^{(j)} + \sum_{j=1}^{n_e} \sum_{k=1}^{n_s} V_o^{e(j,k)}\, \psi^{(j,k)} \tag{21}$$

where $U^{(i)}$ is the total internal energy for particle i and the pressure ($P^{(i)}$) and temperature ($\theta^{(i)}$) are described by an equation of state [26] with functional form

$$P^{(i)} = P^{(i)}(\rho^{(i)}, u^{(i)}), \qquad \theta^{(i)} = \theta^{(i)}(\rho^{(i)}, u^{(i)}) \tag{22}$$

with $\rho^{(i)}$ and $u^{(i)}$ the density and the internal energy per unit mass

$$u^{(i)} = \frac{U^{(i)}}{m^{(i)}} \tag{23}$$

The second term depends on the number of elements (n_e), the reference volume ($V_o^{e(j)}$) for element j, and the strain energy per unit volume in shear ($\psi^{(j)}$), here assumed to be

$$\psi^{(j)} = (1 - d^{(j)})\, \mu^{(j)}\, tr\left(\mathbf{E}^{e(j)^T} \mathbf{E}^{e(j)}\right) \tag{24}$$

where $d^{(j)}$ is a shear damage variable and $\mu^{(j)}$ is a shear modulus. The third term depends on the number of subelements per element (n_s), the subelement reference volumes ($V_o^{e(j,k)}$), and the strain energy per unit volume in tension ($\psi^{(j,k)}$), here assumed to be

$$\psi^{(j,k)} = \frac{1}{2}\,(1 - D^{(j)})\, K^{(j)}\ < J^{(j,k)} - 1 >^2 \tag{25}$$

where $D^{(j)}$ is a normal damage variable, $K^{(j)}$ is a bulk modulus, $< x >$ denotes the bracket function

$$< x > = \ x\, \hat{u}(x) \tag{26}$$

and $\hat{u}$ denotes the unit step function. Since the subelement Jacobians and the shear strain tensor depend on the particle center of mass coordinates

$$J^{(j,k)} = J^{(j,k)}\left(\mathbf{c}^{(i)}\right), \qquad \mathbf{E}^{e(j)} = \mathbf{E}^{e(j)}\left(\mathbf{c}^{(i)}, \mathbf{E}^{p(j)}\right) \tag{27}$$

it follows that the system potential energy has the general functional form

$$V = V\left(\rho^{(i)}, U^{(i)}, \mathbf{c}^{(i)}, d^{(j)}, D^{(j)}, \mathbf{E}^{p(j)}\right) \tag{28}$$

The system potential energy defines the generalized conservative forces

$$m^{(i)}\frac{P^{(i)}}{\rho^{(i)2}} = \frac{\partial V}{\partial \rho^{(i)}}, \qquad \mathbf{g}^{(i)} = \frac{\partial V}{\partial \mathbf{c}^{(i)}}, \qquad 1 = \frac{\partial V}{\partial U^{(i)}} \tag{29}$$

as well as the deviatoric stress

$$\mathbf{S}^{(j)} = -\frac{1}{V_o^{e(j)}}\,\frac{\partial V}{\partial \mathbf{E}^{p(j)}} \tag{30}$$

and the strain energy release rates

$$\Gamma^{D(j)} = -\frac{\partial V}{\partial D^{(j)}}, \qquad \Gamma^{d(j)} = -\frac{\partial V}{\partial d^{(j)}} \tag{31}$$

due to damage evolution. Note that when the internal energy is introduced as a generalized coordinate, the associated generalized forces are constant.

With the system Lagrangian now defined, the next four sections describe evolution equations for the internal state variables.

DENSITY EVOLUTION RELATIONS

This section derives density evolution relations for the particles, by extending certain exact results for the deformation kinematics of a unit cell of spherical particles, arranged in a body centered cubic packing scheme. For uniform compression of such a unit cell, in isolation, the cell center density $\rho^{(i)}$ is related to the reference density ${\rho_o}^{(i)}$, the center of mass separation distances $r^{(i,j)}$ and particle radii $h^{(j)}$ for its eight neighbors by

$$\frac{\rho^{(i)}}{\rho_o^{(i)}} = 1 \;+\; \frac{1}{8}\sum_{j=1}^{8}\left[\left(\frac{2\beta h^{(j)}}{r^{(i,j)}}\right)^3 - 1\right] \tag{32}$$

If the particles are not spherical but ellipsoidal then

$$\frac{\rho^{(i)}}{\rho_o^{(i)}} = 1 \;+\; \frac{1}{8}\sum_{j=1}^{8}\left[\left(\frac{1}{\zeta^{(i,j)}}\right)^3 - 1\right] \tag{33}$$

This expression for an isolated cell may be extended to a cell array of arbitrary size by describing the same kinematics in rate form. Taking the time derivative of the last equation

and multiplying by a step function $W^{(i,j)}$ which allows for contact with near neighbors only yields

$$\frac{\dot{\rho}^{(i)}}{{\rho_o}^{(i)}} = -\frac{3}{8} \sum_{j=1}^{n} \frac{\dot{\zeta}^{(i,j)}}{\zeta^{(i,j)4}} W^{(i,j)} \tag{34}$$

where the summation is now over all n particles. The coefficient $W^{(i,j)}$ must satisfy

$$W^{(i,j)} = \begin{cases} 0 & \text{if } i = j \\ 0 & \text{if } i \neq j \text{ and } {\zeta^{(i,j)}}^3 \geq \frac{\rho_o^{(i)}}{\rho^{(i)}} \\ 1 & \text{if } i \neq j \text{ and } {\zeta^{(i,j)}}^3 < \frac{\rho_o^{(i)}}{\rho^{(i)}} \end{cases}$$

in order to correctly reflect the dependence of particle contact distance on the local density. Otherwise particles will contact remote neighbors through intervening matter. Hence

$$W^{(i,j)} = (1 - \delta_{ij})\, \hat{u} \left(1 - \zeta^{(i,j)} \left[\frac{\rho^{(j)}}{{\rho_o}^{(j)}} \right]^{1/3} \right) \tag{35}$$

where δ_{ij} denotes the Kronecker delta. Note that $W^{(i,j)}$ performs no interpolation. Introducing the kinematic relation for $\dot{\zeta}^{(i,j)}$, developed in an earlier section, yields

$$\dot{\rho}^{(i)} = -\frac{3}{8} \sum_{j=1}^{n} {\rho_o}^{(i)} \frac{W^{(i,j)}}{\zeta^{(i,j)5}} \left[\left(\hat{\mathbf{H}}^{(j)} \mathbf{r}^{(i,j)} \right)^T \dot{\mathbf{r}}^{(i,j)} + \left(\mathbf{H}^{(j)} \hat{\mathbf{r}}^{(i,j)} \times \hat{\mathbf{r}}^{(i,j)} \right)^T \boldsymbol{\omega}^{(j)} \right] \tag{36}$$

which is the constraint form of the density evolution relations. The coefficients of the particle translational velocities and angular velocities in this expression will determine generalized forces in the momentum balance (Lagrange) equations derived in a later section. When the particle velocities in this expression are eliminated in favor of the particle momenta

$$\dot{\mathbf{c}}^{(i)} = m^{(i)-1} \mathbf{p}^{(i)}, \qquad \boldsymbol{\omega}^{(i)} = \mathbf{J}^{(i)-1} \mathbf{h}^{(i)} \tag{37}$$

the density evolution equations take an explicit state space form convenient for use in numerical simulation.

PLASTICITY AND DAMAGE MODELS

This section introduces evolution equations for the plastic and damage variables. As in the case of the potential energy, alternative constitutive assumptions may be introduced without

change to the basic modeling methodology. The plastic flow rule used here is adapted from reference [27], and represents the simplest possible accommodation of the aforementioned isochoric plastic deformation constraint. The flow rule is

$$\dot{\mathbf{E}}^{p(j)} = \frac{\dot{\lambda}^{(j)}}{||S^{p(j)}||} \underline{\underline{\mathbf{N}}}^{p(j)} \underline{\underline{\mathbf{N}}} \, \mathbf{S}^{p(j)} \tag{38}$$

where $\dot{\lambda}^{(j)}$ is a positive proportionality coefficient, $\mathbf{S}^{p(j)}$ is an effective stress

$$\mathbf{S}^{p(j)} = \underline{\underline{\mathbf{N}}}^{T} \, \underline{\underline{\mathbf{N}}}^{p(j)T} \, \mathbf{S}^{(j)} \tag{39}$$

and the invariant operator is defined by

$$||\mathbf{T}|| = \left[\frac{1}{2} \, tr \left(\mathbf{T}^T \mathbf{T} \right) \right]^{1/2} \tag{40}$$

for any second order tensor $\mathbf{T}$. The fourth order tensor coefficients in the flow rule are defined by

$$\underline{\underline{\mathbf{N}}}^{p(j)} \, \mathbf{T} = \frac{1}{2 \, ||C^{p(j)}||} (\mathbf{C}^{p(j)} \, \mathbf{T} + \mathbf{T} \, \mathbf{C}^{p(j)}) \tag{41}$$

$$\underline{\underline{\mathbf{N}}} \, \mathbf{T} = \mathbf{T} - \frac{1}{3} tr(\mathbf{T}) \, \mathbf{I} \tag{42}$$

for any symmetric second order tensor $\mathbf{T}$. The yield function is

$$f^{(j)} = ||S^{p(j)}|| - Y^{(j)} \tag{43}$$

where $Y^{(j)}$ is the yield stress

$$Y^{(j)} = Y_o^{(j)} \, (1 - d^{(j)}) \, (1 + \kappa^{(j)} \epsilon^{p(j)})^{\alpha^{(j)}} \, \left(1 - \eta^{(j)} \theta^{H(j)} \right) \tag{44}$$

with $\epsilon^{p(j)}$ the effective plastic strain, $\kappa^{(j)}$ a strain hardening coefficient, $\alpha^{(j)}$ a strain hardening exponent, $\eta^{(j)}$ a thermal softening coefficient, and $\theta^{H(j)}$ the homologous temperature. The effective plastic strain is determined by integrating the rate relation

$$\dot{\epsilon}^{p(j)} = ||\dot{\mathbf{E}}^{p(j)}|| \tag{45}$$

while the incremental plastic strain for a time step Δt is computed using

$$\Delta\lambda^{(j)} = \frac{< ||S^{p(j)}|| - Y^{(j)} >}{(1 - d^{(j)})\, 2\, \mu^{(j)}} \tag{46}$$

The damage evolution equations applied here are adapted from reference [28], and dissipate the strain energy stored in tension and shear over $\hat{n}$ time steps, once an element meets any stipulated material failure criteria. The evolution equations are

$$\dot{D}^{(j)} = \frac{\Lambda^{(j)}}{\hat{n}\, \Delta t}\, \hat{u}(1 - D^{(j)}), \qquad \dot{d}^{(j)} = \frac{\Lambda^{(j)}}{\hat{n}\, \Delta t}\, \hat{u}(1 - d^{(j)}) \tag{47}$$

where $\Lambda^{(j)}$ is initialized to zero, and is set to a value of one when the accumulated plastic strain, temperature, or element compression reach corresponding critical values for the plastic failure strain ($\epsilon_f^{p(j)}$), melt temperature ($\theta_m^{(j)}$), or maximum compression ($J_c^{(j)}$). Other failure criteria may of course be specified.

In general terms, the plastic and damage evolution equations are noholonomic constraints of the form

$$\dot{\mathbf{E}}^{p(j)} = \dot{\mathbf{E}}^{p(j)} \left(\rho^{(i)}, U^{(i)}, \mathbf{c}^{(i)}, d^{(j)}, D^{(j)}, \epsilon^{p(j)}, \mathbf{E}^{p(j)}\right) \tag{48}$$

$$\dot{d}^{(j)} = \dot{d}^{(j)} \left(\rho^{(i)}, U^{(i)}, \mathbf{c}^{(i)}, d^{(j)}, D^{(j)}, \epsilon^{p(j)}, \mathbf{E}^{p(j)}\right) \tag{49}$$

$$\dot{D}^{(j)} = \dot{D}^{(j)} \left(\rho^{(i)}, U^{(i)}, \mathbf{c}^{(i)}, d^{(j)}, D^{(j)}, \epsilon^{p(j)}, \mathbf{E}^{p(j)}\right) \tag{50}$$

on the system level Lagrangian model.

ARTIFICIAL VISCOSITY AND HEAT DIFFUSION

Shock physics codes of the continuum or particle type incorporate a numerical viscosity and artificial heat diffusion. The forms used here are typical of particle codes, with one exception. Since the ellipsoidal particles used here admit rotational degrees of freedom, a viscous torque has been added which damps the relative rotation of neighboring particles.

A viscous force is introduced for converging particles only

$$\mathbf{f}^{(i)} = \sum_{j=1}^{n} \nu^{(i,j)}\, max\left(0, v^{(i,j)}\right)\, \frac{\left(\mathbf{c}^{(i)} - \mathbf{c}^{(j)}\right)}{|\,\mathbf{c}^{(i)} - \mathbf{c}^{(j)}\,|}\, \hat{u}(1 - \zeta^{(i,j)}) \tag{51}$$

where the relative normal velocity is

$$v^{(i,j)} = -\left(\dot{\mathbf{c}}^{(i)} - \dot{\mathbf{c}}^{(j)} \right) \cdot \frac{\left(\mathbf{c}^{(i)} - \mathbf{c}^{(j)} \right)}{| \mathbf{c}^{(i)} - \mathbf{c}^{(j)} |} \tag{52}$$

and the viscosity coefficient is

$$\nu^{(i,j)} = \frac{c_o}{2} \left(\rho_o^{(i)} \, c_s^{(i)} V_o^{(i)\,\frac{2}{3}} + \rho_o^{(j)} \, c_s^{(j)} V_o^{(j)\,\frac{2}{3}} \right) \left[1 + \frac{2 \, c_1 | v^{(i,j)} |}{(c_s^{(i)} + c_s^{(j)})} \right] \tag{53}$$

with $c_s^{(i)}$ and $V_o^{(i)}$ a soundspeed and particle reference volume. The parameters c_o and c_1 are nondimensional linear and quadratic numerical viscosity coefficients.

Similarly the viscous torque is

$$\mathbf{M}^{(i)} = \sum_{j=1}^{n} \sigma^{(i,j)} \, \mathbf{R}^{(i)T} \, \left(\mathbf{R}^{(i)} \boldsymbol{\omega}^{(i)} - \mathbf{R}^{(j)} \boldsymbol{\omega}^{(j)} \right) \, \hat{u}(1 - \zeta^{(i,j)}) \tag{54}$$

where the torsional damping coefficient is

$$\sigma^{(i,j)} = \frac{c_o}{2} \left(\rho_o^{(i)} \, c_s^{(i)} V_o^{(i)\,\frac{4}{3}} + \rho_o^{(j)} \, c_s^{(j)} V_o^{(j)\,\frac{4}{3}} \right) \tag{55}$$

Finally the thermal power flow due to artificial heat diffusion is taken to be

$$\dot{Q}^{con(i)} = \sum_{j=1}^{n} R^{(i,j)} \left(\theta^{(i)} - \theta^{(j)} \right) \hat{u}(1 - \zeta^{(i,j)}) \tag{56}$$

where the heat transfer coefficient is

$$R^{(i,j)} = \frac{k_o}{2} \left(\rho_o^{(i)} \, c_s^{(i)} c_v^{(i)} V_o^{(i)\,\frac{2}{3}} + \rho_o^{(j)} \, c_s^{(j)} c_v^{(j)} V_o^{(j)\,\frac{2}{3}} \right) \tag{57}$$

with $c_v^{(i)}$ a specific heat and k_o a numerical heat diffusion coefficient.

INTERNAL ENERGY EVOLUTION EQUATIONS

The last internal state variable to be considered is the internal energy. The introduction of internal energy states as generalized coordinates allows the thermomechanical problem of interest here to be solved using energy methods.

The internal energy evolution equations for particle i are

$$\dot{U}^{(i)} = \dot{U}^{wrk(i)} + \dot{U}^{irr(i)} - \dot{U}^{con(i)} \tag{58}$$

where the first term accounts for mechanical work, the second term accounts for the effects of irreversible entropy production, and the third term represents numerical heat diffusion.

The mechanical power flow for particle i is

$$\dot{U}^{wrk(i)} = m^{(i)} \frac{P^{(i)}}{\rho^{(i)2}} \dot{\rho}^{(i)} \tag{59}$$

The energy dissipation due to irreversible entropy production for particle i depends on the viscous forces and torques, which act on the particles, and on the dissipation in the elements

$$\dot{U}^{irr(i)} = \mathbf{f}^{(i)^T} \dot{\mathbf{c}}^{(i)} + \mathbf{M}^{(i)T} \boldsymbol{\omega}^{(i)} + \sum_{j=1}^{n} \phi^{(i,j)} \dot{Q}^{irr(j)} \tag{60}$$

where $\dot{Q}^{irr(j)}$ is a power flow due to damage evolution and plastic deformation in element j

$$\dot{Q}^{irr(j)} = \Gamma^{D(j)} \dot{D}^{(j)} + \Gamma^{d(j)} \dot{d}^{(j)} + V_o^{e(j)} \, tr \left(\mathbf{S}^{(j)T} \dot{\mathbf{E}}^{p(j)} \right) \tag{61}$$

and $\phi^{(i,j)}$ is the fraction of the dissipation in element j associated with particle i.

Finally the internal energy flows due to numerical heat diffusion are

$$\dot{U}^{con(i)} = \dot{Q}^{con(i)} \tag{62}$$

As in the case of the density evolution equations, a constraint form of the internal evolution relations is used to identify the generalized forces which appear in the Lagrange equations developed in the next section. For numerical implementation of the method, the generalized velocities are eliminated by introducing the momentum states as well as evolution relations for the density, plastic, and damage state variables. The resulting internal energy evolution relations take an explicit state space form.

LAGRANGE'S EQUATIONS

The preceding sections defined stored energy functions and nonholonomic constraints for the thermomechanical particle-element system. This section develops the final ODE model. The results of Shivarama and Fahrenthold [21] allow in the present case Lagrange's equations

to take the canonical form

$$\dot{\mathbf{p}}^{(i)} = -\mathbf{g}^{(i)} + \mathbf{q}^{c(i)}, \qquad \dot{\mathbf{c}}^{(i)} = m^{(i)-1}\,\mathbf{p}^{(i)} \tag{63}$$

$$\dot{\mathbf{h}}^{(i)} = -\mathbf{\Omega}^{(i)}\mathbf{h}^{(i)} + \mathbf{Q}^{c(i)}, \qquad \dot{\mathbf{e}}^{(i)} = \frac{1}{2}\mathbf{G}^{(i)T}\mathbf{J}^{(i)-1}\mathbf{h}^{(i)} \tag{64}$$

$$\frac{\partial V}{\partial \rho^{(i)}} = Q^{\rho(i)}, \qquad \frac{\partial V}{\partial U^{(i)}} = Q^{U(i)} \tag{65}$$

$$\frac{\partial V}{\partial d^{(j)}} = Q^{d(j)}, \qquad \frac{\partial V}{\partial D^{(j)}} = Q^{D(j)}, \qquad \frac{\partial V}{\partial \mathbf{E}^{p(j)}} = \mathbf{Q}^{p(j)} \tag{66}$$

where $\mathbf{q}^{c(i)}$, $\mathbf{Q}^{c(i)}$, $\mathbf{Q}^{\rho(i)}$, $Q^{U(i)}$, $Q^{d(i)}$, $Q^{D(i)}$, and $\mathbf{Q}^{p(j)}$ are generalized forces determined by the nonholonomic constraints. The degenerate forms of the Lagrange equations for the internal state variables are due to the fact that those variables are not associated with any generalized momenta. Introducing Lagrange multipliers $\gamma^{\rho(i)}$, $\gamma^{U(i)}$, $\gamma^{d(j)}$, $\gamma^{D(j)}$, and $\mathbf{X}^{p(j)}$ for the constraints, the generalized forces are found to be

$$\mathbf{q}^{c(i)} = -\gamma^{U(i)}\,\mathbf{f}^{(i)} + \frac{3}{8}\sum_{j\,=\,1}^{n}\left[\gamma^{\rho(i)}\rho_o^{(i)}\frac{W^{(i,j)}}{\zeta^{(i,j)5}}\hat{\mathbf{H}}^{(j)}\mathbf{r}^{(i,j)} - \gamma^{\rho(j)}\rho_o^{(j)}\frac{W^{(j,i)}}{\zeta^{(j,i)5}}\hat{\mathbf{H}}^{(i)}\mathbf{r}^{(j,i)}\right] \tag{67}$$

$$\mathbf{Q}^{c(i)} = -\gamma^{U(i)}\,\mathbf{M}^{(i)} + \frac{3}{8}\sum_{j\,=\,1}^{n}\gamma^{\rho(j)}\rho_o^{(j)}\frac{W^{(j,i)}}{\zeta^{(j,i)5}}\left(\mathbf{H}^{(i)}\hat{\mathbf{r}}^{(j,i)} \times \hat{\mathbf{r}}^{(j,i)}\right) \tag{68}$$

$$Q^{\rho(i)} = \gamma^{\rho(i)} \tag{69}$$

$$Q^{U(i)} = \gamma^{U(i)} \tag{70}$$

$$Q^{d(j)} = \gamma^{d(j)} - \sum_{i\,=\,1}^{n}\gamma^{U(i)}\,\phi^{(i,j)}\,\Gamma^{d(j)} \tag{71}$$

$$Q^{D(j)} = \gamma^{D(j)} - \sum_{i\,=\,1}^{n}\gamma^{U(i)}\,\phi^{(i,j)}\,\Gamma^{D(j)} \tag{72}$$

$$\mathbf{Q}^{p(j)} = \mathbf{X}^{p(j)} - \sum_{i\,=\,1}^{n}\gamma^{U(i)}\,\phi^{(i,j)}\,V_o^{(j)}\,\mathbf{S}^{(j)} \tag{73}$$

These results allow the unknown Lagrange multipliers to be determined in closed form, so that the final Lagrange equations are

$$\dot{\mathbf{p}}^{(i)} = -\mathbf{g}^{(i)} - \mathbf{f}^{(i)} + \mathbf{q}^{(i)} \tag{74}$$

$$\dot{\mathbf{h}}^{(i)} = -\boldsymbol{\Omega}^{(i)}\mathbf{h}^{(i)} - \mathbf{M}^{(i)} + \mathbf{Q}^{(i)} \tag{75}$$

$$\dot{\mathbf{c}}^{(i)} = m^{(i)-1}\,\mathbf{p}^{(i)} \tag{76}$$

$$\dot{\mathbf{e}}^{(i)} = \frac{1}{2}\mathbf{G}^{(i)T}\mathbf{J}^{(i)-1}\mathbf{h}^{(i)} \tag{77}$$

where the generalized forces and torques due to particle interactions are

$$\mathbf{q}^{(i)} = \frac{3}{8}\sum_{j=1}^{n}\left(V_o^{(i)}\,\frac{P^{(i)}}{\rho^{(i)2}}\,\frac{W^{(i,j)}}{\zeta^{(i,j)5}}\,\hat{\mathbf{H}}^{(j)} + V_o^{(j)}\,\frac{P^{(j)}}{\rho^{(j)2}}\,\frac{W^{(j,i)}}{\zeta^{(j,i)5}}\,\hat{\mathbf{H}}^{(i)}\right)\,\mathbf{r}^{(i,j)} \tag{78}$$

$$\mathbf{Q}^{(i)} = \frac{3}{8}\sum_{j=1}^{n} V_o^{(j)}\,\frac{P^{(j)}}{\rho^{(j)2}}\,\frac{W^{(j,i)}}{\zeta^{(j,i)5}}\left(\mathbf{H}^{(i)}\hat{\mathbf{r}}^{(j,i)} \times \hat{\mathbf{r}}^{(j,i)}\right) \tag{79}$$

Supplemented by the evolution equations for density, internal energy, shear damage, normal damage, and plastic strain, the result is an explicit first order ODE model for the thermo-mechanical particle-element system.

EXAMPLE SIMULATIONS

This section describes four example problems which illustrate application of the improved particle-element method developed in this paper. The first two examples involve one dimensional test problems with known exact solutions. The third and fourth example problems involve three dimensional simulations. The third example models a published experiment while the fourth example measures the relative computational cost of the present method in a hypervelocity impact application of current research interest.

The first example is the wall shock problem of Noh [31]. The simulations employ an ideal gas equation of state

$$P = (\gamma - 1)\,\rho\,(u - u_o), \qquad \theta = \frac{1}{c_v}\,(u - u_o) \tag{80}$$

and the parameters shown in Table 1. This problem models the collision of a fluid stream located initially in the region $0.0 < x < 0.5$ with a rigid wall located at $x = 0$. The initial conditions are $\rho = \rho_o$, $u = u_o$, and $v = -1$. Figures 1 through 4 plot the simulation results for velocity, density, pressure, and temperature at the stop time of 0.3, for a model composed of 200 particles. The numerical results show good agreement with the exact solution, although better results have been obtained using finite difference and finite element methods [31,35]. Table 2 shows convergence of the simulation results, as the particle count is increased, in terms of the velocity error norm

$$\| e \|_v = \left\{ \frac{1}{n} \sum_{i=1}^{n} \left[v^{(i)} - \hat{v}(x^{(i)}) \right]^2 \right\}^{1/2} \tag{81}$$

and the temperature error norm

$$\| e \|_\theta = \left\{ \frac{1}{n} \sum_{i=1}^{n} \left[\theta^{(i)} - \hat{\theta}(x^{(i)}) \right]^2 \right\}^{1/2} \tag{82}$$

where $\hat{v}$ and $\hat{\theta}$ denote the exact solutions for the velocity and temperature.

The second example is the bar impact problem of Kolsky [33]. The simulations employ a linear isothermal equation of state

$$P = K \left(\rho / \rho_0 - 1 \right) \tag{83}$$

and the parameters shown in Table 3. This problem models the one dimensional motion of an elastic bar of length L subjected to a step tensile pressure loading of magnitude P_{ext}, applied at the end $x = L$ at time $t = 0$. Figures 5 and 6 plot the simulation results for the bar midpoint velocity versus time, to a stop time of 0.001 seconds, for two different particle counts. The numerical results show good agreement with the exact solution. The results shown in Figure 5 are quite similar to those reported by Lu et a. [34], at the same particle count, employing an element-free Galerkin method with an explicit integration algorithm.

The third example problem models the oblique impact of a tungsten alloy (DX2HCMF) rod on a steel (SIS 2541) plate, an experiment described in references [29] and [30]. The

simulations employed a Mie-Gruneisen equation of state [32] and the material properties [30,32] listed in Table 4. The cylindrical projectile has a diameter of 0.5 cm and a length of 7.5 cm (L/D = 15). The simulation models a 1.5 km/s impact on a 0.5 cm thick plate at a sixty degree obliquity, and was run at three different particle counts. Figures 7 and 8 show the initial configuration and the simulation results at 100 microseconds after impact, while Figures 9 and 10 show sectioned views at 20 and 40 microseconds after impact. This simulation illustrates the fact that the present method retains all material fragments and models contact-impact of all intact and fragmented material. Table 5 provides simulation results, at several particle counts, for the residual rod length and residual rod velocity, showing good agreement with the corresponding experimental values (6.38 cm and 1.46 km/s). The simulation results shown here differ by less than three percent from those reported by Lee and Yoo [30] for Lagrangian finite element methods.

The fourth example problem models the oblique impact of an aluminum sphere on a reinforced carbon-carbon plate. This example does not model a specific experiment; rather it was used to measure the improved computational efficiency of the method described here, in a hypervelocity impact application of current research interest [6,36]. The projectile material, diameter (0.618 cm), and impact velocity (7 km/s) represent a typical orbital debris impact threat [4], while the target plate thickness (0.47 cm) is characteristic of reinforced carbon-carbon components of the Space Shuttle thermal protection system [6]. Experimental studies of the mechanical properties of reinforced carbon-carbon are in progress; the material properties used in the simulations are listed in Table 6. A total of six simulations were performed, at three different particle counts, to measure the the computational cost of density calculations made using interpolations kernels, as compared to the nonholonomic formulation developed in the present paper. Each simulation was run to a stop time of ten microseconds, sufficient to perforate the target and include the shock loading and fragmentation processes of central interest in hypervelocity impact applications. Figures 10 through 15 show representative simulation results. Table 7 lists the wall clock times and processor

counts for the simulations, run on a Linux cluster composed of dual processor (3 GHz) nodes. The results show the relatively high computational cost of kernel based density calculations, in the present hybrid particle finite element context. Wall clock times are increased for all three problem sizes and associated processor counts, by an average factor of one third. This result is not surprising, since the finite element related portion of the computation is relatively inexpensive [22], while most of the particle related computations are performed in two sequential routines: one loops over all neighbor particles to determine the density, the second loops again over all neighbor particles to compute the particle interaction forces. The effect of introducing the nonholonomic density calculation developed here is to eliminate the first of these two routines. Considering the very high computational costs of three dimensional shock physics problems, the measured reduction in wall clock time is significant.

CONCLUSION

The present paper has formulated a new kernel free particle-finite element method and demonstrated its application in three dimensional hypervelocity impact simulations. Unlike alternative methods, the formulation is derived without reference to any weighting or interpolation functions for either the density or the rate of dilatation. The improved method introduces a new formulation of the thermomechanical Lagrange equations, one which employs internal energies as generalized coordinates. This avoids the requirement to perform certain Legendre transforms, in order to express the dependence of the pressure and temperature on entropy, and hence allows for the use of equations of state in standard form. As compared to the previous formulation, the revised method is both simplified and computationally more efficient. Applications work in progress is focused on the simulation of orbital debris impact effects on spacecraft thermal protection materials [6].

ACKNOWLEDGEMENTS

This work was supported by NASA Johnson Space Center (NAG9-1244), the National Science Foundation (CMS99-12475), and the State of Texas Advanced Research Program

(003658-0709-1999). Computer time support was provided by the Texas Advanced Computing Center at the University of Texas at Austin and the Arctic Region Supercomputing Center at the University of Alaska Fairbanks.

Table 1. Simulation parameters for the wall shock problem

Ratio of specific heats (γ)	$\frac{5}{3}$
Specific heat (c_v)	1.0
Reference internal energy (e_o)	1.0
Reference density (ρ_o)	1.0
Reference temperature (θ_o)	1.0
Numerical viscosity coefficient (c_o)	1.0
Numerical viscosity coefficient (c_1)	0.0
Numerical conduction coefficient (k_o)	0.1

Table 2. Error norms for the wall shock problem

Number of particles	Velocity error norm	Temperature error norm
100	0.17116	0.08594
200	0.12141	0.06075
400	0.08635	0.04325
800	0.06081	0.03032

Table 3. Simulation parameters for the bar impact problem

Length of the bar (L, in)	100
Bulk modulus (K, psi)	30.0×10^6
Applied end loading (P_{ext}, psi)	50.0×10^3
Reference density (ρ_o, pci)	0.73×10^{-3}
Numerical viscosity coefficient (c_o)	1.0
Numerical viscosity coefficient (c_1)	0.0

Table 4. Material properties used in the long rod impact simulations

Material property	Projectile	Target
Reference density (g/cc)	17.6	7.87
Shear modulus (Mbar)	1.45	0.801
Reference yield stress (Mbar)	0.0075	0.0105
Strain hardening coefficient	1.15	0.177
Strain hardening exponent	0.49	0.12
Thermal softening coefficient	1.0	1.0
Melt temperature (deg K)	1,700	1,723
Specific heat (Mbar-cm^3 per g-deg K)	0.143e-5	0.448e-5
Plastic failure strain	1.0	1.0

Table 5. Simulation results for the long rod impact problem

Number of particles	Residual length (cm)	Residual velocity (km/s)
35,992	6.08	1.42
92,498	6.47	1.42
187,826	6.59	1.42

Table 6. Material properties used in the plate impact simulations

Material property	Projectile	Target
Reference density (g/cc)	2.70	1.58
Shear modulus (Mbar)	0.271	0.0718
Reference yield stress (Mbar)	0.0029	0.000771
Strain hardening coefficient	125.0	2.0
Strain hardening exponent	0.10	1.0
Thermal softening coefficient	0.567	-1.0
Melt temperature (deg K)	1,220	3,840
Specific heat (Mbar-cm^3 per g-deg K)	0.884e-5	0.712e-5
Plastic failure strain	1.0	0.5

Table 7. Relative computational costs for the plate impact simulations

Particles	Density calculation	Processors	Wall clock hours	Relative cost
21,334	nonholonomic	4	1.2611	1.000
21,334	kernel	4	1.7581	1.394
63,253	nonholonomic	6	4.5047	1.000
63,253	kernel	6	5.8078	1.289
140,070	nonholonomic	8	28.8933	1.000
140,070	kernel	8	38.1411	1.320

REFERENCES

[1] Anderson CE, ed. Proceedings of the 2003 Hypervelocity Impact Symposium. *International Journal of Impact Engineering*, 2003; **29**: No. 1-10.

[2] Gisler G, Weaver R, Gittings M, and Mader C. Two and three dimensional asteriod ocean impact simulations. *International Journal of Impact Engineering*, 2003; **29**: 283-292.

[3] Knudson MD, Hall CA, Lemke R, Deeney C, and Asay JR. High Velocity Flyer Plate Launch Capability on the Sandia Z Accelerator. *International Journal of Impact Engineering*, 2003; **29**: 377-384.

[4] Hayhurst CJ, Livingstone IHG, Clegg, RA, Destefanis R, Faraud M. Ballistic limit evaluation of advanced shielding using numerical simulations. *International Journal of Impact Engineering*, 2001; **26**: 309-320.

[5] Yatteau JD, Recht GW, Edquits KT. Transverse loading and response of long rod penetrators during high velocity plate perforation. *International Journal of Impact Engineering*, 1999; **23**: 967-980.

[6] Christiansen EL and Friesen L. Penetration equations for thermal protection materials. *International Journal of Impact Engineering*, 1997; **20**: 153-164.

[7] Christiansen EL and Kerr JH. Projectile shape effects on shielding performance at 7 km/s and 11 km/s. *International Journal of Impact Engineering*, 1997; **20**: 165-172.

[8] Benson DJ. Computational methods in Lagrangian and Eulerian hydrocodes. *Computer Methods in Applied Mechanics and Engineering*, 1992; **99**: 235-394.

[9] McGlaun JM, Thompson SL, Elrick MG. CTH: A three dimensional shock wave physics code. *International Journal of Impact Engineering*, 1990; **10**: 351-360.

[10] Hertel ES. A Comparison of the CTH Hydrodynamics Code With Experimental Data, 1992, SAND92-1879, Sandia National Laboratories.

[11] Hallquist JO. Theoretical Manual for DYNA3D, 1983, Lawrence Livermore National Laboratory, Livermore, California.

[12] Carroll DE, Hertel ES, Trucano TG. Simulation of armor penetration by tungsten rods: ALEGRA validation report, 1997, SAND97-2765, Sandia National Laboratories.

[13] Wallin BK, Tong C, Nichols AL, Chow ET. Large multiphysics simulations in ALE3D. Presented at the Tenth SIAM Conference on Parallel Processing for Scientific Computing, Portsmouth, Virginia, March 12-14, 2001.

[14] Stellingwerf RF, Wingate CA. Impact modeling with smooth particle hydrodynamics. *International Journal of Impact Engineering*, 1993; **14**: 707-718.

[15] Shapiro PR, Martel H, Villumsen JV, Owen JM. Adaptive smoothed particle hydrodynamics with application to cosmology: methodology. *The Astrophysical Journal Supplement Series*, 1996; **103**: 269-330.

[16] Owen JM, Villumsen JV, Shapiro PR, Martel H. Adaptive smoothed particle hydrodynamics with application to cosmology: methodology II. *The Astrophysical Journal Supplement Series*, 1998; **116**: 155-209.

[17] Belytschko T, Krongauz Y, Organ D, Fleming M, Krysl P. Meshless methods: an overview and recent developments. *Computer Methods in Applied Mechanics and Engineering*, 1996; **139**: 3-47.

[18] Fahrenthold EP. Numerical simulation of impact on hypervelocity shielding. Proceedings of the Hypervelocity Shielding Workshop, 1998, Galveston, Texas, pp. 47-50.

[19] Fahrenthold EP, Horban BA. An improved hybrid particle-element method for hypervelocity impact simulation. *International Journal of Impact Engineering*, 2001; **26**: 169-178.

[20] Johnson GR, and Stryk RA. Conversion of 3D distorted elements into meshless particles during dynamic deformation. *International Journal of Impact Engineering*, 2003; **28**: 947-966.

[21] Shivarama R and Fahrenthold EP. An ellipsoidal particle-finite element method for hypervelocity impact simulation. *International Journal for Numerical Methods in Engineering*, 2004; **59**: 737-753.

[22] Fahrenthold EP, Shivarama R. Extension and validation of a hybrid particle-element method for hypervelocity impact simulation. *International Journal of Impact Engineering*, 2003; **29**: 237-246.

[23] Haim Baruh. Analytical Dynamics, 1999, McGraw Hill, New York.

[24] Rapaport DC. Molecular dynamics simulation using quaternions. *Journal of Computational Physics*, 1985; **41**: 306-314.

[25] Lubliner J. Plasticity theory, 1990, Macmillan, New York

[26] Lyon SP, Johnson JD, editors. SESAME: The Los Alamos National Laboratory Equation of State Database, LA-UR-92-3407, Los Alamos National Laboratory, Los Alamos, New Mexico.

[27] Fahrenthold EP, Horban BA. Thermodynamics of continuum damage and fragmentation models for hypervelocity impact. *International Journal of Impact Engineering*, 1997; **20**: 241-252.

[28] Silling SA. CTH Reference Manual: Johnson-Holmquist Ceramic Model, 1992, SAND92-0576, Sandia National Laboratories.

[29] Liden E, Ottosson J, and Holmberg L. WHA rods penetrating stationary and moving oblique steel plates. Proceedings of the 16th International Symposium on Ballistics, 1996, pp. 711-719.

[30] Lee M, Yoo YH. Assessment of a new dynamic FE-Code: application to the impact of a yawed-rod onto nonstationary oblique plate. *International Journal of Impact Engineering*, 2003; **29**: 425-436.

[31] Noh, W.F. Errors for calculation of strong shocks using an artificial viscosity and an artificial heat flux. *Journal of Computational Physics*, 1978; **72**: 78-120.

[32] Steinberg DJ. Equation of State and Strength Properties of Selected Materials, 1996, Lawrence Livermore National Laboratory, UCRL-MA-106439.

[33] Kolsky H. Stress waves in solids, 1963, Dover, New York

[34] Lu, YY, Belytschko, T, and Tabbara, M.. Element-free Galerkin method for wave propagation and dynamic fracture. *Computer Methods in Applied Mechanics and Engineering*, 1995; **126**: 131-153.

[35] Fahrenthold, EP, and Koo, JC. Discrete Hamilton's equations for viscous compressible fluid dynamics. *Computer Methods in Applied Mechanics and Engineering*, 1999; **178**: 1-22.

[36] Fahrenthold, EP, and Park, YK. Simulation of foam impact effects on the space shuttle thermal protection system. *AIAA Journal of Spacecraft and Rockets*, in press.

LIST OF FIGURES

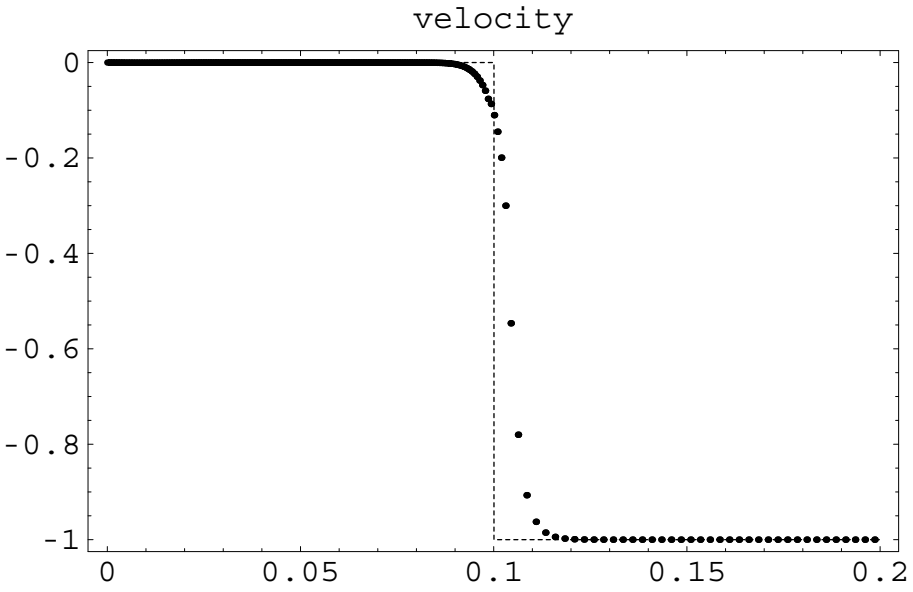

Figure 1: Wall shock problem, velocity versus position at t = 0.3.

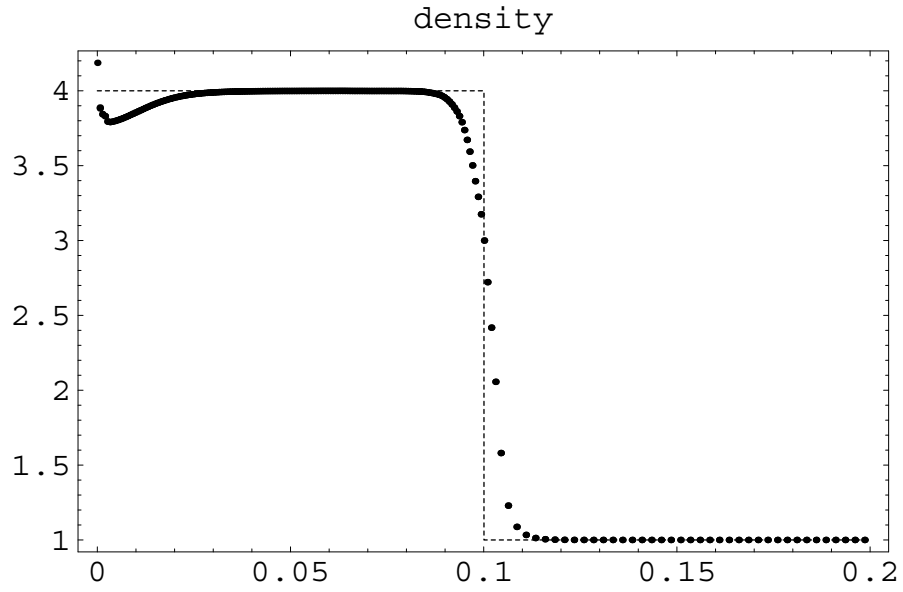

Figure 2: Wall shock problem, density versus position at t = 0.3.

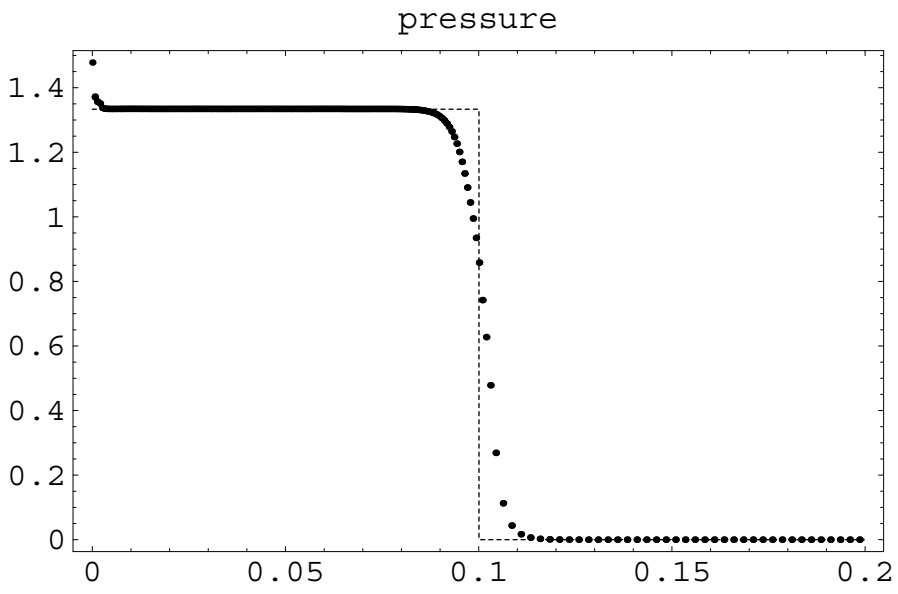

Figure 3: Wall shock problem, pressure versus position at t = 0.3.

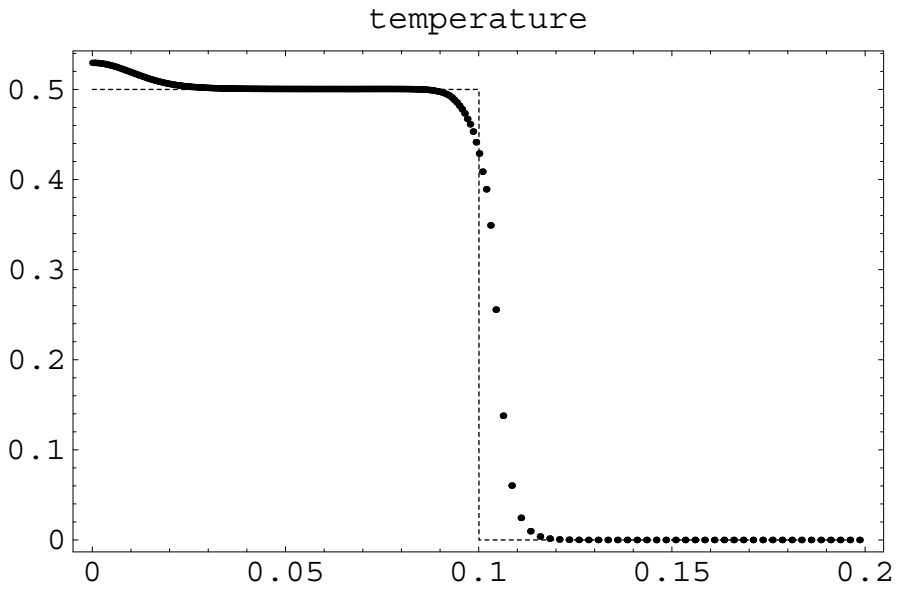

Figure 4: Wall shock problem, temperature versus position at t = 0.3.

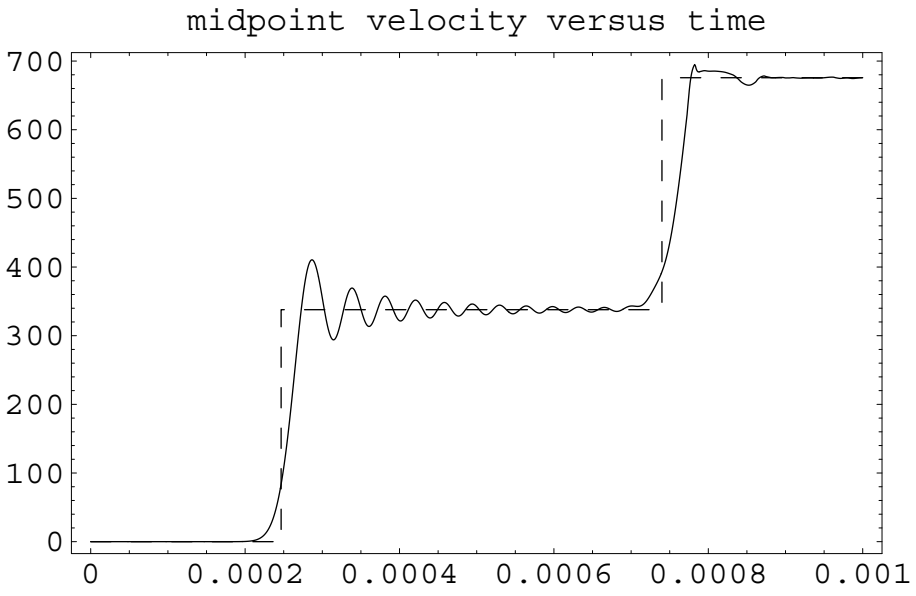

Figure 5: Bar impact problem, midpoint velocity versus time for 51 particles.

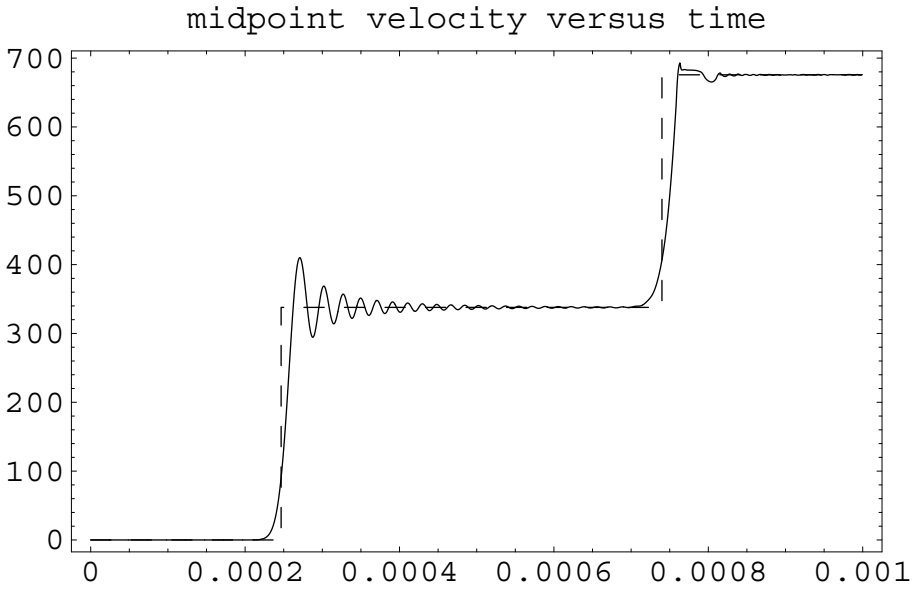

Figure 6: Bar impact problem, midpoint velocity versus time for 101 particles.

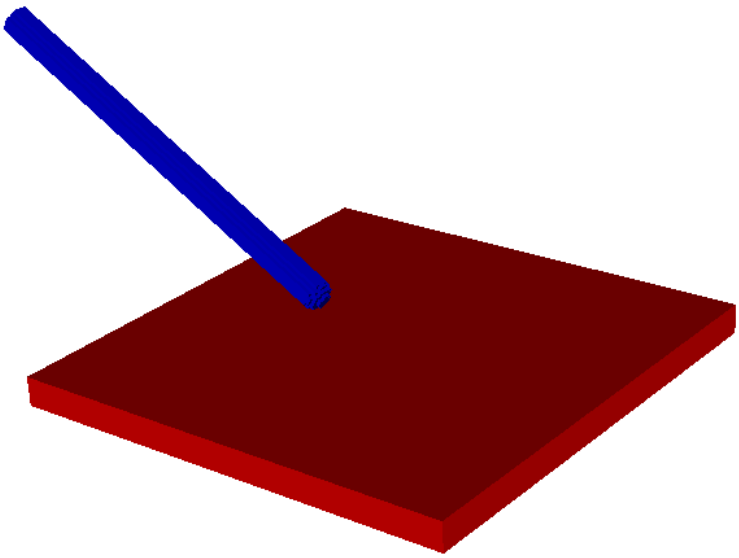

Figure 7: Long rod impact problem, element plot of the initial configuration.

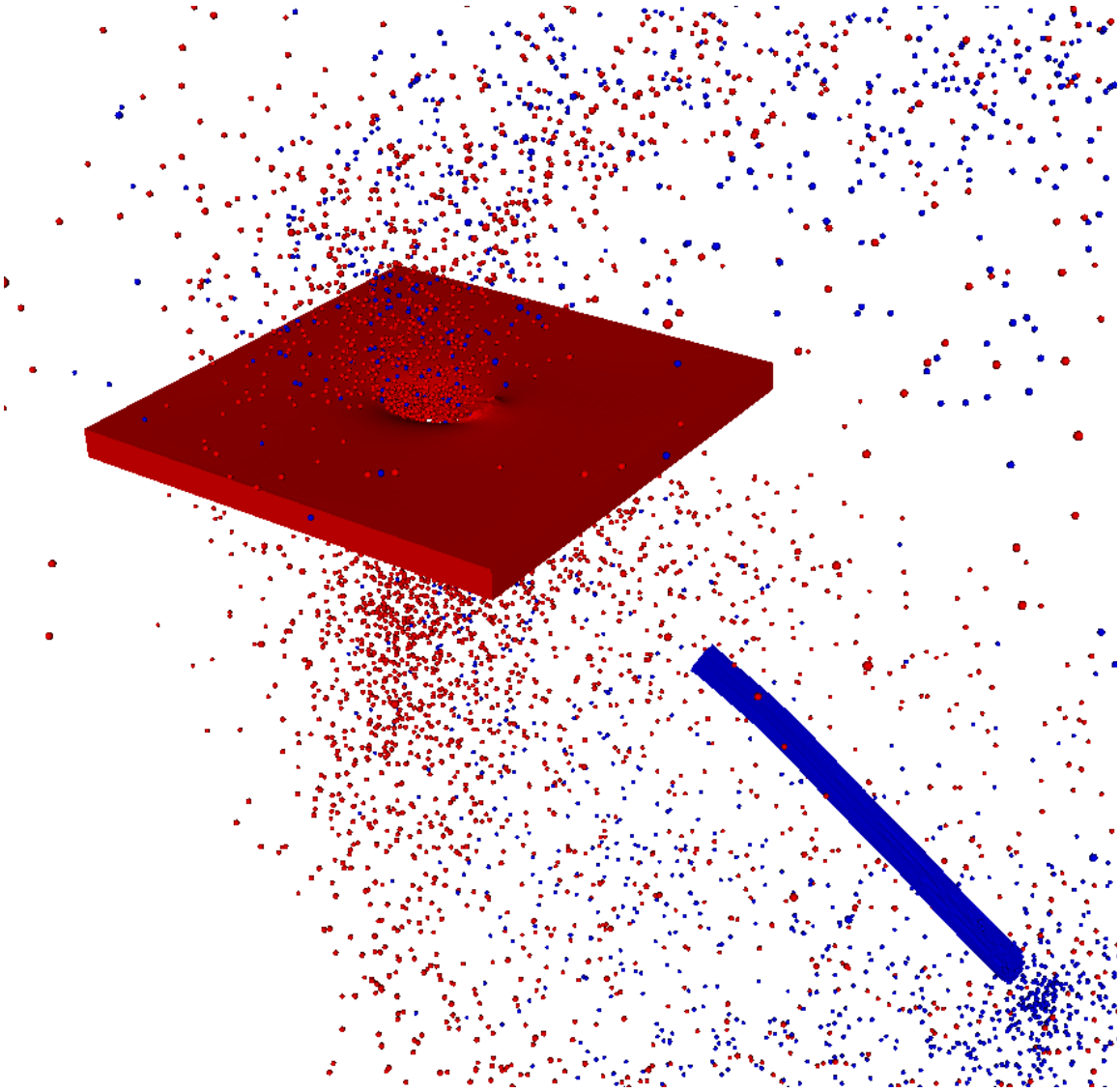

Figure 8: Long rod impact problem, particle-element plot at 100 microseconds after impact.

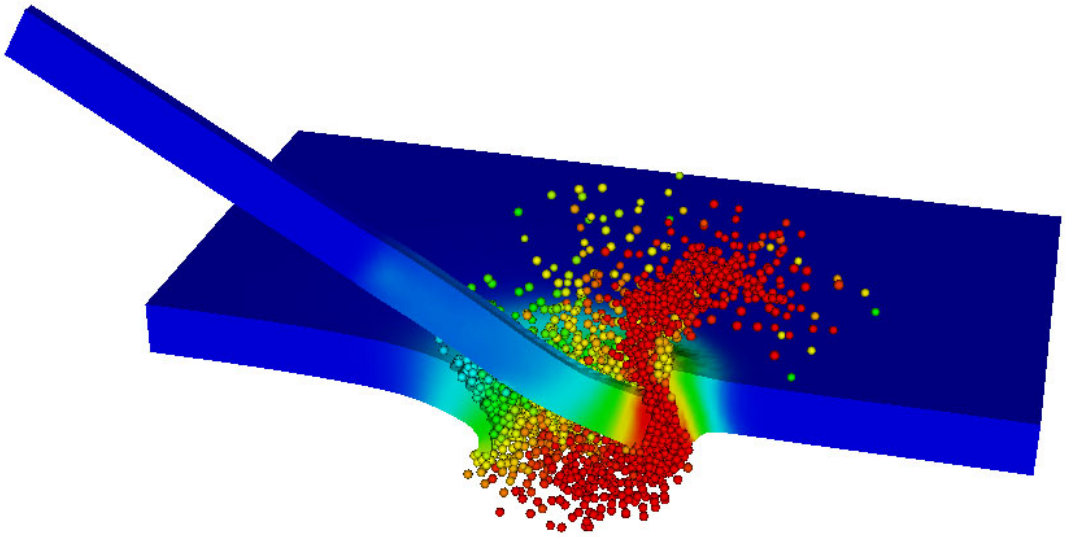

Figure 9: Long rod impact problem, sectioned particle-element plot at 20 microseconds after impact, color on temperature.

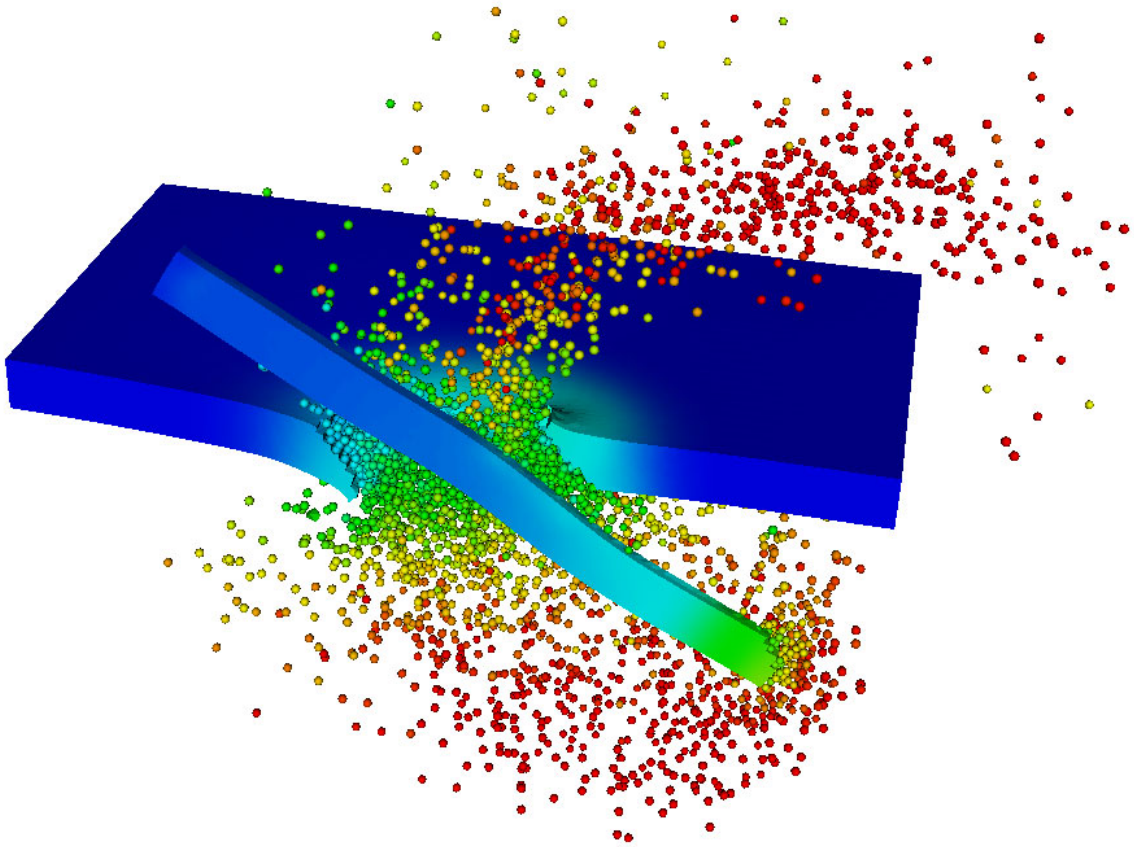

Figure 10: Long rod impact problem, sectioned particle-element plot at 40 microseconds after impact, color on temperature.

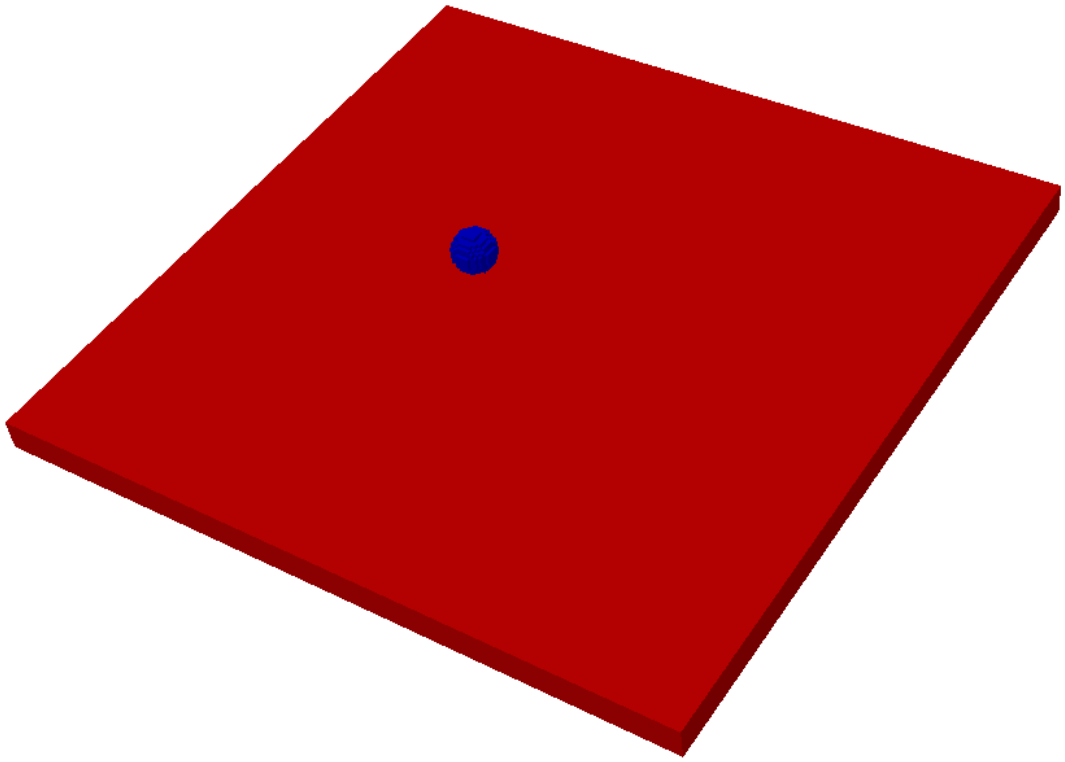

Figure 11: Plate impact problem, element plot of the initial configuration.

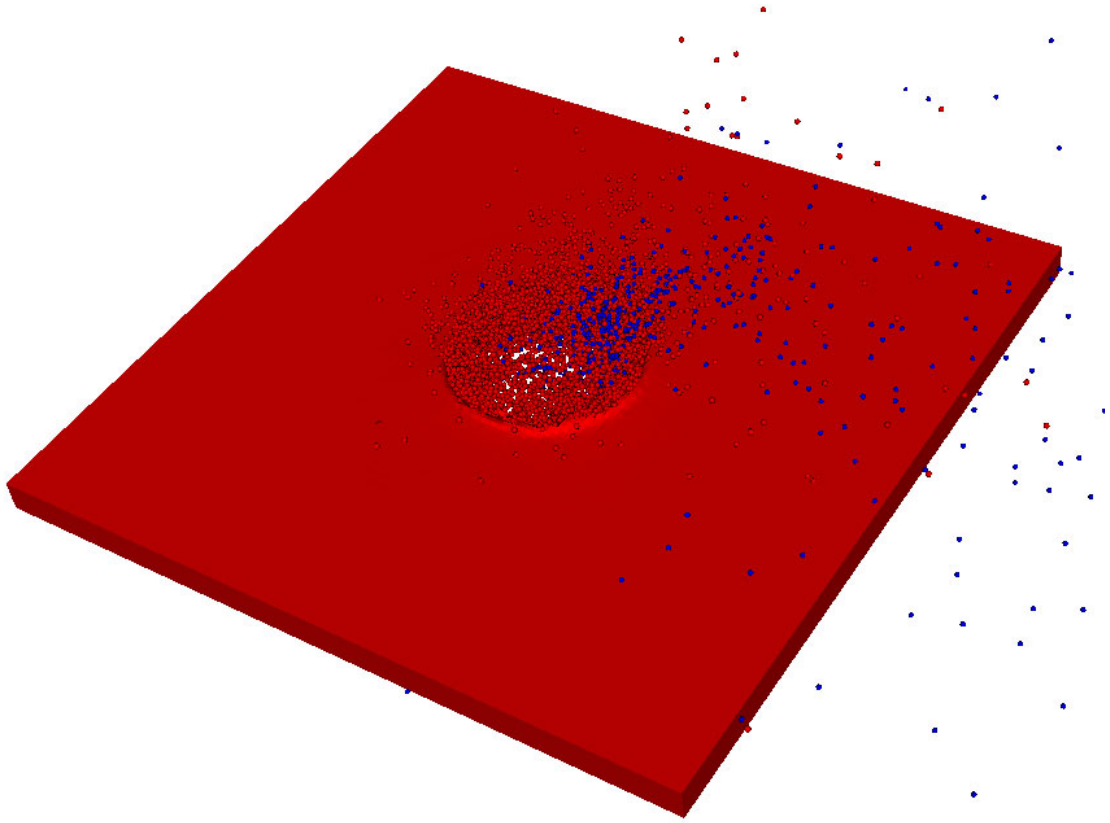

Figure 12: Plate impact problem, particle-element plot at 10 microseconds after impact.

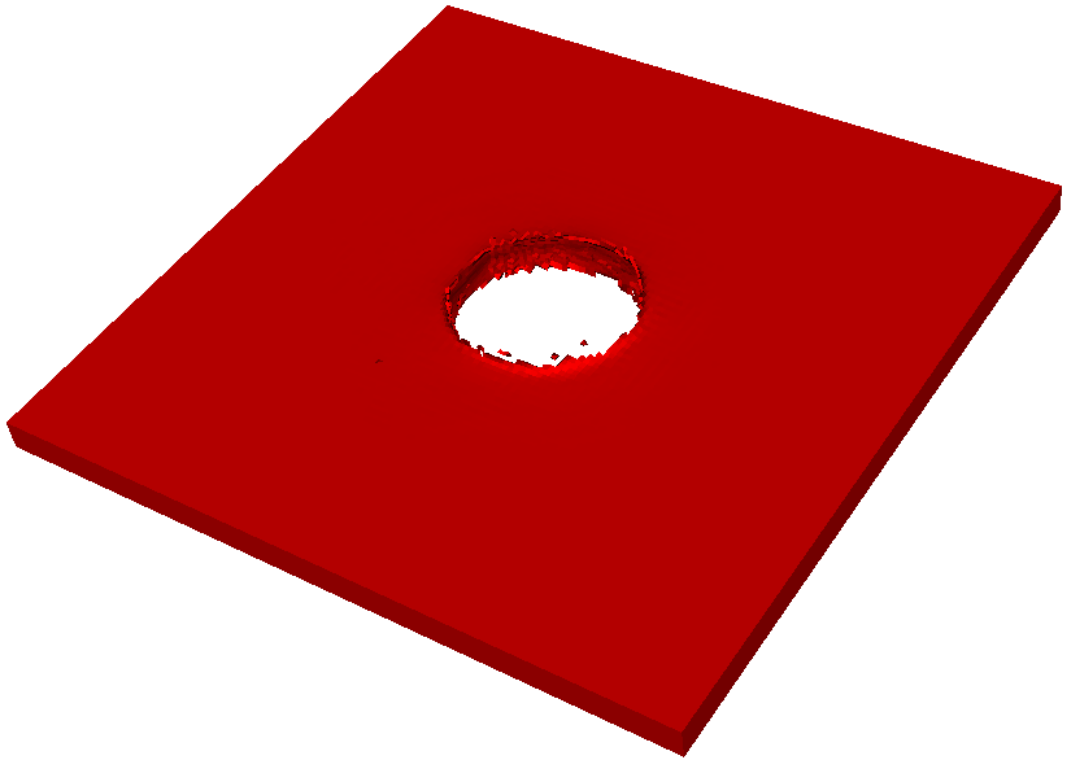

Figure 13: Plate impact problem, element plot at 10 microseconds after impact.

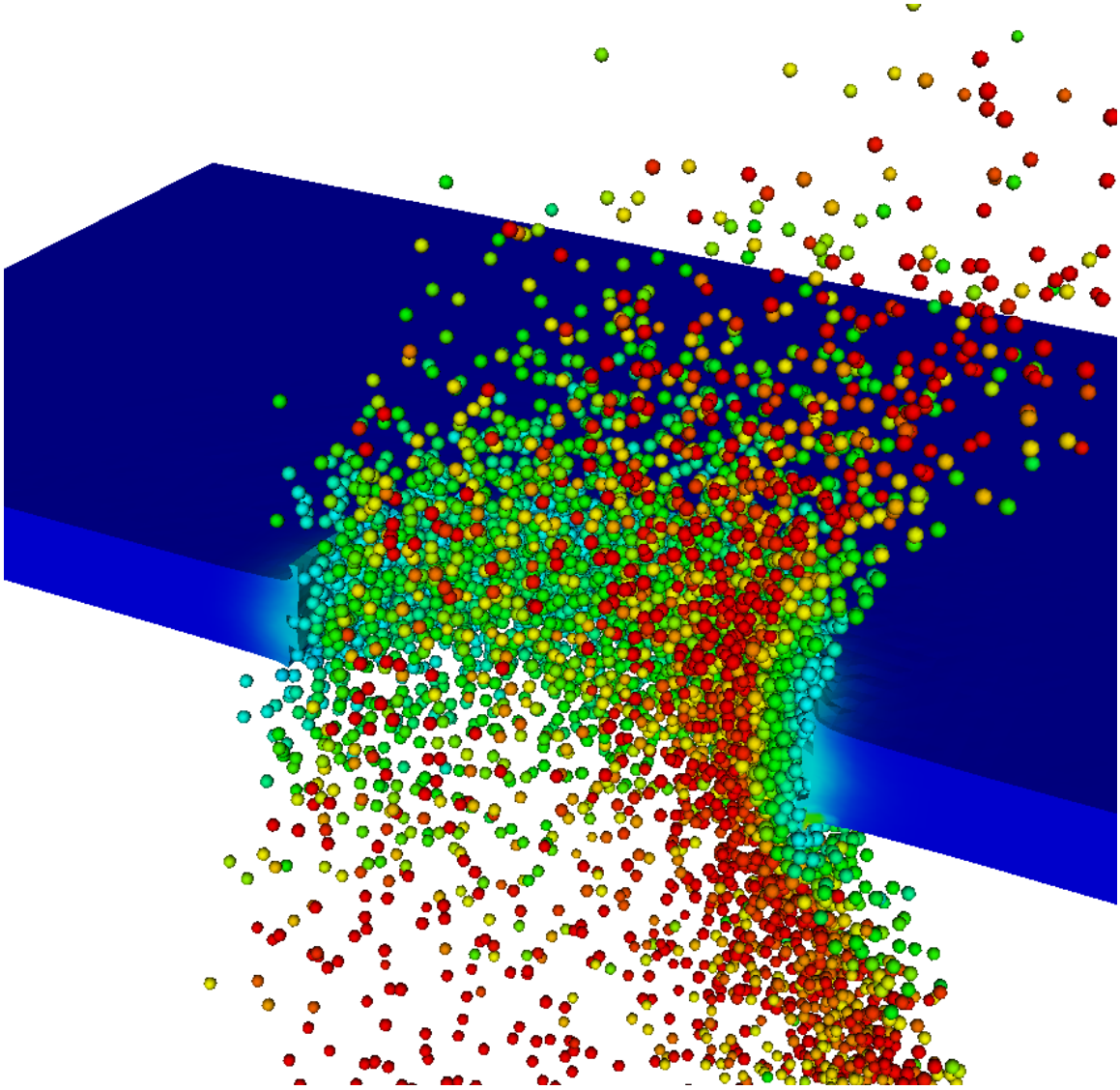

Figure 14: Plate impact problem, sectioned particle-element plot at 10 microseconds after impact, color on temperature.

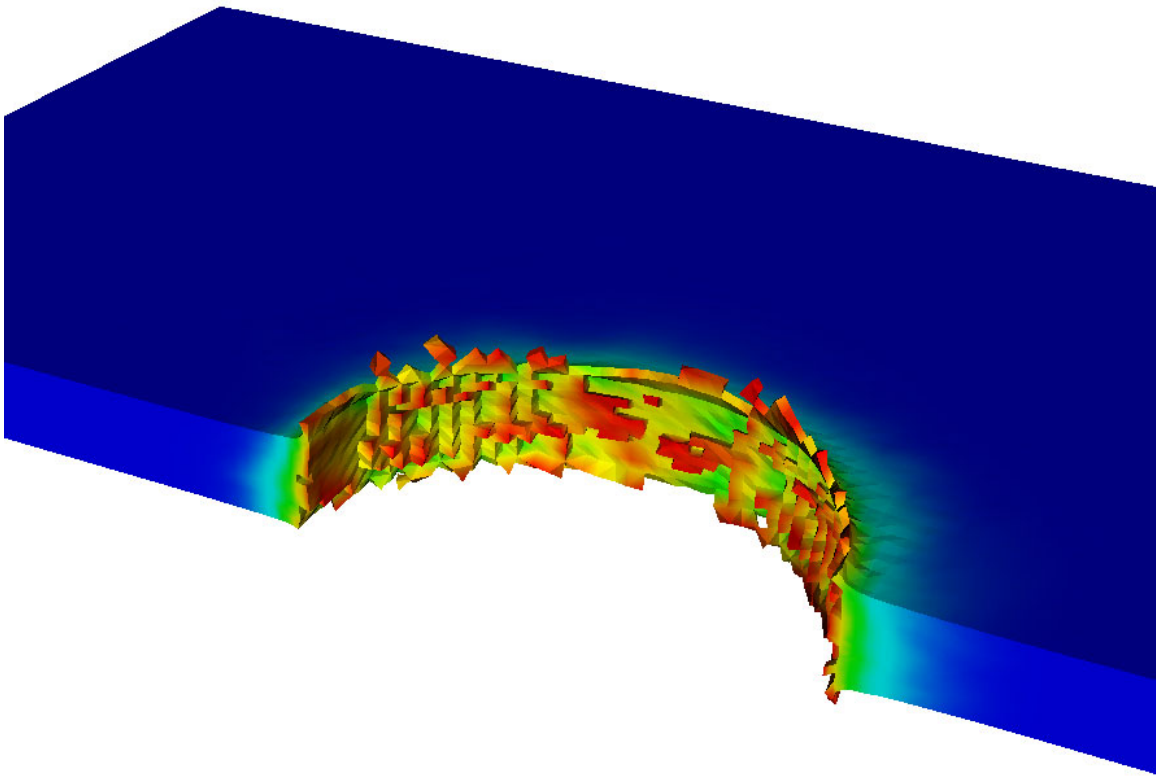

Figure 15: Plate impact problem, sectioned element plot at 10 microseconds after impact, color on effective plastic strain.

CHAPTER 5

SIMULATION OF HYPERVELOCITY IMPACT ON ALUMINUM-NEXTEL-KEVLAR ORBITAL DEBRIS SHIELDS

Eric P. Fahrenthold[1] **and Young-Keun Park**[2]

Department of Mechanical Engineering, 1 University Station C2200
University of Texas, Austin, TX 78712, USA

[1]Professor, corresponding author, phone: (512) 471-3064, email: epfahren@mail.utexas.edu
[2]Graduate student

SIMULATION OF HYPERVELOCITY IMPACT ON ALUMINUM-NEXTEL-KEVLAR ORBITAL DEBRIS SHIELDS

Eric P. Fahrenthold[3] and Young-Keun Park[4]

Department of Mechanical Engineering, 1 University Station C2200
University of Texas, Austin, TX 78712, USA

KEYWORDS: particle methods, finite element methods, impact simulation

INTRODUCTION

Advanced orbital debris shield designs often incorporate a multi-plate geometry and are fabricated of composite materials. An example is the aluminum-Nextel-Kevlar shields developed by NASA [1] for application on the International Space Station (ISS). Simulation of hypervelocity impact effects on these shielding designs is difficult, due both to their geometry and their material composition. Since multi-plate shields distribute the allocated shielding mass over more than one bumper, they reduce the minimum bumper thickness and in general increase the computational cost of the simulation. The extensive use of composite materials in advanced shielding designs complicates the simulation problem for two basic reasons: (a) the requirement to consider nonhomogeneous or anisotropic media increases the number of internal state variables which must be evolved in any numerical simulation, and (b) the thermomechanical response of such materials, generally more complex than that of aluminum or other metals, may be only partially described by the existing material property data base. In spite of these complications, simulation of the hypervelocity impact response of multi-plate metal-composite debris shields is of strong engineering interest, due to their proven effectiveness as components of spacecraft protection systems [2]. The present work describes numerical implementation of a rate dependent material model for Kevlar [3,4], and the conduct of several three dimensional simulations, performed to investigate the hyper-

[3]Professor, corresponding author, phone: (512) 471-3064, email: epfahren@mail.utexas.edu
[4]Graduate research assistant

velocity impact response of aluminum-Nextel-Kevlar debris shields like those deployed on the ISS. The simulations employed a hybrid-particle finite element method and a parallel computer code specifically developed to address the orbital debris shielding design problem. Simulation work appears to conservatively estimate the protection afforded by multi-layered aluminum-Nextel-Kevlar shielding.

COMPOSITE DEBRIS SHIELDING

Kevlar aramid fiber, introduced by the Du Pont Company in 1972, has been used in a variety of impact protection applications. The woven cloth Nextel (manufactured by 3M corporation) is made from alumina, a ceramic shown to provide effective impact protection when applied as a component of composite armor systems. These materials are used in the design of the multiplate orbital debris shielding deployed on some modules of the ISS. The latter shielding consists of three material layers, arranged in the sequence: aluminum, Nextel, Kevlar. The outer aluminum bumper is located approximately eleven centimeters from the pressurized module, a multilayer stack of Nextel cloth is located approximately halfway between the aluminum bumper and the pressure wall, and a multilayer stack of Kevlar cloth is located directly behind the Nextel. Nextel is manufactured in various grades. A number of different grades of Kevlar are also manufactured, with Kevlar 29 (all purpose yarn), Kevlar 49 (high modulus yarn), and Kevlar 129 (high tenacity yarn) used in composite armor applications. Tables 1 and 2 list mechanical properties of these three grades of Kevlar and compare some important material properties of high performance Nextel and Kevlar fibers.

IMPACT SIMULATIONS

Experimental work has demonstrated that aluminum-Nextel-Kevlar shields perform much better than weight equivalent Whipple shield designs. Hence the development of a validated computer aided design tool for use in future composite shielding design studies is of considerable interest. Fahrenthold and Shivarama [9] described some initial work on the use of a

hybrid particle-finite element method for composite shield impact simulations. The latter work used a rather coarse three dimensional model of less the 0.5 million particles, and a simulation time of less than 55 microseconds. The simulations discussed here involved an order of magnitude increase in particle count and a three-fold increase in simulation time. Related work using SPH and finite element methods has been reported by Hiermaier et al. [10] and Palmieri [11], although the latter efforts have focused on the use of Kevlar-epoxy plates [12], in lieu of the cloth Kevlar material modeled here. Three of the four simulations described in the present chapter modeled an experiment performed by Grosch [13], test number SwRI 7139-24, in which a 1.07 gram inhibited shaped charge (ISC) projectile struck a two-thirds scale model composite orbital debris shield similar to that deployed on the ISS. Parameters of the experiment are detailed in Table 3. The impact velocity is 11 kilometers per second, and the impact obliquity is 45 degrees. The first simulation reported here modeled the ISC projectile used in the experiment. A second simulation was performed using a spherical projectile with the same mass as the experimental (ISC) projectile, in order to investigate the effect of projectile shape [14] on the simulation results. A concern in the conduct of any hypervelocity impact simulation is the use of an appropriate equation of state. However there is no validated Mie-Gruneisen or tabular equation of state data for either Nextel cloth or Kevlar cloth. The aforementioned work of Hiermaier et al. [10] developed an equation of state and an orthotropic elastic model for Kevlar-epoxy, as well as a compaction equation of state for Nextel. The Kevlar layer modeled here does not include epoxy, and a compaction model for Nextel may not be appropriate for use in the present application. Hence the first and second simulations presented here used a linear equation of state and the material properties listed in Table 4. The first simulation represented the ISC projectile as a hollow aluminum cylinder, with dimensions estimated from the experimental radiographs. The exact mass and geometry of ISC projectiles is somewhat uncertain. Both simulations employed approximately 6 million particles, and required approximately 252 wall clock hours to complete, in parallel execution on 16 processors of an IBM Regatta.

The enclosed Figures 1 and 2 show an element plot of the first case at the simulation start time, and a particle plot of the simulation results at 100 microseconds after impact. Figures 3 and 4 show element plots of the damage at each level of the multi-plate structure, again at 100 microseconds. The simulation results underestimate the composite shield performance, since the experimental results showed a bulged but not perforated wall plate. A comparison of the first and second simulations, involving mass equivalent spherical and ISC projectiles, is provided by the wall plate plot of Figure 5, showing the results of the spherical projectile impact simulation, at 150 microseconds after impact. The results suggest that projectile geometry effects are significant even at the upper end of the orbital debris velocity regime.

COMPOSITE MATERIAL MODELS

The preceding simulation results underestimate the protection afforded by composite shielding materials. To investigate the effects of changes in the composite material models on the predicted shielding performance, both the Nextel and Kevlar equations of state were modified, and a rate-dependent strength model was introduced for the Kevlar. Two additional simulations were then conducted using the modified composite material models. The modified equations of state for Nextel and Kevlar used a Mie-Gruneisen functional form and the estimated material properties listed in the enclosed table, with the Gruneisen gamma for Nextel and Kevlar approximated using the formula of Anderson [17]

$$\Gamma \;=\; \beta\kappa/\rho C \tag{1}$$

where β is the thermal expansion coefficient, κ is the bulk modulus, C is the specific heat, and ρ is the density. The engineering application discussed here involves very high strain rate loading, hence any variation of material properties with strain rate is of considerable interest. Two recent papers [3,4] describe a significant strain rate dependence in the measured mechanical response of Kevlar 49, as summarized in Table 5, for experiments conducted over a large strain rate regime. The parameters listed refer to the (apparent) Young's modulus, the maximum engineering stress, and the engineering strain at maximum engineering stress,

as measured under uniaxial loading conditions. There is no data showing a similar strain rate dependence for Nextel. For use in later impact simulation work, the maximum stress versus strain rate data were fit to the function

$$\frac{\sigma}{\sigma_0} = g(\dot{\varepsilon}) \tag{2}$$

where

$$g(\dot{\varepsilon}) = 1 \qquad \dot{\varepsilon} \leq \dot{\varepsilon}_0 \tag{3}$$

and

$$g(\dot{\varepsilon}) = 1 + a\left[ln\frac{\dot{\varepsilon}}{\dot{\varepsilon}_0}\right]^m \qquad \dot{\varepsilon} > \dot{\varepsilon}_0 \tag{4}$$

As indicated in Figure 6, for Kevlar 49

$$a = 0.0064, \quad m = 1.4 \tag{5}$$

where the reference values of stress and strain rate are

$$\sigma_0 = 2340\ MPa, \quad \dot{\varepsilon}_0 = 0.0001\ s^{-1} \tag{6}$$

To investigate the effects of rate dependence on predicted Kevlar impact response, the plasticity model of Fahrenthold and Horbon [5] was modified, as described in the equations which follow, and used in the two simulations discussed next. Note that the plasticity model outlined here incorporates large strain kinematics and an isochoric plastic deformation constraint. The nonassociated flow rule for the plastic strain rate ($\dot{\mathbf{E}}^p$) is

$$\dot{\mathbf{E}}^p = \dot{\lambda}\left(\mathbf{C}^p\mathbf{W} + \mathbf{W}\mathbf{C}^p\right) \tag{7}$$

where $\dot{\lambda}$ is a scalar multiplier and

$$\mathbf{W} = \mathbf{C}^p\mathbf{S}^{eff} + \mathbf{S}^{eff}\mathbf{C}^p - \frac{1}{3}tr\left[\mathbf{C}^p\mathbf{S}^{eff} + \mathbf{S}^{eff}\mathbf{C}^p\right]\mathbf{I} \tag{8}$$

with the effective stress tensor and plastic Cauchy-Green strain tensor defined by

$$\mathbf{S}^{eff} = \frac{(1-d)2\mu_0\mathbf{E}^e}{g(\dot{\varepsilon})}, \quad \mathbf{C}^p = \mathbf{I} + 2\mathbf{E}^p \tag{9}$$

where $\dot{\varepsilon}$ is the effective strain rate, $\mathbf{E}^e$ is the elastic deviatoric strain, d is the deviatoric damage, and μ_0 is the shear modulus. The yield condition is

$$f = \tau - Y, \quad \tau = \left\{ \frac{1}{2} tr \left[\mathbf{S}^{eff^T} \mathbf{S}^{eff} \right] \right\}^{1/2} \tag{10}$$

where τ is the second invariant of the effective stress. The yield stress Y is

$$Y = \frac{1}{2} (1-d)\, Y_0 \, \{1 - \gamma\theta\} \tag{11}$$

where Y_0 is the reference yield stress, γ is a thermal softening modulus, and θ is the homologous temperature. The plastic strain increment at each time step is determined using a one step iteration procedure with

$$\Delta\lambda = \frac{(\tau - Y)\, \Lambda\, (\tau - Y)}{(1-d)\, 2\mu_0\, \omega\, g(\dot{\varepsilon})} \tag{12}$$

where Λ denotes the unit step function and

$$\omega = \left\{ \frac{1}{2} tr \left[\mathbf{W}^T \mathbf{W} \right] \right\}^{1/2} \tag{13}$$

The preceding modified material models were used in two additional three dimensional simulations of hypervelocity impact effects on aluminum-Nextel-Kevlar shielding. The first simulated a published light gas gun experiment [1], while the second again considered the ISC experiment discussed in the last section. The light gas gun experiment was JSC test B536, and involved the oblique (15 degree) impact of a 1.0 gram aluminum sphere on a full scale aluminum-Nextel-Kevlar shield, at a velocity of 6.86 km/s. Parameters of the experiment are listed in Table 5. The simulation employed 1.18 million particles and required 63.2 wall clock hours to complete on 16 processors of an IBM Regatta. The simulation results (Figures 7 and 8) indicate at 150 microseconds a slightly deformed but not perforated wall

plate. The experiment showed a "slight dish," indicating that the simulation results provide an accurate estimate of the wall plate damage. Since simulation of this light gas gun test showed good agreement with the corresponding experiment, simulation of the ISC projectile test SwRI 7139-24 was repeated with a relatively high resolution model and the modified material models discussed in this section. The simulation employed 15.6 million particles and required 305 wall clock hours to complete on 512 processors of an SGI Origin. The simulation results (Figures 9 and 10) indicate at 75 microseconds a perforated wall plate. The effect of introducing nonlinear equations of state for the composites and a rate dependent Kevlar model appears in this case to be rather small, with the simulation again overestimating the wall plate damage. The results reported here suggest that the hybrid particle-element method used in the simulations is numerically robust and captures important basic features of multi-plate impact experiments. For example, the intermediate composite shields are perforated, not fluidized, by the debris cloud impact. However the results also suggest that modeling improvements are needed, in order to better represent the available experimental impact data. The present study suggests possibilities for future work in both the modeling and experimental areas. First, the modeling of damage induced anisotropy, commonly encountered for example in ceramic media, may be investigated to determine its effect on predicted shield performance. Second, impact experiments using a simpler target geometry might be conducted, with a primary goal of materials characterization in mind.

CONCLUSION

The hybrid numerical method utilized here has been applied with some success to model the impact of metal projectiles and targets, over a wide range of velocities. The present work has described development of a rate dependent material model for Kevlar and three dimensional simulation work aimed at extending the formulation, for use in the computer aided design of multi-plate composite orbital debris shields. Both the geometry and the material composition of such shields complicate the simulation problem. The simulation results

conservatively estimate the protection afforded by multi-layered aluminum-Nextel-Kevlar shielding. Additional material modeling work, guided by impact tests focused on materials characterization issues, is expected to improve upon current simulation capabilities. The rather high computational cost of three dimensional multi-plate shield impact simulations emphasizes the importance of developing efficient parallel numerical implementations.

REFERENCES

[1] Christiansen EL, Crews JL, Williamsen JH, Robinson JH, Nolen AM. Enhanced Meteoroid and Orbital Debris Shielding. *International Journal of Impact Engineering*, 1995; **17**: 217-228.

[2] Boslough MB, Ang JA, Chhabildas WD, Reinhart CA, Hall CA, Cour-Palais BG¡ Christiansen EL, Crews JL. Hypervelocity Testing of Advanced Shielding Concepts for Spacecraft against Impacts to 10 km/s. *International Journal of Impact Engineering*, 1993; **14**: 95-106.

[3] Wang Y, Xia Y. The Effects of Strain Rate on the Mechanical Behavior of Kevlar Fibre Bundles: An Experimental and Theoretical Study. *Composites Part A*, 1998; **29A**: 1411-1415.

[4] Wang Y, Xia YM. Experimental and Theoretical Study on the Strain Rate and Temperature Dependence of Mechanical Behavior of Kevlar Fibre. *Composites Part A*, 1999; **30**: 1251-1257.

[5] Fahrenthold EP, Horban BA. An improved hybrid particle-element method for hypervelocity impact simulation. *International Journal of Impact Engineering*, 2001; **26**: 169-178.

[6] Fahrenthold EP. User's Guide for EXOS, 1999, University of Texas, Austin.

[7] 3M Corporation. *http* : *//www.3m.com/ceramics/misc/tech_notebook.jhtml*,2002.

[8] Yang HH. Kevlar Aramid Fiber, 1993, John Wiley & Sons Ltd.

[9] Fahrenthold EP, Shivarama R. Orbital debris impact simulation using a parallel hybrid particle-element code. *International Journal of Impact Engineering*, 2001; **26**: 179-188.

[10] Hiermaier SJ, Riedel W, Hayhurst CJ, Clegg RA, Wentzel CM. Advanced Material Models for Hypervelocity Impact Simulations, ESTEC Contract 12400/97/NL/PA(SC) Final Report, July, 1999

[11] Palmieri D. ATV Pressure Module MDPS: Determination of Ballistic Limit Through Numerical Simulation, European Space Agency Report, EWP-2167

[12] Destefanis R, Faraud M. Testing of Advanced Materials for High Resistance Debris Shielding. *International Journal of Impact Engineering*, 1997; **20**: 209-222.

[13] Grosch DJ. Inhibited Shaped Charge Launcher Testing of Spacecraft Shield Designs, April 1997, Southwest Research Institute, San Antonio, Texas.

[14] Christiansen EL, Kerr JH. Projectile Shape Effects on Shielding Performance at 7 km/s and 11 km/s. *International Journal of Impact Engineering*, 1997; **20**: 165-172.

[15] Steinberg DJ. Equation of State and Strength Properties of Selected Materials, 1996, Lawrence Livermore National Laboratory, UCRL-MA-106439.

[16] Fahrenthold EP. A continuum damage model for fracture of brittle solids under dynamic loading. *Journal of Applied Mechanics*, 1991; **58**: 904-909.

[17] Anderson CE. An overview of the theory of hydrocodes. *International Journal of Impact Engineering*, 1987; **5**: 33-59.

Yarn properties	Kevlar 29	Kevlar 49	Kevlar 129
Tensile Strength (Kpsi)	420	420	485
Initial Modulus	10.3	17.4	14
Elongation (%)	3.6	2.8	3.3
Density (lb/ft^3)	89.9	90.5	90.5

Table 1: Mechanical properties of Kevlar aramid fibers

Fiber type	Density (g/cm^3)	Strength (GPa)	Modulus (GPa)	Elongation (%)	Fiber diameter (μm)
Kevlar 129	1.45	3.4	99	3.3	12
Nextel	2.5	1.72	152	2	13

Table 2: Comparison of mechanical properties for Kevlar 129 and Nextel

Projectile mass (aluminum, L/D = 1)	1.07 g
Bumper thickness (aluminum)	0.127 cm
Nextel areal density	0.400 g/cm^2
Kevlar areal density	0.128 g/cm^2
Wall plate thickness (aluminum)	0.3175 cm
Total standoff	7.62 cm
Projectile velocity	11.25 km/s
Impact obliquity	45 degrees

Table 3: Parameters of SwRI test number 7139-24

Material property	Aluminum	Nextel	Kevlar
Shear modulus (Mbar)	0.271	0.164	0.100
Reference density (g/cc)	2.7	2.7	1.45
Reference sound speed (cm/μsec)	0.524	0.4968	0.5352
Reference yield stress (Mbar)	0.0029	0.0172	0.034
Strain hardening exponent	0.1	0.0	0.0
Strain hardening modulus	125.0	0.0	0.0
Melt temperature (degrees Kelvin)	1,220	1,220	700
Specific heat (Mbar-cm^3 per g-kilodegrees Kelvin)	0.00884	0.00884	0.00142
Spall stress (Mbar)	0.012	0.100	0.100
Plastic failure strain	1.0	1.0	1.0
Thermal expansion coefficient (per kilodegrees Kelvin)	0.0216	0.009	0.038
Mie-Gruneisen gamma	1.97	0.2513	0.7666
Mie-Gruneisen slope coefficient	1.4	1.0	1.0

Table 4: Material properties used in the simulation

Strain rate	0.0001 s^{-1}	0.01 s^{-1}	140 s^{-1}	440 s^{-1}	1350 s^{-1}
E (GPa)	97	100	112	119	125
σ_{max} (GPa)	2.34	2.47	2.94	3.02	3.08
ε_m (%)	3.29	3.33	3.54	3.64	3.86

Table 5: Mechanical properties of Kevlar 49 versus strain rate

Projectile mass (aluminum sphere)	1.0 g
Bumper thickness (aluminum)	0.16 cm
Nextel areal density	0.600 g/cm^2
Kevlar areal density	0.192 g/cm^2
Wall plate thickness (aluminum)	0.48 cm
Total standoff	11.4 cm
Projectile velocity	6.86 km/s
Impact obliquity	15 degrees

Table 6: Parameters of JSC test number B536

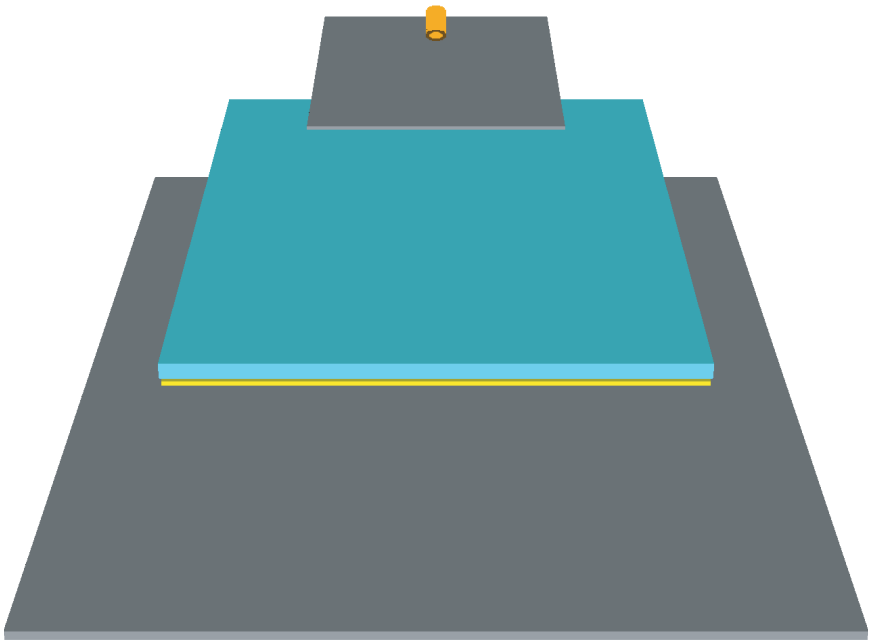

Figure 1: Element plot of the initial configuration

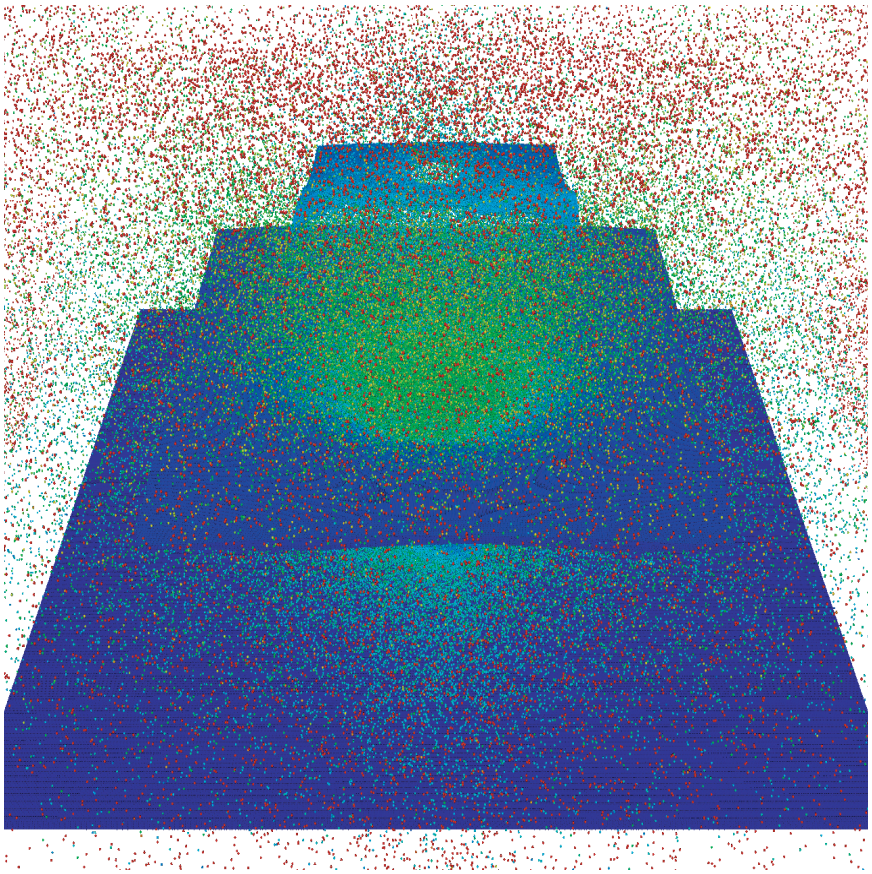

Figure 2: Particle plot of the simulation results at 100 microseconds after impact

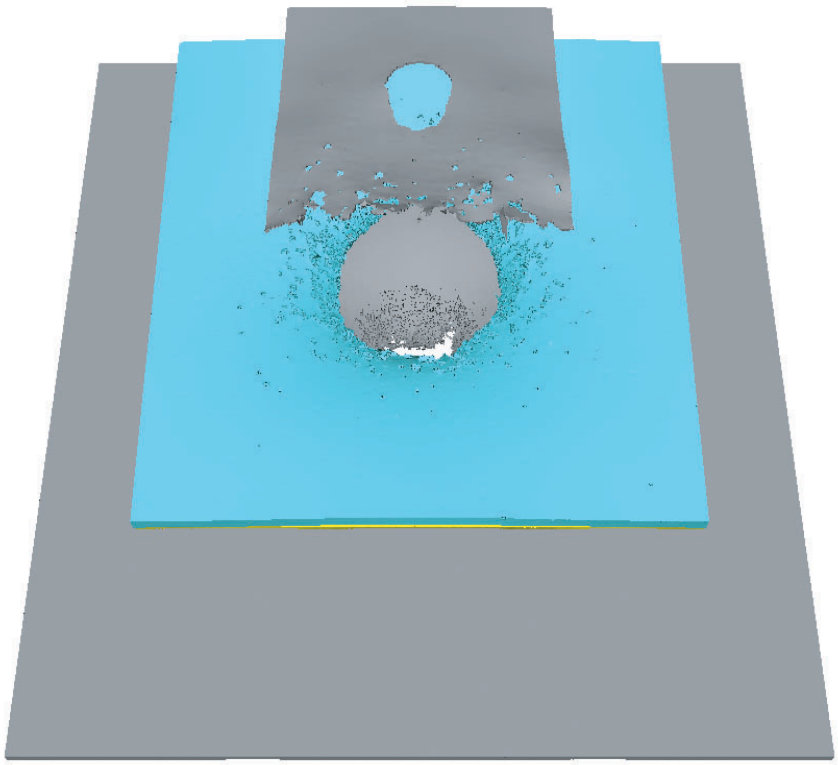

Figure 3: Element plot of the simulation results at 100 microseconds after impact

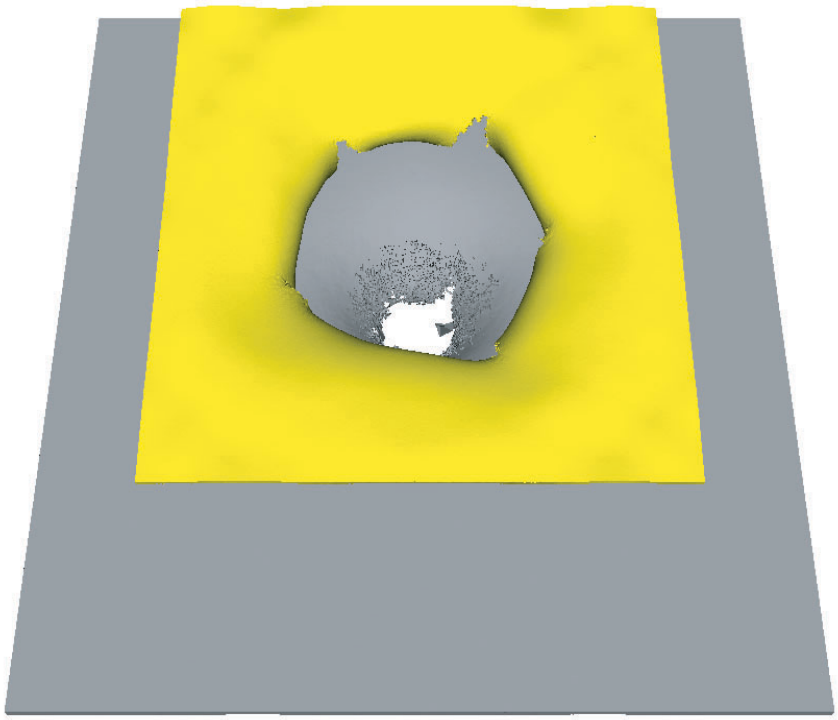

Figure 4: Element plot of the Kevlar shield and wall plate at 100 microseconds after impact

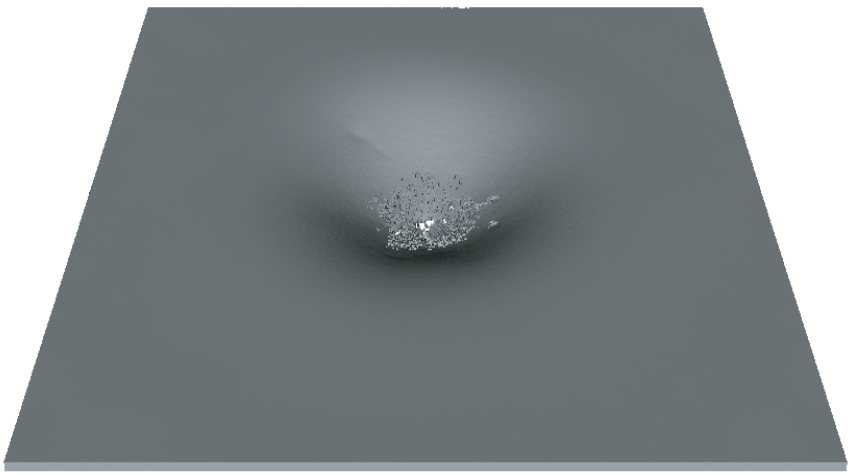

Figure 5: Element plot of the wall plate damage, spherical projectile

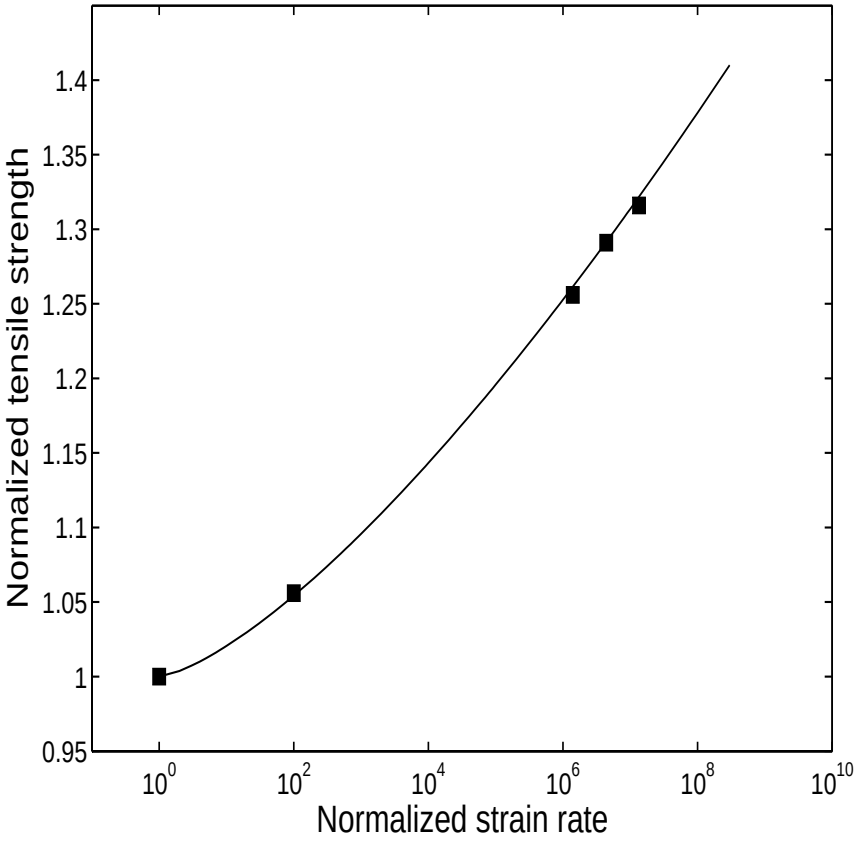

Figure 6: Strain rate dependence of tensile strength of Kevlar 49

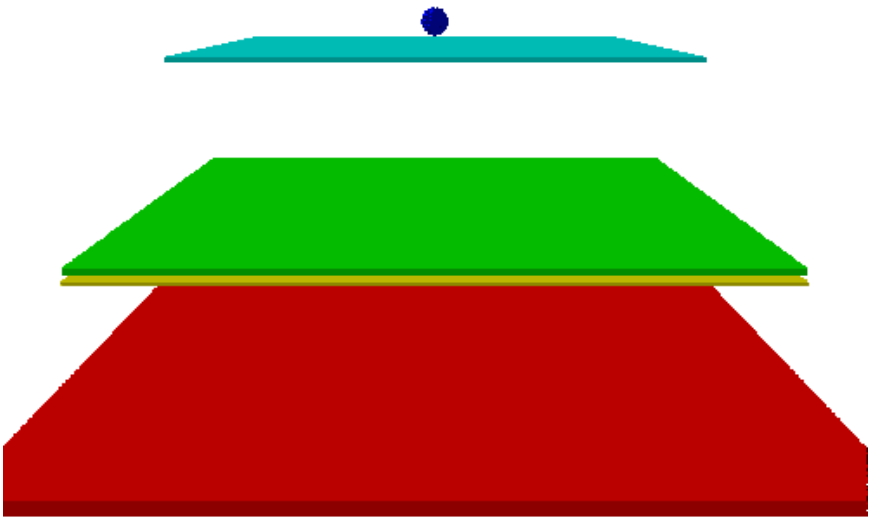

Figure 7: Element plot of the initial configuration

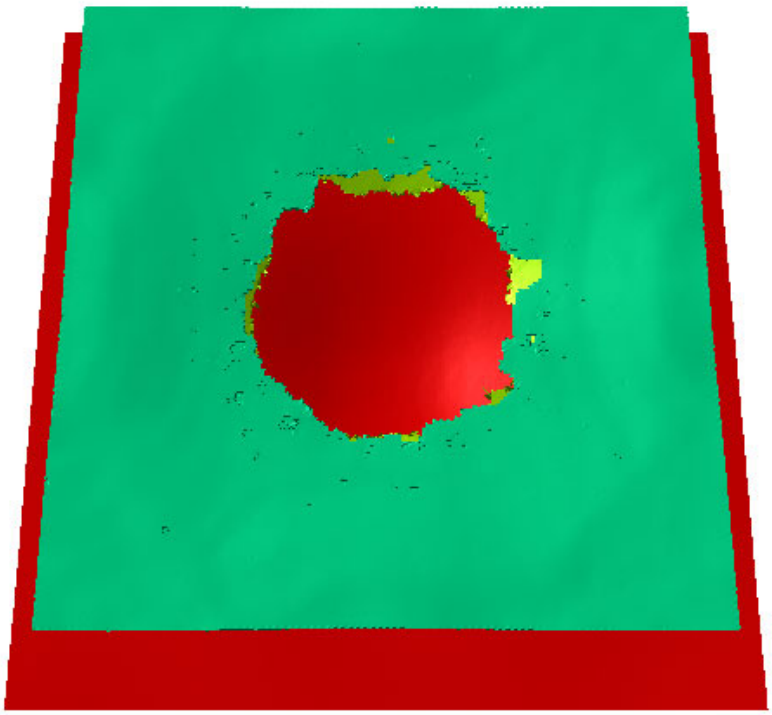

Figure 8: Element plot of the Kevlar shield and wall plate at 150 microseconds after impact

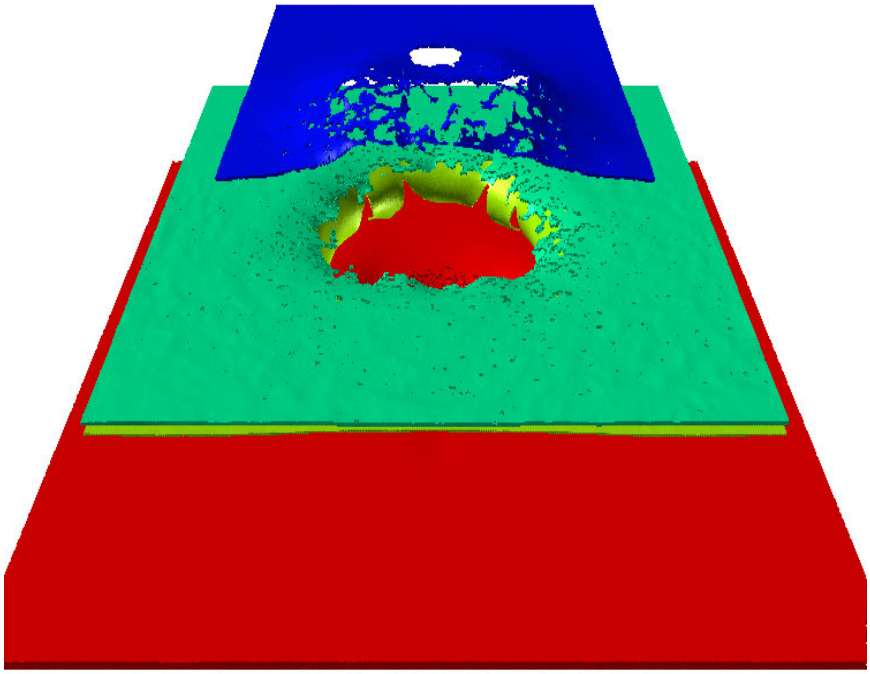

Figure 9: Element plot of the simulation results at 75 microseconds after impact (front view)

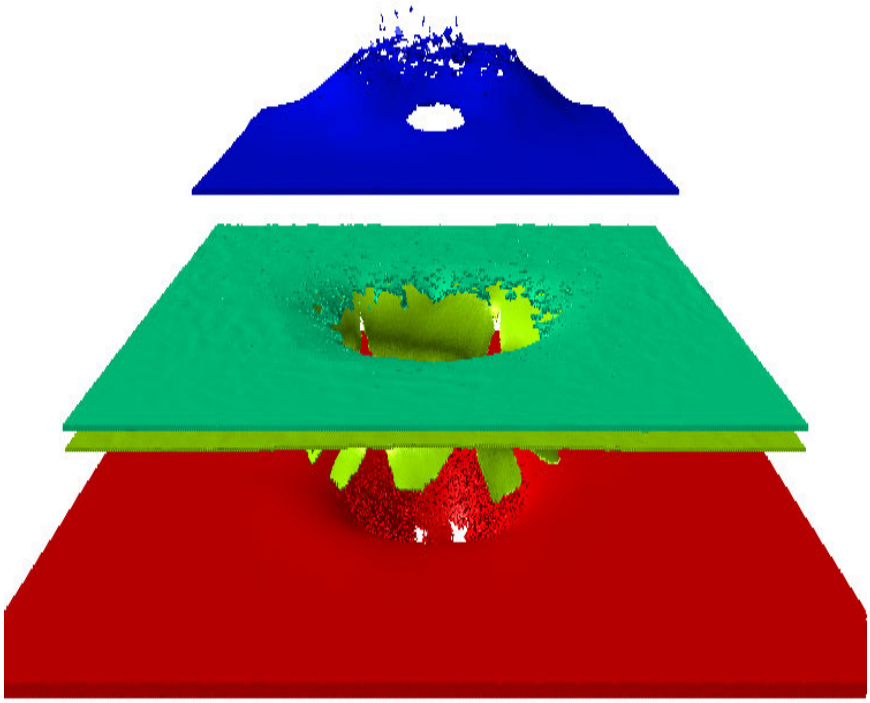

Figure 10: Element plot of the simulation results at 75 microseconds after impact (rear view)

CHAPTER 6

SIMULATION OF HYPERVELOCITY IMPACT EFFECTS ON REINFORCED CARBON-CARBON

Young-Keun Park[1] **and Eric P. Fahrenthold**[2]

Department of Mechanical Engineering, 1 University Station C2200
University of Texas, Austin, TX 78712, USA

[1]Graduate student

[2]Professor, corresponding author, phone: (512) 471-3064, email: epfahren@mail.utexas.edu

ABSTRACT

Spacecraft operating in low earth orbit face a significant orbital debris impact hazard. Of particular concern, in the case of the Space Shuttle, are impacts on critical components of the thermal protection system. Recent research has formulated a new material model of reinforced carbon-carbon, for use in the analysis of hypervelocity impact effects on the Space Shuttle wing leading edge. The material model has been validated in simulations of published impact experiments and applied to model orbital debris impacts at velocities beyond the range of current experimental methods. The results suggest that momentum scaling may be used to extrapolate the available experimental data base, in order to predict the size of wing leading edge perforations at impact velocities as high as 13 km/s.

NOMENCLATURE

d, shear damage variable	δ_{ij}, Kronecker delta
D, projectile diameter	$\mathbf{L}$, velocity gradient tensor
D_p, perforation diameter	$\mathbf{N}_e$, number of elements
D_c, coating spall diameter	$\mathbf{R}$, rotation matrix
$\mathbf{D}$, rate of deformation tensor	$\mathbf{S}$, deviatoric stress tensor
$\mathbf{e}$, Euler parameter vector	$\mathbf{S}^p$, effective stress tensor
$\overline{\mathbf{E}}$, deviatoric strain tensor	s, entropy density
$\mathbf{E}^e$, elastic strain tensor	v, impact velocity
$\mathbf{E}^p$, plastic strain tensor	Y, yield stress
ε^p, effective plastic strain	ψ, strain energy density
$\dot{\varepsilon}$, deviatoric strain rate	θ, temperature
$\mathbf{F}$, deformation gradient tensor	ϕ, impact obliquity

INTRODUCTION

Carbon-carbon composites offer an unusual combination of thermal and mechanical properties.[1] Their light weight and high temperature strength satisfy some very stringent design requirements for reusable orbital vehicles.[2] The wing leading edge of the Space Shuttle, subject to severe thermal re-entry loads, is constructed of reinforced carbon-carbon (RCC) panels, coated in silicon carbide to prevent oxidation.[3] Although the thermal properties of RCC composites are well understood,[4] much less is known about their dynamic mechanical properties. The loss of the Space Shuttle Columbia,[5] apparently due to impact damage on the wing leading edge, has motivated recent experimental[6] and computational[7] work aimed at developing a better understanding of the impact response of thermal protection materials.

The wing leading edge damage to Columbia was unexpected, the result of a relatively low velocity impact by a relatively low density projectile.[8] Another impact damage hazard, due to space debris in low earth orbit, has long been recognized. This threat involves projectiles of very low mass, but much higher density, and impact velocities as high 15 km/s. The debris shielding on the International Space Station is designed to defeat centimeter sized aluminum projectiles. Although the likelihood of such a projectile striking the Space Shuttle is quite low, orbital debris damage by much smaller projectiles is routinely observed during post-mission inspections of the vehicle. As a result previous experimental research has investigated the response of Space Shuttle thermal protection materials to orbital debris impact by spherical aluminum projectiles as large as 0.628 cm in diameter.[9]

Due to the high cost of carbon-carbon composites and the long fabrication lead times associated with the preparation of test samples, impact testing of RCC materials has been limited. In addition, the limitations of current experimental technology preclude hypervelocity impact testing over the entire projectile mass and kinetic energy range of interest. As a result, numerical simulation can serve as an important complement to experimental studies of the impact response of RCC materials. Numerical models validated by comparison with

experiment at velocities below 8 km/s can be used to extrapolate results into a higher velocity impact regime. A coordinated experimental and computational approach to the study of RCC response to insulating foam impacts has proven to be productive;[10] the present paper extends the latter computational work, to projectiles and impact velocities associated with orbital debris impact. In particular it develops a new anisotropic, rate-dependent material model for reinforced carbon-carbon, validates that model in three dimensional simulations of published hypervelocity impact experiments, and applies the validated formulation in simulations of impacts at velocities beyond the experimental range. The results indicate that a momentum scaling approach used to correlate the available experimental impact data may be extrapolated to describe RCC perforation by hypervelocity projectiles at velocities as high as 13 km/s.

The present paper is organized as follows. The first section outlines the hybrid particle-finite element method used in the present study, including the imbedded large deformation kinematics and general functional forms for the associated constitutive relations. The second section discusses published experimental results on the properties of RCC. The third section develops an RCC constitutive model, formulated for use in hypervelocity impact applications and reflecting important mechanical characteristics described in the material testing literature. The fourth section validates and applies the developed model in a series of three dimensional impact simulations. The last section presents conclusions and suggestions for related future work.

NUMERICAL METHOD

The material model described in this paper was developed for application in a specific numerical framework, the hybrid particle-finite element formulation of references 11 and 12. In order to provide appropriate context, this section summarizes the latter numerical formulation, details certain element level kinematics, and provides functional forms for the

required constitutive relations. The kinematic and constitutive modeling framework assumed here has wide scope, so that the material model described in the present paper may be adapted for use in shock physics codes which are based on alternative numerical modeling schemes.[13]

The hybrid particle-finite element model employed here takes an explicit state space form. The state equations consist of evolution equations for the following variables:

- translational and rotational momentum vectors for the three dimensional motion of ellipsoidal particles,
- center of mass position vectors and Euler parameters for the particles, the latter providing a singularity free description of particle rotations,
- density and entropy for each particle, and
- damage and plastic internal state variables for each finite element.

The state equations are derived using a thermomechanical formulation of the Lagrange equations. All inertia effects are modeled using the particles, whose mass centers are also nodal coordinates for the finite elements. The volumetric thermomechanical response of the modeled medium is described by an equation of state for the particles, which may take either an analytic or tabular form.

The material modeling work described in the present paper develops two specific components of the general numerical formulation:

- a strain energy density in shear, one part of the thermomechanical Lagrangian for the modeled particle-element system, and
- a plasticity model which specifies evolution equations for the plastic internal state variables, equations which serve as nonholonomic constraints on the system level model.

The strain energy density in shear takes the general functional form

$$\psi \;=\; \psi(d, \mathbf{e}, \overline{\mathbf{E}}, \mathbf{E}^p) \tag{1}$$

where d is a shear damage variable, $\overline{\mathbf{E}}$ is the total deviatoric strain, $\mathbf{E}^p$ is the plastic strain, and $\mathbf{e}$ is a vector of Euler parameters which relates a material reference frame for each element to a single global Cartesian reference frame. The evolution equations for the plastic strain components take the general functional form

$$\dot{\mathbf{E}}^p \;=\; \dot{\mathbf{E}}^p(s, d, \varepsilon^p, \dot{\varepsilon}, J, \mathbf{e}, \overline{\mathbf{E}}, \mathbf{E}^p) \tag{2}$$

where s is an entropy density, ε^p is the effective plastic strain, $\dot{\varepsilon}$ is a deviatoric strain rate, and

$$J = det(\mathbf{F}) \tag{3}$$

where $\mathbf{F}$ is the deformation gradient tensor.

The strain and strain rate variables which appear in the preceding functional forms are defined by the following large deformation kinematics.[14] The deviatoric strain is

$$\overline{\mathbf{E}} = \frac{1}{2}\left(\,\overline{\mathbf{C}} - \mathbf{I}\,\right) \tag{4}$$

where

$$\overline{\mathbf{C}} = \overline{\mathbf{F}}^T\overline{\mathbf{F}}, \qquad \overline{\mathbf{F}} = (det\,\mathbf{F})^{-\frac{1}{3}}\,\mathbf{F} \tag{5}$$

The elastic shear strain is defined as

$$\mathbf{E}^e = \overline{\mathbf{E}} - \mathbf{E}^p \tag{6}$$

where the flow rule for the plastic stain tensor must satisfy the isochoric plastic deformation constraint

$$tr\left(\mathbf{C}^{p-T}\dot{\mathbf{C}}^p\right) = 0, \qquad \mathbf{C}^p = \mathbf{I} + 2\,\mathbf{E}^p \tag{7}$$

The effective plastic strain is determined by integrating the rate relation

$$\dot{\varepsilon^p} = ||\dot{\mathbf{E}}^p|| \tag{8}$$

with the indicated invariant operator defined by

$$||\mathbf{T}|| = \left[\frac{1}{2}\, tr\left(\mathbf{T}^T\mathbf{T}\right)\right]^{1/2} \tag{9}$$

for any second order tensor $\mathbf{T}$. The deviatoric strain rate is

$$\dot{\varepsilon} = ||\mathbf{D}'||, \qquad \mathbf{D}' = \mathbf{D} - \frac{1}{3} tr(\mathbf{D})\, \mathbf{I} \tag{10}$$

where $\mathbf{D}$ is the rate of deformation tensor

$$\mathbf{D} = \frac{1}{2}\left(\mathbf{L} + \mathbf{L}^T\right), \qquad \mathbf{L} = \dot{\mathbf{F}}\, \mathbf{F}^{-1} \tag{11}$$

with $\mathbf{L}$ the velocity gradient tensor.

In the case of anisotropic materials, the constitutive response is described in a material reference frame. Here an Euler parameter vector

$$\mathbf{e} = [e_0\, e_1\, e_2\, e_3]^T, \qquad \mathbf{e}^T\mathbf{e} = 1 \tag{12}$$

is used to define a rotation matrix ($\mathbf{R}$) for each element

$$\mathbf{R} = \mathbf{A}\, \mathbf{G}^T \tag{13}$$

$$\mathbf{A} = \begin{bmatrix} -e_1 & e_0 & -e_3 & e_2 \\ -e_2 & e_3 & e_0 & -e_1 \\ -e_3 & -e_2 & e_1 & e_0 \end{bmatrix} \tag{14}$$

$$\mathbf{G} = \begin{bmatrix} -e_1 & e_0 & e_3 & -e_2 \\ -e_2 & -e_3 & e_0 & e_1 \\ -e_3 & e_2 & -e_1 & e_0 \end{bmatrix} \tag{15}$$

which relates a material reference frame in each element to the global Cartesian system used in the numerical simulations. The rotation matrix relates vector components $\mathbf{p}$ in the global

coordinate system to corresponding components $\mathbf{q}$ described in the material reference frame, using

$$\mathbf{p} = \mathbf{R}\,\mathbf{q} \tag{16}$$

The corresponding transformation relation for second order tensors is

$$\mathbf{P} = \mathbf{R}\,\mathbf{Q}\,\mathbf{R}^T \tag{17}$$

where the components $\mathbf{P}$ refer to the global frame and the components $\mathbf{Q}$ refer to the material reference frame.

REINFORCED CARBON-CARBON

The published material property data base for carbon-carbon composites is limited by material costs and proprietary considerations. On the other hand, the complex nature of both the material and the application of interest here means that a rather wide range of experiments are needed to fully characterize its constitutive response. This section discusses some properties of RCC of particular significance in hypervelocity impact applications.

The most directly relevant experimental results are those of Lu et al.,[6] who performed tests at Sandia National Laboratories on samples taken from Space Shuttle wing leading edge panels, in support of the Columbia accident investigation. They provide data on elastic moduli as well as strength measurements obtained from tension, bending, and compression tests. Although the elastic moduli measured in tension and compression were similar, strength in compression was approximately double that in tension. In addition they reported a strain rate dependence of the tensile strength, observing a fifteen percent increase in strength as the loading rate increased from 1 to 200 sec^{-1}. Finally they noted that removal of the silicon carbide coating from the tested samples showed little effect on the measured mechanical properties.

Several different authors have reported results of shear tests performed on carbon-carbon composites.[15−20] In the case of the RCC, interlaminar shear strength and stiffness is of interest, since oblique hypervelocity impacts will in general lead to multi-axial loading. The published shear test data show that interlaminar shear stiffness and strength can differ by factors of approximately two and four respectively, from their in-plane counterparts.

Perhaps the most unusual property of RCC is its increase in strength with temperature,[17,21] by as much as a factor of two, as compared to the thermal softening response observed in metals. The high temperature strength of RCC is important in hypervelocity impact applications, due to the adiabatic heating typically associated with shock loading.

The preceding references, along with the equation of state literature[22] and published data on the thermal properties of RCC,[4,23] were used to estimate the material parameters used in the simulations reported in a later section. Although additional tests on Space Shuttle wing leading edge panels, like those reported by Lu at al., are needed, the cited references represent the best data available to the authors at the time the simulations were conducted.

MATERIAL MODEL

Composite materials are used in structural,[24] orbital debris shielding,[25] and thermal protection[4] applications on a variety of spacecraft, hence their response to hypervelocity impact effects has been analyzed in a number of previous experimental[26] and computational[27] studies. Previous material modeling work has considered both micromechanical[28] and anisotropic continuum models. The present paper employs an anisotropic continuum approach, since the high computational cost of micromechanical models normally precludes their use in structural scale simulations. Large deformation, anisotropic continuum models of composite materials[29,30] normally address shock physics problems by extending small strain formulations originally developed for applications in structural mechanics. In an alternative approach, the present work starts with the finite strain, hybrid particle-element kinematics

discussed in an earlier section, and then formulates: (1) an anisotropic strain energy density function which depends on a general deviatoric Lagrangian strain tensor, and (2) an anisotropic, temperature and rate dependent plastic flow rule which depends on an effective stress[31] and satisfies a general isochoric deformation constraint. Both the strain energy density function and the plastic flow rule: (1) account for differences in material response under tension and compression, (2) account for material reference frame dependence under large deformations, and (3) satisfy first and second law thermodynamic constraints. The approach used here has been applied with success to model isotropic materials.[32] It is motivated by a focus on hypervelocity problems, where large deformation dynamics are of central interest, and by the kinematic form of the hybrid numerical method used in the present paper. As indicated in the later section on simulations, this material modeling approach provides an accurate description of hypervelocity impact effects in reinforced carbon-carbon. Potential application of the formulation to model impact in other composites, such as graphite-epoxy or Kevlar-epoxy, is of interest for future work.

In the case of an orthotropic material, with distinct elastic moduli in tension and compression, the shear strain energy density per unit reference volume is

$$\begin{aligned} \psi &= (1-d)\,\mu_o\,\frac{1}{2}\sum_{i=1}^{3}\mu_{ii}\left[(1+\gamma_i)+(1-\gamma_i)\,sgn(E^{em}_{ii})\right](E^{em}_{ii})^2 + \\ &\quad (1-d)\,\mu_o\sum_{i=1}^{3}\sum_{j=1}^{3}(1-\delta_{ij})\,\mu_{ij}\,(E^{em}_{ij})^2 \end{aligned} \tag{18}$$

where δ_{ij} is the Kronecker delta, μ_o is a reference elastic modulus, and the parameters $\mu_{ij} = \mu_{ji}$ are dimensionless constants. The parameters γ_i are the ratios of the elastic moduli in compression to those in tension, while the E^{em}_{ij} are the components of the elastic shearing strain, expressed in a material reference frame. Note that this function is analytic, since a change in modulus from tension to compression occurs when the corresponding material strain component is zero.

A plastic flow rule for an anisotropic, rate dependent material, which satisfies the afore-

mentioned isochoric plastic deformation constraint, may be obtained by extending a large strain Lagrangian formulation previously developed for use in hypervelocity impact applications.[32,33] The flow rule is

$$\dot{\mathbf{E}}^p = \frac{\dot{\lambda}}{||\mathbf{S}^p||} \underline{\underline{\mathbf{N}}}^p \, \underline{\underline{\mathbf{N}}} \, \underline{\underline{\mathbf{M}}} \, \underline{\underline{\mathbf{M}}}^p \, \mathbf{S}^p \tag{19}$$

where $\dot{\lambda}$ is a positive proportionality coefficient, $\mathbf{S}^p$ is the effective stress,

$$\mathbf{S}^p = \underline{\underline{\mathbf{M}}}^{pT} \, \underline{\underline{\mathbf{M}}}^T \, \underline{\underline{\mathbf{N}}}^T \, \underline{\underline{\mathbf{N}}}^{pT} \, \mathbf{S} \tag{20}$$

and $\mathbf{S}$ is the deviatoric stress tensor

$$\mathbf{S} = \frac{\partial \psi}{\partial \mathbf{E}^e} \tag{21}$$

The first two coefficients in the flow rule impose the isochoric plastic deformation constraint, and are defined by

$$\underline{\underline{\mathbf{N}}}^p \, \mathbf{T} = \frac{1}{2 \, ||\mathbf{C}^p||} (\mathbf{C}^p \, \mathbf{T} + \mathbf{T} \, \mathbf{C}^p) \tag{22}$$

and

$$\underline{\underline{\mathbf{N}}} \, \mathbf{T} = \mathbf{T} - \frac{1}{3} tr(\mathbf{T}) \, \mathbf{I} \tag{23}$$

for any symmetric second order tensor $\mathbf{T}$. The third coefficient performs a component transformation from a material reference frame to a fixed global frame, and is defined by

$$\underline{\underline{\mathbf{M}}}^T \, \mathbf{T} = \mathbf{R}^T \, \mathbf{T} \, \mathbf{R} \tag{24}$$

for any symmetric second order tensor $\mathbf{T}$. The last coefficient in the flow rule defines an effective stress transformation, in a material reference frame, using

$$\underline{\underline{\mathbf{M}}}^{pT} \, \mathbf{P} = \mathbf{Q} \tag{25}$$

for symmetric second order tensors $\mathbf{P}$ and $\mathbf{Q}$, with component forms

$$Q_{ii} = \frac{2 \, \alpha_{ii} \, P_{ii}}{(1 + \beta_{ii}) + (1 - \beta_{ii}) \, sgn(E^{em}_{ii})} \quad , \qquad i = 1, 2, 3 \tag{26}$$

and

$$Q_{ij} = \frac{2\,\alpha_{ij}\,P_{ij}}{(1+\beta_{ij}) + (1-\beta_{ij})\;sgn(J-1)} \quad , \qquad i \neq j \tag{27}$$

The parameter $\alpha_{ij} = \alpha_{ji}$ is the ratio of a reference yield stress to the yield stress for the ijth stress component, while the parameter $\beta_{ij} = \beta_{ji}$ is the ratio of the strength in compression to that in tension for the ijth stress component.

The rate dependent, strain hardening, thermal softening yield function is

$$f = ||\mathbf{S}^p|| - Y \tag{28}$$

where Y is the yield stress

$$Y = \frac{1}{2}\,(1-d)\,Y_o\,\left(1-\kappa\,\theta^H\right)\,(1+\eta\,\varepsilon^p)^n\,\left[1+\zeta\;log\left(\frac{\dot{\varepsilon}}{\dot{\varepsilon}_o}\right)\right]^m \tag{29}$$

with Y_o the reference yield stress, η a strain hardening coefficient, n a strain hardening exponent, ζ a strain rate hardening coefficient, m a strain rate hardening exponent, $\dot{\varepsilon}_o$ a reference strain rate, κ a thermal softening coefficient, and θ^H the homologous temperature

$$\theta^H = \frac{\theta - \theta_o}{\theta_m - \theta_o} \tag{30}$$

where θ_o and θ_m are reference and melt temperatures.

In a numerical implementation, the aforementioned plastic flow rule is expressed in incremental form. That is the incremental plastic strain at each time step is computed using the incremental proportionality coefficient

$$\Delta\lambda = max\left(0\,,\,\frac{||\mathbf{S}^p|| - Y}{(1-d)\,2\,\mu_o}\right) \tag{31}$$

The shear damage variable (d) models the transition from an intact to a failed medium, evolving from an initial value of 0 to a final value of 1 over a fixed number of time steps[34] when any stipulated element failure criterion is satisfied. The simulations discussed in the next section incorporate accumulated plastic strain, melt temperature, and maximum compression failure criteria, although other criteria may be accommodated.

IMPACT SIMULATIONS

The material model just described was applied in a series of three dimensional simulations of hypervelocity impacts on reinforced carbon-carbon. The simulations employed a hybrid particle-finite element method and the material properties listed in Tables 1 and 2. An initial set of simulations was used to validate the material model, compare results obtained using analytic (Mie Gruneisen) and tabular[35] (SESAME 3715) equations of state, and check numerical convergence of the simulation results. A second series of simulations was then performed to estimate orbital debris impact effects at velocities beyond the range of current experimental methods.

The first set of eight simulations modeled NASA JSC experiments B1028 and B1040,[9] which involved oblique impacts of aluminum spheres on reinforced carbon-carbon target plates at a velocity of seven kilometers per second. The target plates were 0.63 cm in thickness, including upper and lower surface coatings composed of silicon carbide, each 0.08 cm in thickness. Table 3 lists the simulation parameters, including projectile diameter (D), impact velocity (v), impact obliquity (ϕ, with zero degrees a normal impact), number of elements spanning the target thickness (N_e), and the equation of state used to model the aluminum projectile. Tabular equation of state data was not available for the target materials.

Figures 1 through 4 show example plots for a simulation of experiment B1028. Figure 1 shows the initial configuration while Figures 2 through 4 show the simulation results at 50 microseconds after impact. The sectioned plot in Figure 4 depicts plate perforation and coating spall similar to that observed in the corresponding experiment. Table 3 lists simulation results for the diameter of the RCC perforation (D_p) and the average diameter of the target region over which the silicon carbide coating was removed (D_c). The results of the validation simulations suggest the following conclusions:

- the material model developed here can provide good estimates of both the RCC perforation diameter and the extent of the spalled coating region, for oblique impacts at seven kilometers per second,
- accurate estimates of the RCC perforation diameter require a mesh resolution sufficient to place 8 elements across the target plate,
- accurate estimates of the diameter of the spalled coating region require a mesh resolution sufficient to place 16 elements across the target plate, and
- the simulation results are not sensitive to the choice of projectile equation of state.

Table 4 shows the relative computational cost of simulations of experiments B1028 and B1040 run at three different mesh densities. As is well known, in three dimensional models the particle count increases with the cube of the increase in resolution, while the time step decreases linearly with the increase in resolution, so that the total computational cost of high resolution models is considerable.

A second set of twelve simulations was performed to investigate orbital debris impact effects at velocities beyond the current experimental range. The simulations involved spherical aluminum projectiles, at three different projectile diameters, an impact obliquity of 30 degrees and impact velocities of 7, 10, and 13 km/s. In the case of the largest projectile, simulations were performed using both an analytic and a tabular equation of state. The target assumed in these simulations was identical to that involved in the aforementioned experiments. In the target mesh 8 elements spanned the plate thickness, so that the resolution level was sufficient to estimate the diameter of the RCC perforations, but not the extent of the region of coating spall. Figure 5 shows simulation results for the diameters of the RCC perforations, as a function of projectile diameter, impact velocity, and projectile equation of state. In Figure 5, MG denotes the Mie Gruneisen analytic equation of state, while SES

denotes the SESAME tabular equation of state. The results of these simulations suggest the following conclusions, for the impact velocity range and impact obliquity considered:

- perforation diameters increase with both projectile size and impact velocity, over the full range of the simulations,
- for a fixed projectile size, perforation diameters increase with impact velocity at an approximately linear rate,
- for a fixed impact velocity, perforation diameters increase with projectile size, but at a declining rate, and
- the simulation results are not sensitive to the choice of projectile equation of state.

Note that Figure 5 is not a ballistic limit plot; rather it plots perforation diameter versus impact velocity, so that the indicated trends are not unexpected.

Although the preceding results are informative, they consider only a limited rage of projectile size and obliquity. Hence the scaling of the simulation results, as compared to the available experimental data, is of considerable interest. Figure 6 shows a plot of perforation diameter versus normal impact momentum for the 11 different projectile size and impact velocity combinations modeled in the present computational study, as well as corresponding data for 15 published experiments.[9,36] The experiments involved projectile diameters ranging from 0.039 to 0.628 cm, impact velocities ranging from 2.49 to 7.32 km/s, and impact obliquities ranging from 0 to 80 degrees. The simulations involved a more limited range of projectile diameters (0.123 to 0.360 cm) and obliquities (30 to 45 degrees), but a much higher range of impact velocities (7 to 13 km/s). All of the simulations and experiments of course involved the same target configuration. The data in Figure 6 suggests that the experimental and simulation results for the diameters of RCC perforations scale with normal impact momentum in a similar fashion. Although these results do not establish a universal

scaling relation for the problem of interest, they do suggest that the scaling of perforation size with normal impact momentum observed in experiments below 8 km/s may be extrapolated to much of the velocity range of interest in orbital debris impact applications.

CONCLUSION

The present paper has formulated an anisotropic, rate dependent material model for use in the simulation of hypervelocity impact problems. The material model was developed to study orbital debris impact effects on reinforced carbon-carbon materials, and has been validated in simulations of hypervelocity impact experiments conducted at 7 km/s. The validated model was applied to simulate impacts at velocities beyond the experimental range. The results indicate that momentum scaling analysis, used to correlate a wide range of experiments below 8 km/s, has application in predicting perforation diameters for reinforced carbon-carbon targets at velocities as high as 13 km/s. The ability of reinforced carbon-carbon to retain its strength at high temperatures suggests that accurate strength models of this material are important in simulations of impact effects over the entire orbital debris velocity range.

Some conclusions relevant to future work are suggested:

- additional high resolution simulations are needed in order to investigate the spallation of silicon carbide coating at velocities above the current experimental range,
- additional mechanical properties testing is needed, at elevated temperatures and high strain rates, to support the development and validation of improved strength models for reinforced carbon-carbon,
- additional equation of state research is needed, to provide tabular data applicable to reinforced carbon-carbon materials over a wide range of impact velocities, and

- the development of advanced thermal protection materials should in the future include experimental work aimed at detailed characterization of their mechanical as well as their thermal properties.

The use of composite materials in spacecraft applications complicates both experimental and computational studies of impact effects. High cost materials with long fabrication lead times, such as reinforced carbon-carbon, and the limitations of current experimental impact techniques motivate the increased use of computer simulation in the design of spacecraft for micrometeoroid and orbital debris impact effects.

Acknowledgments — This work was supported by NASA Johnson Space Center (NAG 9-1244) and by the National Science Foundation (CMS 99-12475). Computer time support was provided by the Texas Advanced Computing Center at the University of Texas at Austin and the Arctic Region Supercomputing Center at the University of Alaska Fairbanks.

REFERENCES

1. T. Windhorst and G. Blount, 1997, "Carbon-Carbon Composites: a Summary of Recent Developments and Applications," Materials and Design, volume 18, Number 1, pp. 11-15.

2. D.L. Schmidt, K.E. Davidson and L.S. Theibert, 1999, "Unique Applications of Carbon-Carbon Composite Materials (Part One)," SAMPE Journal, Volume 35, pp. 27-39.

3. G. Savage, 1993, "Carbon-Carbon Composites," Chapman and Hall, London.

4. C.W. Ohlhorst, W.J. Vaughn, P.O. Ransone, and H.T. Tsou, 1997, "Thermal Conductivity Database of Various Structural Carbon-Carbon Composite Materials," NASA TM 1997-4787.

5. Report of the Columbia Accident Investigation Board, Volume 1, Government Prining Office, Washington, DC, August 2003.

6. W.-Y. Lu, B.R. Antoun, J.S. Korellis, S. Scheffel, M.Y. Lee, R.D. Hardy, and L.S. Costin, "Material Characterization of Shuttle Thermal Protection System for Impact Analyses," AIAA-2004-0945, presented at the 2004 AIAA Aerospace Sciences Meeting, Reno, Nevada, January 5-8,2004.

7. K.W. Gwinn and K.E. Metzinger, "Analysis of Foam Impact Onto the Columbia Shuttle Wing Leading Edge Panels Using Pronto3D/SPH," AIAA-2004-0942, presented at the 2004 AIAA Aerospace Sciences Meeting, Reno, Nevada, January 5-8,2004.

8. J.H. Kerr, D.J. Grosch, and E.L. Christiansen, "Impact Testing of Large Foam Projectiles," AIAA-2004-0939, presented at the 2004 AIAA Aerospace Sciences Meeting, Reno, Nevada, January 5-8,2004.

9. E.L. Christiansen and L. Friesen, 1997, "Penetration Equations for Thermal Protection Materials," International Journal of Impact Engineering, Volume 20, pp. 153-164.

10. Fahrenthold, EP, and Park, YK. "Simulation of foam impact effects on the space shuttle thermal protection system.," AIAA Journal of Spacecraft and Rockets, in press.

11. Fahrenthold, E.P., and Horban, B.A., 2001, "An improved hybrid particle-finite element method for hypervelocity impact simulation," International Journal of Impact Engineering, Vol. 26, pp. 169-178.

12. Shivarama, R., and Fahrenthold, E.P., 2004, "An ellipsoidal particle-finite element method for hypervelocity impact simulation," International Journal for Numerical Methods in Engineering, Volume 59, pp. 737-753.

13. J.M. McGlaun, S.L. Thompson, and M.G. Elrick, 1990, "CTH: A three dimensional shock wave physics code," International Journal of Impact Engineering, Volume 10, pp. 351-360.

14. L.E. Malvern, 1969, Introduction to the Mechanics of a Continuous Medium, Prentice Hall, Englewood Cliffs, New Jersey.

15. M.S. Aly-Hassan, H. Hatta, S. Wakayama, M. Watanabe and K. Miyagawa, 2003, "Comparison of 2D and 3D Carbon/Carbon Composites with respect to Damage and Fracture Resistance," Carbon, Volume 41, pp. 1069-1078.

16. K. Anand, V. Gupta and D. Dartford, 1994, "Failure Mechanisms of Laminated Carbon-Carbon Composites - II. Under Shear Loads," Acta metallurgica et materialia, volume 42, Number 3, pp.797-809.

17. E. Fitzer and L.M. Manocha, 1998, "Carbon Reinforcements and Carbon/Carbon Composites," Springer-Verlag, Berlin, Heidelberg, New York.

18. F. Abali, A. Pora and K. Shivakumar, 2003, "Modified Short Beam Shear Test for Measurement of Interlaminar Sheear Strength of Composites," Journal of Composite Materials, Volume 37, Number 5, pp.453-464.

19. C.G. Papakonstantinou, P. Balaguru and R.E. Lyon, 2001, "Comparative Study of High Temperature Composites," Composites: Part B, Volume 32, pp. 637-649.

20. L.C. Edgar, B. David and K.F. Mattison, 1996, "The Interlaminar tensile and Shear Behavior of a Unidirectional C-C Composite," Journal of Nuclear Materials, Volume 230, pp.226-232.

21. J.D. Buckley and D.D. Edie, 1993, "Carbon-Carbon Materials and Composites," Noyes Publications, New Jersey.

22. Steinberg DJ. Equation of State and Strength Properties of Selected Materials, 1996, Lawrence Livermore National Laboratory, UCRL-MA-106439.

23. K.J. Dowding, J.V. Beck and B.F. Blackwell, 1996, "Estimation of Directional-Dependent Thermal Properties in a Carbon-Carbon Composite," International Journal of Heat Mass Transfer, Volume 39, Number 15, pp. 3157-3164.

24. Christiansen, E.L., 1990, "Investigation of Hypervelocity Impact Damage to Space Station Truss Tubes," International Journal of Impact Engineering, Volume 10, pp. 125-133.

25. Destefanis, R., and Faraud, M., 1997, "Testing of Advanced Materials for High Resistance Debris Shielding," International Journal of Impact Engineering, Volume 20, pp. 209-222.

26. Yew, C.H., and Kendrick, R.B., 1987, "A Study of Damage in Composite Panels Produced by Hypervelocity Impact," International Journal of Impact Engineering, Volume 5, pp. 792-738.

27. Palmieri, D., Destefanis, R., Faraud, M., and Lambert, M., 2003, "Penetration Effectiveness of Inhibited Shaped Charge Launcher Projectiles and Solid Spheres on Spacecraft Shields," International Journal of Impact Engineering, Volume 29, pp. 513-526.

28. Silling SA, Taylor, PA, Wise, JL, and Furnish, MD. Micromechanical Modeling of Advanced Materials, 1994, SAND94-0129, Sandia National Laboratories.

29. Logan, RW. Incorporating Non-quadratic and Crystallographic Yields Surfaces in Finite Element Codes, 1988, LA-CP-88-186, Los Alamos National Laboratory, Los Alamos, New Mexico.

30. Hayhurst, CJ, Livingstone, IHG, Clegg, RA, Destefanis, R, and Faraud, M, 2001,"Ballistic Limit Evaluation of Advanced Shielding Using Numerical Simulations," International Journal of Impact Engineering, Volume 26, pp. 309-320.

31. Hill, R. The mathematical theory of plasticity, 1950, Oxford University Press.

32. Fahrenthold EP, Horban BA. , 1997, "Thermodynamics of continuum damage and fragmentation models for hypervelocity impact, " International Journal of Impact Engineering, Volume 20, pp. 241-252.

33. E.P. Fahrenthold and Y.K. Park, "Simulation of hypervelocity impact on aluminum-Nextel-Kevlar orbital debris shields," International Journal of Impact Engineering, Volume 29, 2003, pp. 227-235.

34. Silling SA. CTH Reference Manual: Johnson-Holmquist Ceramic Model, 1992, SAND92-0576, Sandia National Laboratories.

35. Lyon SP, Johnson JD, editors. SESAME: The Los Alamos National Laboratory Equation of State Database, LA-UR-92-3407, Los Alamos National Laboratory, Los Alamos, New Mexico.

36. F. Lyons, E.L. Christiansen, and J.H. Kerr. Hypervelocity Impact Testing of Reinforced Carbon-Carbon Composites, May 1998, Report JSC 23898, NASA Johnson Space Center.

Table 1. Material properties

Material property	Aluminum	Silicon Carbide	RCC
Reference bulk modulus ($Mbar$)	0.784	2.21	0.0576
Reference shear modulus ($Mbar$)	0.271	0.240	0.0718
Reference soundspeed ($cm\,\mu sec^{-1}$)	0.539	0.829	0.191
Mie-Gruneisen gamma	1.97	0.95	0.24
Mie-Gruneisen slope	1.34	1.21	1.33
Reference density ($g\,cm^{-3}$)	2.70	3.21	1.58
Reference yield stress ($kbar$)	2.90	0.771	0.771
Specific heat ($bar\,cm^3\,g^{-1}\,^\circ K^{-1}$)	8.84	7.12	7.12
Strain hardening coefficient	125	10	2
Strain hardening exponent	0.1	1.0	1.0
Strain rate hardening coefficient	0.0	0.0	0.1
Strain rate hardening exponent	0.0	0.0	1.0
Reference strain rate (sec^{-1})	0	0	0.01
Thermal softening coefficient	0.567	0.0	-1.0
Melt temperature ($^\circ K$)	1,220	3,840	3,840
Maximum compression	100	100	100
Plastic failure strain	1.00	0.10	0.50

Table 2. Material model parameters

Parameters	Silicon Carbide	Reinforced carbon-carbon
$\gamma_1 = \gamma_2 = \gamma_3$	0.10	1.00
$\mu_{11} = \mu_{22} = \mu_{33} = \mu_{13}$	1.00	1.00
$\mu_{12} = \mu_{23}$	1.00	0.50
$\alpha_{11} = \alpha_{22} = \alpha_{33} = \alpha_{13}$	1.00	1.00
$\alpha_{12} = \alpha_{23}$	1.00	3.73
$\beta_{11} = \beta_{22} = \beta_{33}$	2.00	2.00
$\beta_{12} = \beta_{13} = \beta_{23}$	2.00	2.00

Table 3. Numerical results, simulations of NASA JSC experiments B1028 and B1040

Test number	D (cm)	v (km/s)	ϕ (deg)	N_e	Equation of state	D_p (cm)	Error (%)	D_c (cm)	Error (%)
B1028	0.628	7.01	45	8	Mie Gruneisen	2.60	10.3	3.74	15.0
				8	SESAME 3715	2.65	8.6	3.60	18.2
				16	Mie Gruneisen	2.66	8.3	4.05	8.0
				24	Mie Gruneisen	2.67	7.9	4.08	7.3
B1040	0.478	6.96	30	8	Mie Gruneisen	2.12	3.6	2.95	21.3
				8	SESAME 3715	1.97	10.5	2.95	21.3
				16	Mie Gruneisen	2.00	10.0	3.38	9.9
				24	Mie Gruneisen	2.10	4.5	3.48	7.2

Table 4. Computer resource requirements, simulations of NASA JSC experiments

Test number	N_e	Total particles (million)	Total elements (million)	Number of processors	Wall clock hours
B1028	8	0.078	0.036	16	14
	16	0.572	0.275	64	65
	24	1.857	0.905	64	340
B1040	8	0.078	0.036	32	5
	16	0.572	0.275	64	74
	24	1.856	0.905	64	347

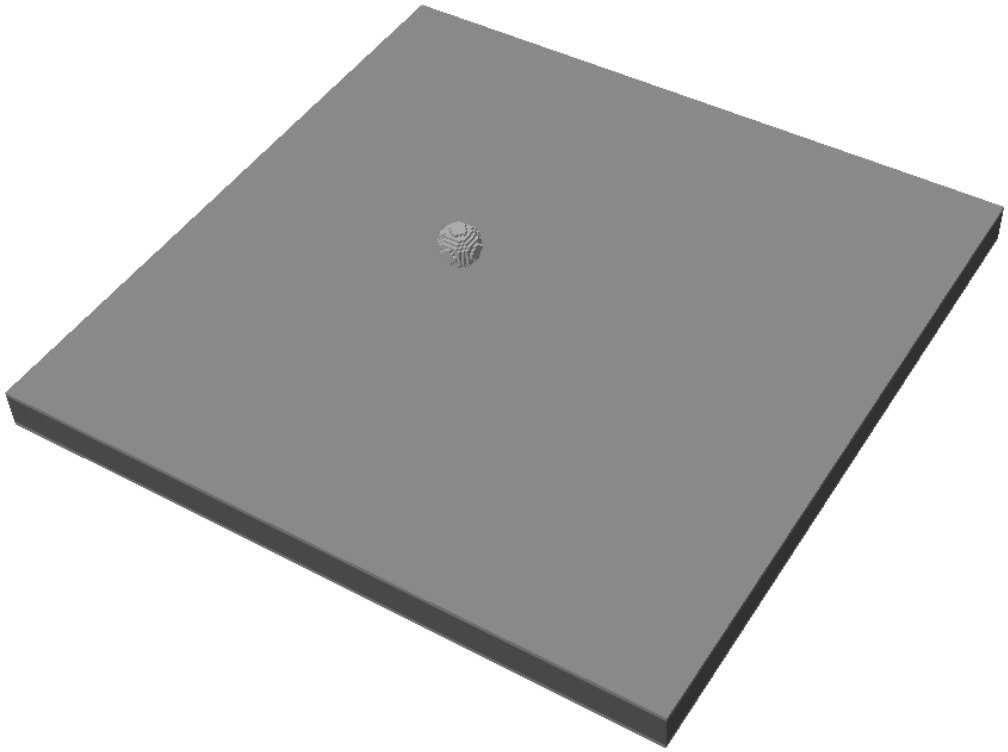

Figure 1. Initial configuration, simulation of NASA JSC experiment B1028.

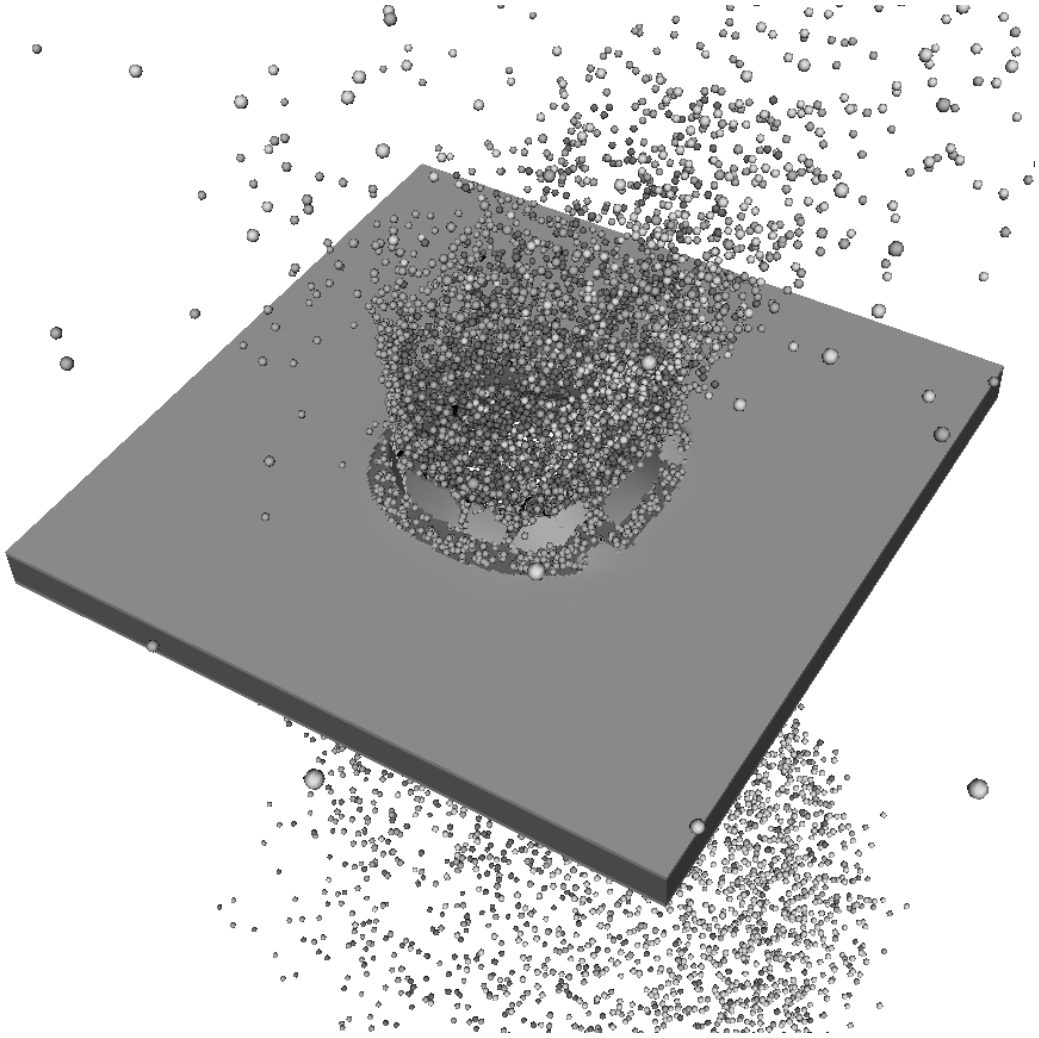

Figure 2. Particle-element plot of the simulation results at 50 microseconds after impact.

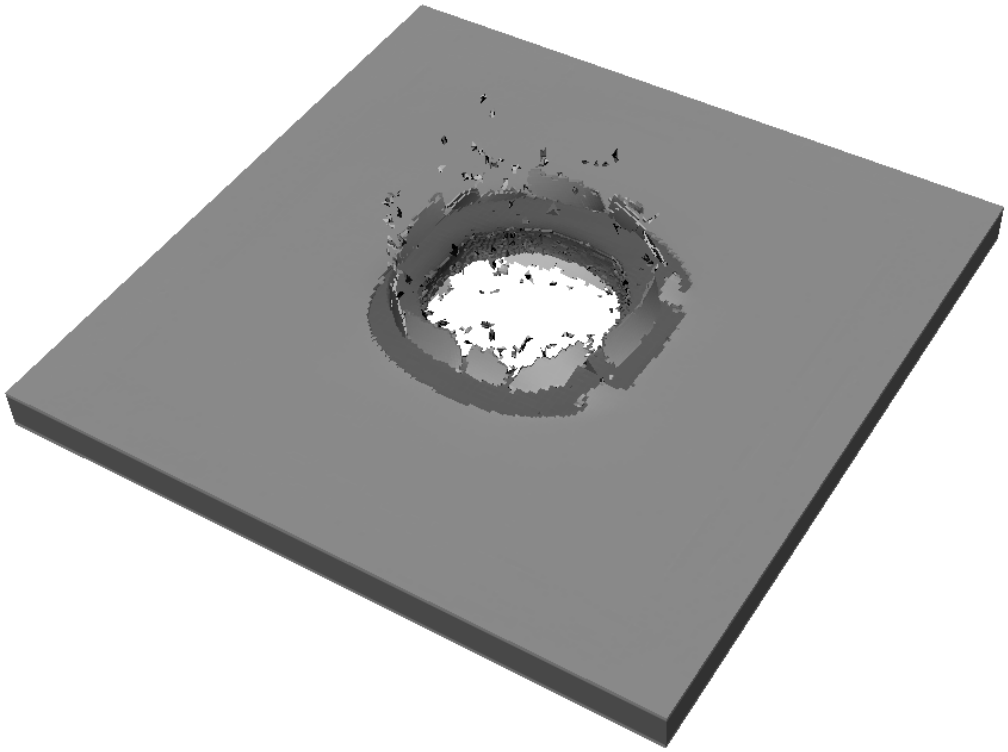

Figure 3. Element plot of the simulation results at 50 microseconds after impact.

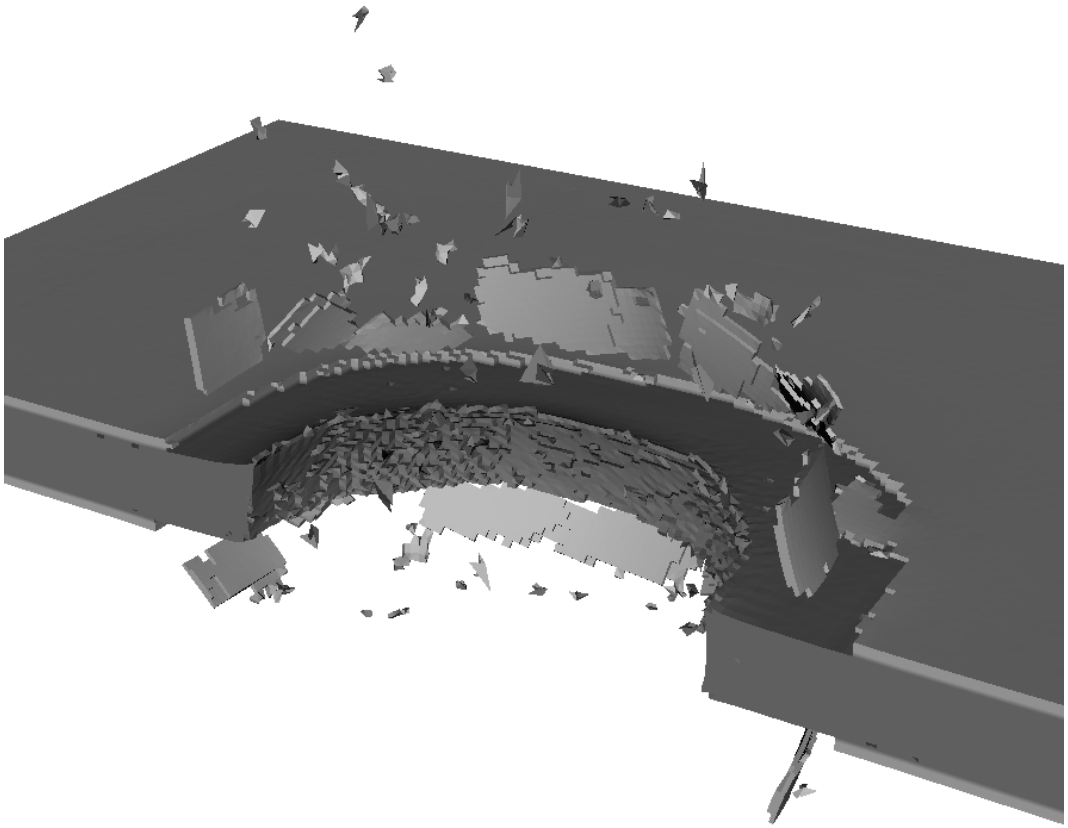

Figure 4. Sectioned element plot of the simulation results at 50 microseconds after impact.

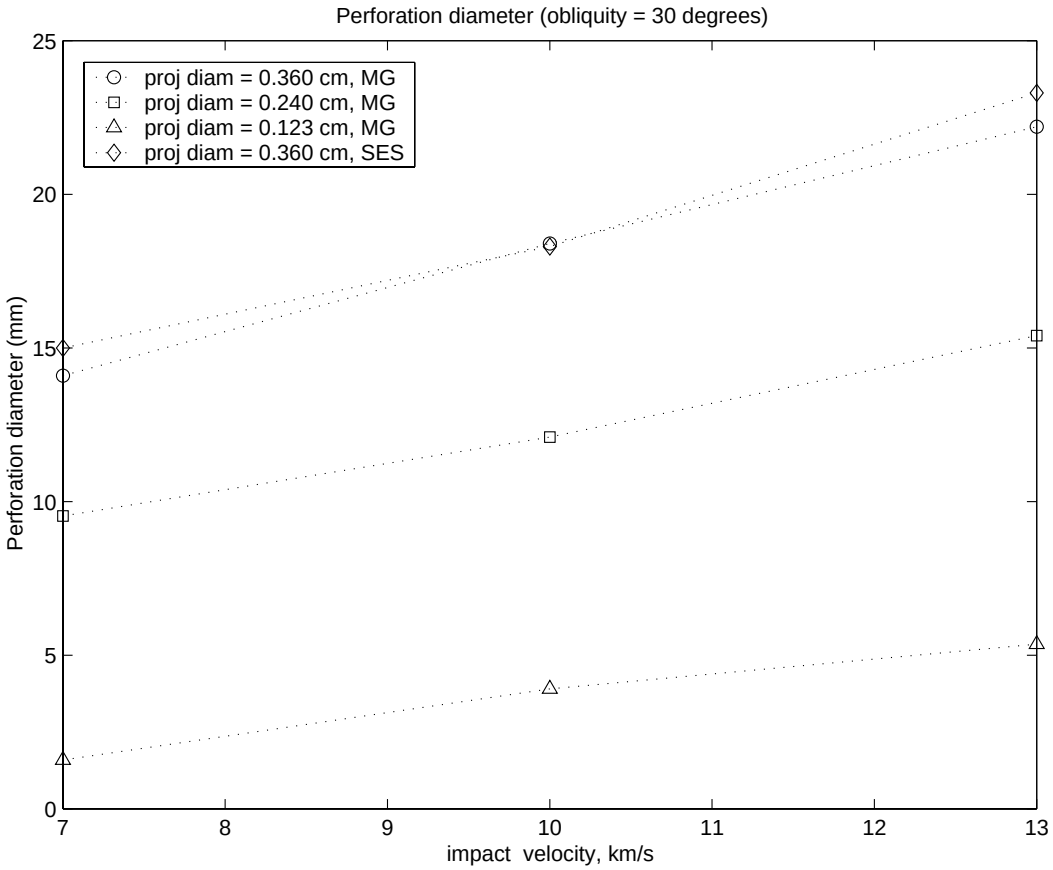

Figure 5. Simulation results for perforation diameter versus impact velocity.

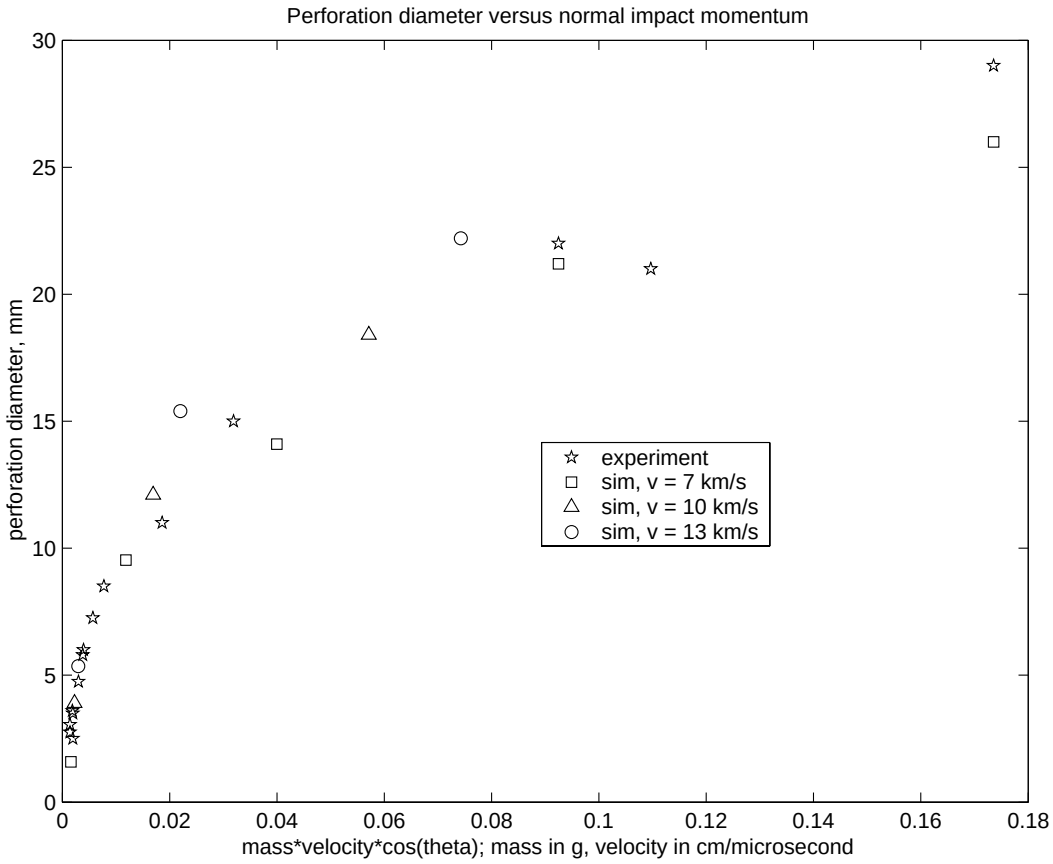

Figure 6. Perforation diameter versus normal impact momentum, for hypervelocity impact in reinforced carbon-carbon.

CHAPTER 7

SIMULATION OF FOAM IMPACT EFFECTS ON COMPONENTS OF THE SPACE SHUTTLE THERMAL PROTECTION SYSTEM

Eric P. Fahrenthold[1] **and Young-Keun Park**[2]

Department of Mechanical Engineering, 1 University Station C2200
University of Texas, Austin, TX 78712, USA

[1]Professor, corresponding author, phone: (512) 471-3064, email: epfahren@mail.utexas.edu
[2]Graduate student

ABSTRACT

A series of three dimensional simulations has been performed to investigate analytically the effect of insulating foam impacts on ceramic tile and reinforced carbon-carbon components of the Space Shuttle thermal protection system. The simulations employed a hybrid particle-finite element method and a parallel code developed for use in spacecraft design applications. The conclusions suggested by the numerical study are in general consistent with experiment. The results emphasize the need for additional material testing work on the dynamic mechanical response of thermal protection system materials, and additional impact experiments for use in validating computational models of impact effects.

NOMENCLATURE

$\mathbf{c}$	particle center of mass position vector
d	element shear damage variable
D	element normal damage variable
$\mathbf{E}^p$	element plastic strain tensor
$\mathbf{f}$	particle damping force
m	particle mass
$\mathbf{p}$	particle translational momentum vector
S	particle entropy
V	thermomechanical potential energy function

INTRODUCTION

The report of the Columbia Accident Investigation Board[1] concluded that the effects of foam impact on the wing leading edge of the Space Shuttle was the most likely cause for the loss of the Orbiter Columbia. Strong evidence in support of this conclusion is provided by a recent series of impact experiments conducted at Southwest Research Institute (SwRI) by a NASA-SwRI-industry team.[2] The current consensus regarding the cause of the accident was not present in the early stages of the investigation, since little experimental data relevant to the accident conditions was available, and since significant lead times were required to prepare and conduct the necessary impact experiments.

Soon after the loss of Columbia an impact analysis team was assembled[3] whose purpose was to investigate analytically the effects of foam impact on components of the Space Shuttle thermal protection system, and to support the conduct of experiments designed to duplicate the impact events observed during launch of the vehicle. This group included NASA, industry, national laboratory, and university participation and employed a variety of numerical methods[4] and computer codes[5] to simulate the impact events of interest. The present paper describes simulations performed using a hybrid particle-finite element method[6] and a parallel computer code[7] to model the impact of foam blocks on both ceramic tile and reinforced carbon-carbon (RCC) components of the Space Shuttle thermal protection system. The simulations described here were performed in advance of the aforementioned experiments and employed the best available material property data for foam, tile, and RCC. The conclusions suggested by the simulations are in general consistent with the results of later experiments, although additional material testing, material modeling, and simulation work is needed to develop a validated computational approach to impact damage assessment for future Space Shuttle applications.

The sections which follow describe the numerical method used in the simulations, the structural and material models assumed for the foam projectiles and the ceramic tile or RCC targets, the computational costs of the simulations, and the results of the numerical study, including suggestions for future research.

NUMERICAL METHOD

In recent research focused on the design of orbital debris shielding, a new numerical method and parallel computer code have been developed for use in spacecraft design applications. This hybrid numerical method employs in tandem nondeforming Lagrangian particles and large strain finite element kinematics,[8] to simulate impact problems involving shock loading, large deformation plasticity, and complex fragmentation dynamics. The method has been implemented in a three dimensional code and validated by comparison with published experiments at impact velocities ranging from one to eleven kilometers per second.[9]

The hybrid method combines the general contact-impact modeling capabilities of particle methods with a true Lagrangian description of strength effects, the latter offered by finite element techniques. It avoids

the tensile instability problems which have hindered the effective use of some particle techniques, as well as the mass and energy discard normally associated with Lagrangian finite element models of material failure. No particle to element mapping is required, since both particles and elements are used throughout the calculation, but to represent distinct physical effects. The particles model all inertia and all contact-impact as well as volumetric thermomechanical response in compressed states, while the elements model tension and elastic-plastic shear. Material failure is represented by the loss of element cohesion, after which particles not associated with any intact element are free to flow under general contact-impact loads.

In the case of spherical particles, the state space model for the particle-element system[8] consists of evolution equations for the particle translational momenta ($\mathbf{p}^{(i)}$) and center of mass position vectors ($\mathbf{c}^{(i)}$)

$$\dot{\mathbf{p}}^{(i)} = -\frac{\partial V}{\partial \mathbf{c}^{(i)}} - \mathbf{f}^{(i)} \,, \qquad \dot{\mathbf{c}}^{(i)} = m^{(i)-1}\, \mathbf{p}^{(i)} \tag{1}$$

augmented by evolution equations for the internal state variables

$$\dot{S}^{(i)} = \dot{S}^{(i)}(\mathbf{p}^{(i)}, \mathbf{c}^{(i)}, S^{(i)}, d^{(j)}, D^{(j)}, \mathbf{E}^{p(j)}) \tag{2}$$

$$\dot{d}^{(j)} = \dot{d}^{(j)}(\mathbf{p}^{(i)}, \mathbf{c}^{(i)}, S^{(i)}, d^{(j)}, D^{(j)}, \mathbf{E}^{p(j)}) \tag{3}$$

$$\dot{D}^{(j)} = \dot{D}^{(j)}(\mathbf{p}^{(i)}, \mathbf{c}^{(i)}, S^{(i)}, d^{(j)}, D^{(j)}, \mathbf{E}^{p(j)}) \tag{4}$$

$$\dot{\mathbf{E}}^{p(j)} = \dot{\mathbf{E}}^{p(j)}(\mathbf{p}^{(i)}, \mathbf{c}^{(i)}, S^{(i)}, d^{(j)}, D^{(j)}, \mathbf{E}^{p(j)}) \tag{5}$$

where $\mathbf{f}^{(i)}$ is a damping force, $m^{(i)}$ is a particle mass, $S^{(i)}$ is a particle entropy, $d^{(j)}$ and $D^{(j)}$ are element shear and normal damage variables, $\mathbf{E}^{p(j)}$ is a plastic strain tensor, i is a particle index, j is an element index, and V is a thermomechanical potential

$$V = V(\mathbf{c}^{(i)}, S^{(i)}, d^{(j)}, D^{(j)}, \mathbf{E}^{p(j)}) \tag{6}$$

The specific functional forms of the thermomechanical potential and the internal state evolution equations depend upon the constitutive assumptions as well as the adopted interpolations for the density and displacement fields. The present work investigated for the first time the application of this method to a relatively low velocity impact regime, in problems which nonetheless involved complex contact-impact, material failure, and fragmentation phenomena difficult to simulate using structural finite element codes.

MATERIAL MODELS

The simulations described here employed simple material models for the foam, tile, felt strain isolation pad (SIP), and RCC, with material properties estimated using the available experimental data. All materials were assumed to be isotropic elastic-perfectly plastic,[10] with an accumulated a plastic strain criterion applied to initiate element failure. The available material data base may be summarized as follows. In support of the Columbia accident investigation, Glenn Research Center[11] and Sandia National Laboratories (SNL)[12] performed mechanical property tests on foam, tile, and reinforced carbon-carbon. Mechanical property tests previously performed on SIP and on SIP-tile combinations are described by Sawyer[13] and Cooper and Sawyer[14] respectively. The relevant thermal properties for polyurethane, tile, SIP, and carbon-carbon materials are provided by Oertel,[15] Banas et al.,[16] Myers et al.,[17] Ohlhorst et al.,[18] and the commercial literature.[19]

Table 1 lists estimated properties for the materials of interest. These values were used (except in the case of the SIP) to perform the simulations described in this paper. The present analysis adopted a yield strength for the tile corresponding to the lowest experimental measurements of Lu et al.[12] In the case of the RCC, the present analysis assumed a yield strength equal to the bending strength measured by Lu et al.,[12] since the failure mode for the RCC panels was expected to be flexure of the panel surface under the foam impact load. At the time the present analysis was performed, the data available to the authors on SIP properties was very limited. As a result the SIP density was underestimated by a factor of 2.3, and the single layer of SIP elements used in the numerical model was assigned the same stiffness properties as the tile. The effect of the underestimating the SIP density was to slightly underestimate the target areal density, and in the present analysis is not considered to be significant. The experiments of Cooper and Sawyer[14] suggest that the stiff SIP elements used here would tend to overestimate the tile damage produced by the foam impact load.

More general models of the dynamic mechanical deformation and failure of the foam, tile, felt, and reinforced carbon-carbon materials are needed. The authors and others are currently engaged in work to develop improved material models, with anisotropy and strain rate dependence significant in some if not all

of these materials.

TILE IMPACT MODEL

Analysis of launch videos, supplemented by computational fluid dynamics studies, suggested that ceramic tiles located on the lower surface of Columbia might have been struck by a block of insulating foam shed from the vehicle's external tank. A series of experiments was therefore planned to measure the impact damage produced by highly oblique foam block impacts on tile arrays similar to those covering the lower surface of the Orbiter wing. Simulations were run in advance of these experiments, to estimate the impact damage. The simulation parameters are listed in Table 2.

In each simulation the target model was composed of a 2 x 4 foot array of tiles, each tile having an areal extent of 6 x 6 inches. The uniform tile thickness matched that in the suspected impact areas, over the main landing gear door and in the nearby wing acreage. In the simulations the tile array was supported by an aluminum plate, whose lower surface was fixed along a circumferential edge strip, the latter with a width of one inch. The strain isolation pad (SIP) which separates the tile and the aluminum wing structure was modeled with a single layer of finite elements, however similar (gap filler) material often interposed between the individual tiles was not modeled. The foam projectile was modeled as a homogeneous hexahedral block. The dimensions, obliquity, and orientation of the foam block at impact were varied between simulations, due to uncertainties in the interpretation of the launch videos, a dependence of the impact obliquity on the vehicle impact location, and a desire to investigate the effect of projectile orientation (roll angle) on impact damage.

Computer resource requirements and some limitations of the research code and preprocessor used here made it necessary to introduce certain geometric approximations. Since available commercial preprocessors do not generate hybrid particle-finite element models, a special preprocessor was employed. The latter code generates solid models composed of uniform hexahedra, and associated ellipsoidal particles, so that an element and particle deletion process was used to introduce the gaps between the tiles. As a result the width of these gaps was overestimated. Combined with the aforementioned neglect of gap fillers, the assumed geometric

model approximates conservatively the structural strength of the actual tile array. A second approximation was introduced in modeling the individual tiles, whose external surfaces are coated in a borosilicate layer, to a depth approximately five percent of the tile thickness. Computer resource requirements precluded modeling of features with such small dimensions, so the tiles were taken to be monolithic with material properties derived from the published strength and stiffness properties of an individual tile.

TILE IMPACT SIMULATIONS

The four tile impact simulations were performed on systems operated by NASA Ames Research Center, and required between three and five wall clock days on 128 or 192 processors of an SGI Origin. The models were composed of over one million particles, with the simulations extending over five or six milliseconds of physical time.

The first two simulations differed only with respect to projectile orientation (roll angle), and modeled the impact of a 1.06 pound block of foam, at a velocity of 700 feet per second, on a tile array similar to those which cover the main landing gear doors. Impact obliquity was five degrees. The simulations showed 12.0 cubic inches of material (0.178 tile volumes) eroded by the long edge impact and 19.6 cubic inches of material (0.290 tile volumes) eroded by the short edge impact. Figures 1 and 2 show the simulation results, including views of the predicted tile erosion. In both these simulations the maximum predicted depth of penetration was approximately one half of the tile thickness. Since the short edge impact appeared to be more damaging under the postulated impact conditions, subsequent simulations (and later experiments) involved foam blocks rotated so as to strike the tile array along the projectile's short edge. Experiments which approximately correspond to these two simulations were later performed by Kerr et al.[2] The first experiment produced three craters with a total volume of approximately 0.1 cubic inches, although much of this damage may have been caused by the unintended impact of a Mylar burst disc used in the compressed air gun which launched the projectile. The second experiment produced no impact craters. Since the aforementioned numerical modeling assumptions minimized both tile strength and tile lateral support while maximizing the stiffness of the SIP layer, the tile impact damage was overestimated. However the eroded volume error was less than

one third of one tile volume, with the damage distributed among several tiles.

The third and fourth simulations considered somewhat more severe impact conditions. The third case assumed a 2.24 pound projectile and a slightly reduced tile thickness (tile thickness varies with position over the lower surface of the Orbiter). The result was an increase in eroded material, to 48.2 cubic inches (0.789 tile volumes) and an increase in the maximum depth of penetration, to three quarters of the tile thickness. These simulation results are depicted in Figure 3. Finally the fourth case considered a lower mass projectile (1.53 pounds), but a slightly higher impact velocity (720 fps) and a more direct impact, with the impact obliquity taken to be thirteen degrees. The tile thickness in the target was increased in order to represent a wing acreage area away from the main landing gear door. The simulation results, shown in Figure 4, predicted erosion of 70.6 cubic inches of material (0.785 tile volumes) and a maximum depth of penetration to the level of the SIP, in one small area. Experiments which approximately correspond to these two simulations were later performed by Kerr et al.[2] The first experiment produced no impact craters. The second experiment produced four craters, each with an areal extent of less than 1.0 square inches (depth not provided). It appears that the aforementioned numerical modeling assumptions again caused the tile impact damage to be overestimated. The eroded volume error was less than one tile volume, with the damage distributed among multiple tiles.

In summary the pretest simulations predicted in the worst case the removal of less than one tile volume of ceramic material, under modeling assumptions which conservatively approximated tile strength properties, the lateral support provided in the tile gap region, and the compliance of the SIP layer. Subsequent testing showed that none of the impact configurations considered here produced significant damage to the target tile array.

RCC IMPACT MODEL

As in the case of the underwing tiles, analysis of launch videos and complimentary computational fluid dynamics work suggested the possibility that Columbia's wing leading edge was subjected to a highly oblique foam block impact. A series of experiments on reinforced carbon-carbon panels was therefore planned to

investigate the effects of such impacts, for panel geometries representative of the leading edge region most likely involved. Prior to these experiments, two simulations were run to estimate the impact damage. The simulation parameters are listed in Table 3.

The target model used in the simulations represented the geometry of wing leading edge panel number six. The limitations of the preprocessor used here again led to certain approximations. A profile for the model cross section was obtained by fitting coordinate data extracted from a CAD model of the actual panel, and assuming a constant RCC wall thickness. This cross section was then extended an axial distance equal to the total panel length, with stiffening ribs added at both ends, similar to those found on the actual part. The upper and lower edges of the panel were held fixed in the simulations. This target model was considered to be generally representative of the strength and stiffness of the actual structure. The simulations assumed that in the RCC elements failure would occur at a plastic strain of 0.01, a relatively brittle failure criterion. The thin silicon carbide coating present on the actual part was not modeled, again due to the high computational cost of simulations which resolve very small scale features. As discussed in a preceding section, the particle-element preprocessor used here produced models composed of uniform hexahedra, so that the curved surface of the RCC panel model was represented with a stairstep geometry.

The starting conditions for the two simulations differed only with respect to projectile orientation (roll angle), one objective of the analysis being to determine the relative severity of impact damage caused by edge and corner impacts. The specified impact point was located a distance of 18.1 inches from the panel edge, measured along the panel arc, and the impact obliquity (14.6 degrees) was specified as the angle between the target surface normal at the impact point and the projectile velocity vector, the latter aligned with the long axis of the foam block. The pitch, roll, and yaw of the projectile were computed so as to match these specifications.

RCC IMPACT SIMULATIONS

The RCC panel impact simulations were performed on SGI Origin systems at NASA Ames Research Center, and required between three and four wall clock days on 128 or 256 processors. The models were

composed of approximately two million particles, with the simulations extending over no more than two milliseconds of physical time. The simulation results are depicted in Figure 5 (corner impact case) and Figure 6 (edge impact case). The first simulation modeled a corner impact and resulted in failure of the panel, with a crack approximately six inches in length developing along the panel surface, normal to the leading edge stagnation line. The second simulation modeled an edge impact and showed greater panel damage, in this case multiple cracks, the largest extending along half the length of the panel and aligned parallel to the stagnation line.

Although the scope of the RCC impact simulation work described here was limited, the results indicate failure of the panel under the postulated foam impact loads. These results are in general consistent with later experiments conducted on Space Shuttle wing leading edge panels. Experiments which approximately correspond to these two simulations were performed by Kerr et al.[2] In the first experiment, a corner impact test conducted on a panel six target at a twenty-one degree obliquity resulted in a crack of length 5.5 inches located at the panel edge and oriented parallel to the stagnation line. In the second experiment, an edge impact test conducted on a panel eight target at a twenty-five degree obliquity resulted in gross failure of the panel surface, producing a 17 inch by 16 inch hole in the panel surface. Comparison of the experiments and simulations is complicated by differences in target geometry and impact obliquity. Since the experiments involved higher impact obliquities, they would be expected to produce more damage than is depicted in the simulations. The first simulation showed a crack similar in size to that observed in the first experiment, although the predicted location and orientation were not correct. The second simulation showed large cracks in the panel surface, at an impact obliquity ten degrees less than that which resulted in gross panel failure in the second experiment. In general the numerical modeling work, which incorporated best case assumptions with regard to RCC strength and ductility, appears to provide good estimates of panel impact damage.

CONCLUSION

The present paper has described a series of pre-test simulations performed to estimate damage produced by external foam strikes on thermal protection system components of the Space Shuttle. The simulations

employed a hybrid particle-finite element technique and a parallel computer code developed for use in spacecraft design applications. The simulation results are in general consistent with experimental results available for this class of problems, and indicate that the numerical method used here is suitable for application in a relatively low velocity regime. The application of this numerical technique to future impact problems would be facilitated by further methods and interface development work, aimed at accommodating complex structural geometries described by a standard CAD data base or a commercial finite element preprocessor.

Several conclusions specific to the operation of the Space Shuttle and the design of future aerospace planes are suggested: (1) additional material testing and constitutive modeling research describing the deformation and failure of thermal protection system materials is needed, (2) numerical methods and code development work is needed to provide a validated computer simulation capability for impact damage assessment, (3) additional, higher resolution simulations should be performed, to investigate the effects of any simplifying assumptions made in the areas of material modeling and structural geometry, and (4) additional impact testing should be conducted, over a wider range of impact conditions, to validate proposed computational analysis techniques.

Research in the suggested areas is already in progress. The authors are currently engaged in work which will allow the hybrid particle-finite element technique used here to model impact on any structural geometry described by a general hexahedral finite element mesh.

Acknowledgments — This work was supported by the Space Science Branch of NASA Johnson Space Center (NAG 9-1244) and by the National Science Foundation (CMS 99-12475). Computer time support was provided by the NASA Advanced Supercomputing Division of Ames Research Center and by the Texas Advanced Computing Center at the University of Texas at Austin.

REFERENCES

1. Report of the Columbia Accident Investigation Board, Volume 1, Government Prining Office, Washington, DC, August 2003.

2. J.H. Kerr, D.J. Grosch, and E.L. Christiansen, "Impact Testing of Large Foam Projectiles," AIAA-2004-0939, presented at the 2004 AIAA Aerospace Sciences Meeting, Reno, Nevada, January 5-8,2004.

3. R.F. Stellingwerf, J.H. Robinson, S. Richardson, S.W. Evans, R. Stallworth, and M. Hovater, "Foam-on-tile Impact Modeling for the STS-107 Investigation," AIAA-2004-0938, presented at the 2004 AIAA Aerospace Sciences Meeting, Reno, Nevada, January 5-8,2004.

4. J.M. McGlaun, S.L. Thompson, and M.G. Elrick, 1990, "CTH: A three dimensional shock wave physics code," International Journal of Impact Engineering, Volume 10, pp. 351-360.

5. K.W. Gwinn and K.E. Metzinger, "Analysis of Foam Impact Onto the Columbia Shuttle Wing Leading Edge Panels Using Pronto3D/SPH," AIAA-2004-0942, presented at the 2004 AIAA Aerospace Sciences Meeting, Reno, Nevada, January 5-8,2004.

6. Fahrenthold, E.P., and Horban, B.A., 2001, "An improved hybrid particle-finite element method for hypervelocity impact simulation," International Journal of Impact Engineering, Vol. 26, pp. 169-178.

7. Fahrenthold, E.P., User's Guide for EXOS, University of Texas, Austin, Texas, 2003.

8. Shivarama, R., and Fahrenthold, E.P., 2004, "An ellipsoidal particle-finite element method for hypervelocity impact simulation," International Journal for Numerical Methods in Engineering, Volume 59, pp. 737-753.

9. Fahrenthold, E.P., and Shivarama, R., 2003, "Extension and validation of a hybrid particle-finite element method for hypervelocity impact simulation," International Journal of Impact Engineering, Volume 29, pp. 237-246.

10. L.E. Malvern, 1969, Introduction to the Mechanics of a Continuous Medium, Prentice Hall, Englewood Cliffs, New Jersey.

11. M. Melis, K. Carney, M. Pereira, D. Revilock, and P. Kopfinger, "Characterization of BX-250 ET Foam Behavior Under Impact in a 1 psi Environment," AIAA-2004-0943, oral presentation at the 2004 AIAA

Aerospace Sciences Meeting, Reno, Nevada, January 5-8,2004.

12. W.-Y. Lu, B.R. Antoun, J.S. Korellis, S. Scheffel, M.Y. Lee, R.D. Hardy, and L.S. Costin, "Material Characterization of Shuttle Thermal Protection System for Impact Analyses," AIAA-2004-0945, presented at the 2004 AIAA Aerospace Sciences Meeting, Reno, Nevada, January 5-8,2004.

13. J.W. Sawyer, "Mechanical Properties of the Shuttle Orbiter Thermal Protection System Strain Isolator Pad," AIAA-1982-0789.

14. P.A. Cooper and J.W. Sawyer, 1983, "Life Considerations of the Shuttle Orbiter Densified-Tile," in Shuttle Performance: Lessons Learned, NASA Conference Publication 2283, pp. 1009-1024.

15. Oertel, G., editor, 1994, Polyurethane Handbook, Hanser/Gardner, New York.

16. R.P. Banas, D.E. Elgin, E.R. Cordia, K.N. Nickel, E.R. Gzowski, and L. Aguilar, 1983, "Lessons Learned from the Development and Manufacturing of Ceramic Reusable Surface Insulation Materials for the Space Shuttle Orbiters," in Shuttle Performance: Lessons Learned, NASA Conference Publication 2283, pp. 967-1008.

17. D.E. Myers, C.J. Martin, and M.L. Blosser, 2000, "Parametric Weight Comparison of Advanced Metallic, Ceramic Tile, and Ceramic Blanket Thermal Protection Systems," NASA TM 2000-210289.

18. C.W. Ohlhorst, W.J. Vaughn, P.O. Ransone, and H.T. Tsou, 1997, "Thermal Conductivity Database of Various Structural Carbon-Carbon Composite Materials," NASA TM 1997-4787.

19. DuPont Corporation, 2001, Technical Guide for Nomex Brand Fiber, H-52720.

Table 1. Material properties

Material property	*Foam*	*Tile*	*SIP*	*RCC*
Young's modulus (psi)	1,360	9,022	220	2.21×10^{6}
Shear modulus (psi)	529	3,510	110	1.04×10^{6}
Reference density (lb/ft^3)	2.15	9.00	12.3	98.6
Yield stress (psi)	42.2	23.9	27.4	14.0×10^{3}
Specific heat (Btu/lbm-degree F)	0.454	0.151	0.315	0.171
Thermal expansion coefficient (1/degree F)	0	2.25×10^{-7}	1.00×10^{-5}	7.28×10^{-7}
Plastic failure strain	1.0	1.0	1.0	0.01

Table 2. Parameters of the tile impact simulations

Parameter	*MLGD 1*	*MLGD 2*	*MLGD 3*	*Wing Acreage*
Projectile velocity (fps)	700	700	700	720
Impact obliquity (degrees)	5	5	5	13
Projectile roll (degrees)	90	0	0	0
Projectile cross section (in)	3.5×11.5	3.5×11.5	5.5×11.5	5.5×11.5
Projectile length (in)	21.25	21.25	28.5	19.0
Tile thickness (in)	1.875	1.875	1.700	2.450
Aluminum plate thickness (in)	0.1875	0.1875	0.2689	0.2720
Simulation time (milliseconds)	5.0	5.0	6.0	5.0
Number of particles (millions)	1.10	1.10	1.42	1.48
Number of processors (SGI Origin)	128	128	192	192
Wall clock time (hours)	76.5	90.1	127	102

Table 3. Parameters of the wing leading edge impact simulations

Parameter	*Corner impact case*	*Edge impact case*
Projectile velocity (fps)	775	775
Projectile dimensions (in)	5.5×11.5×22.8	5.5×11.5×22.8
Projectile roll, pitch, yaw (degrees)	0.0, 17.5, 6.32	30.0, 17.5, 6.32
Impact obliquity (degrees)	14.6	14.6
Panel dimensions (in)	20.5×38.4×21.3	20.5×38.4×21.3
Panel thickness (in)	0.25	0.25
Simulation time (milliseconds)	1.635	2.000
Number of particles (millions)	1.90	1.90
Number of processors (SGI Origin)	128	256
Wall clock time (hours)	96	74

Figure 1. Simulation results for case MLGD 1.

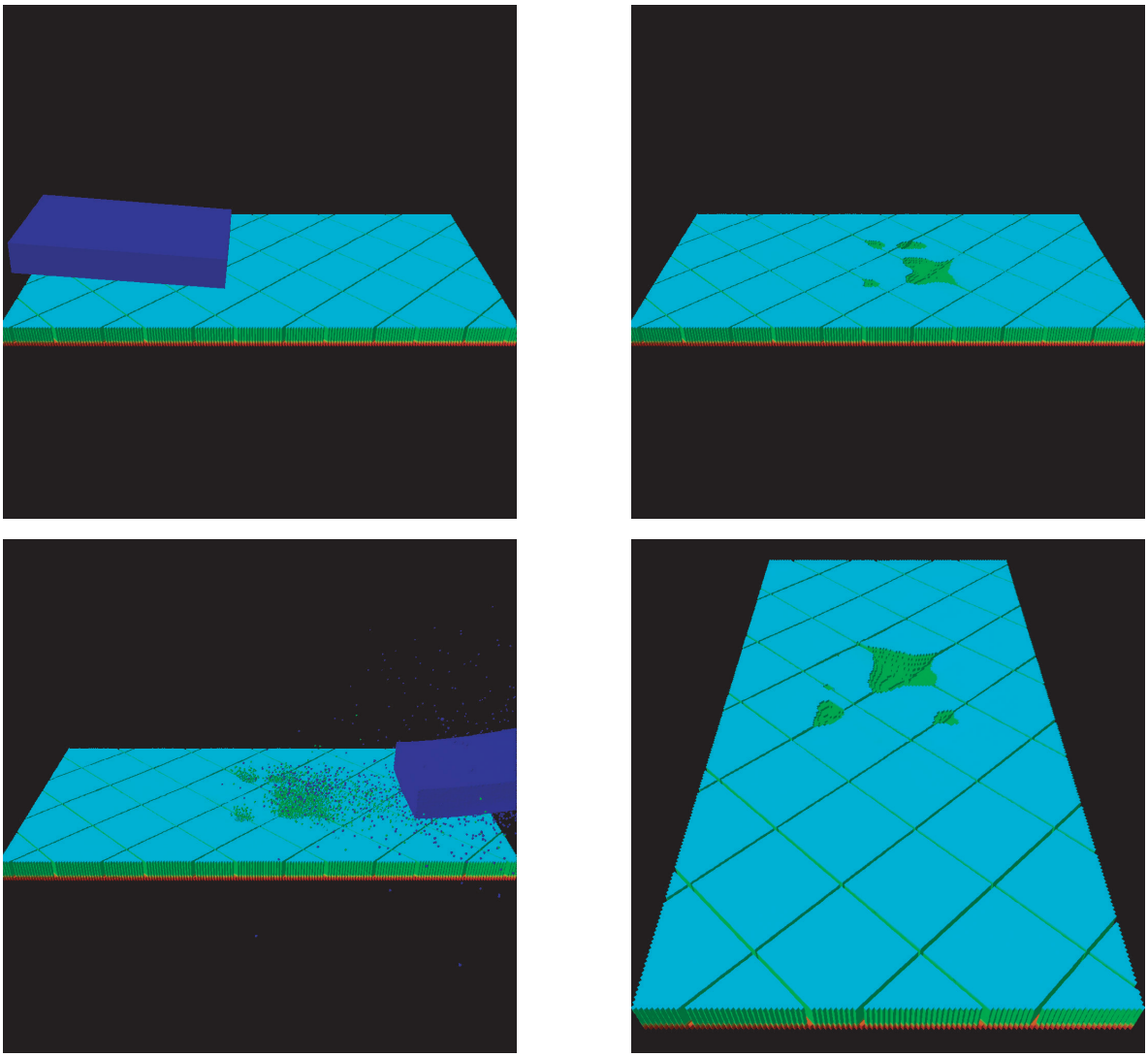

Figure 2. Simulation results for case MLGD 2.

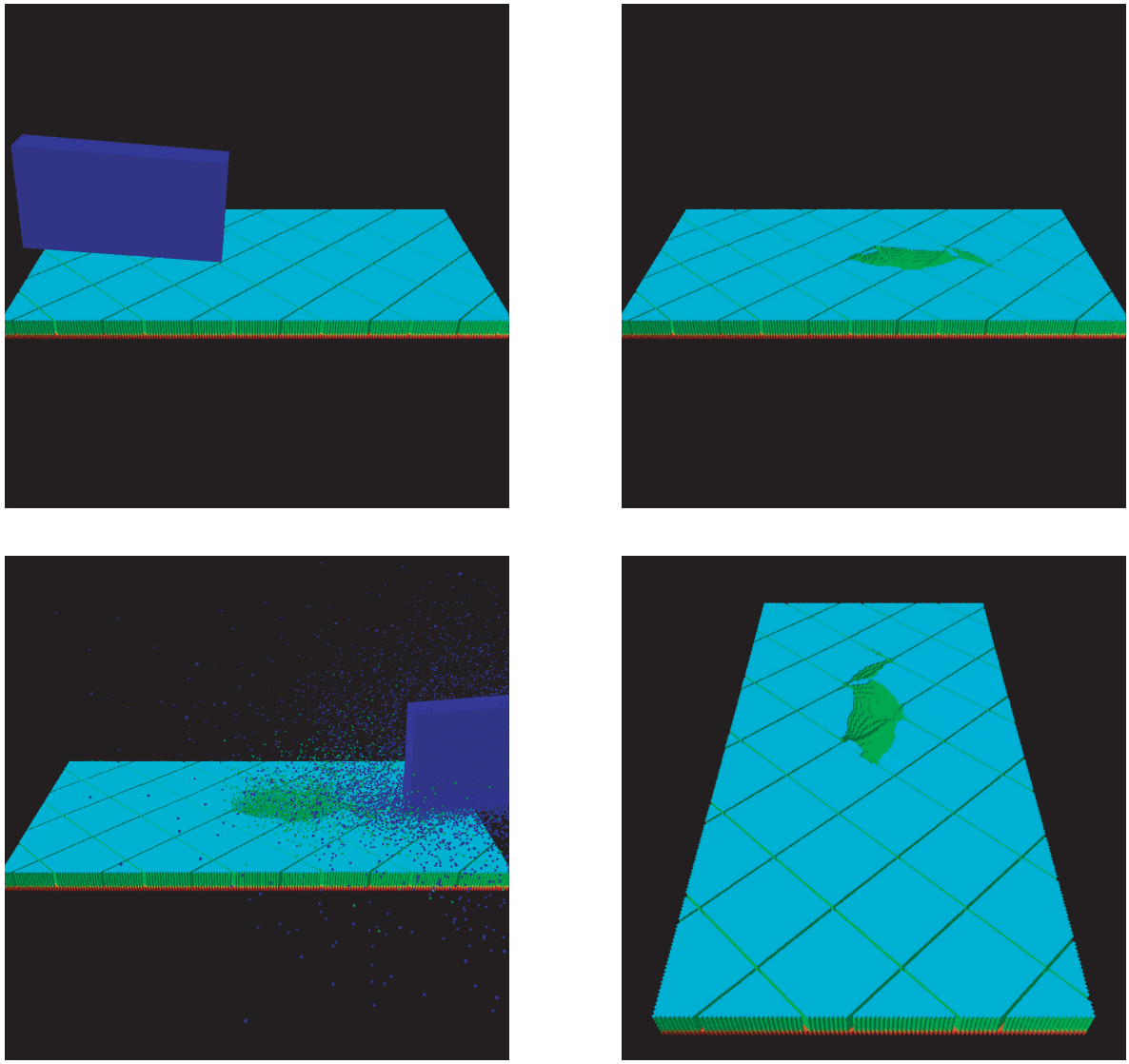

Figure 3. Simulation results for case MLGD 3.

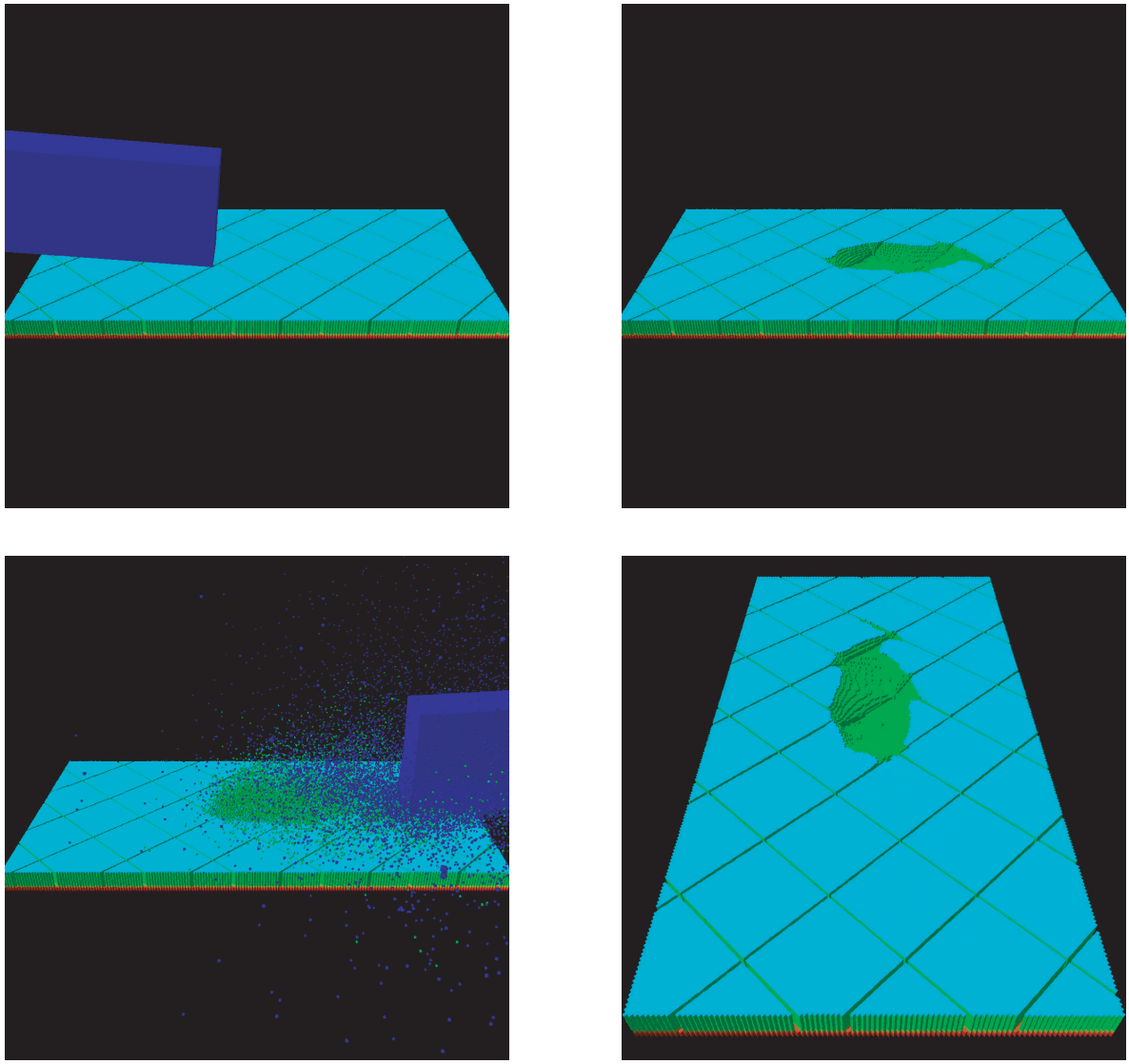

Figure 4. Simulation results for the wing acreage impact case.

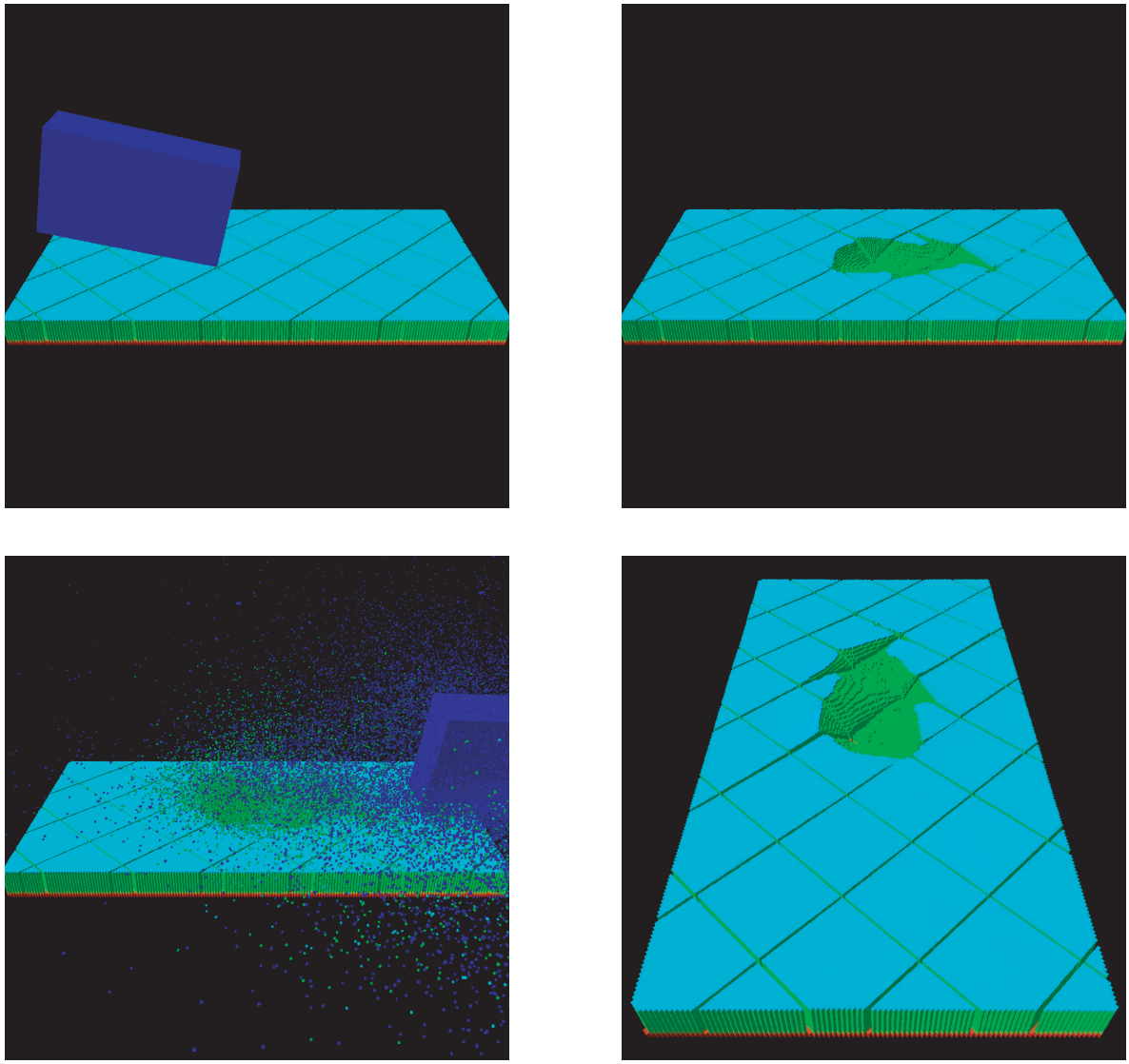

Figure 5. Simulation results for the RCC corner impact case.

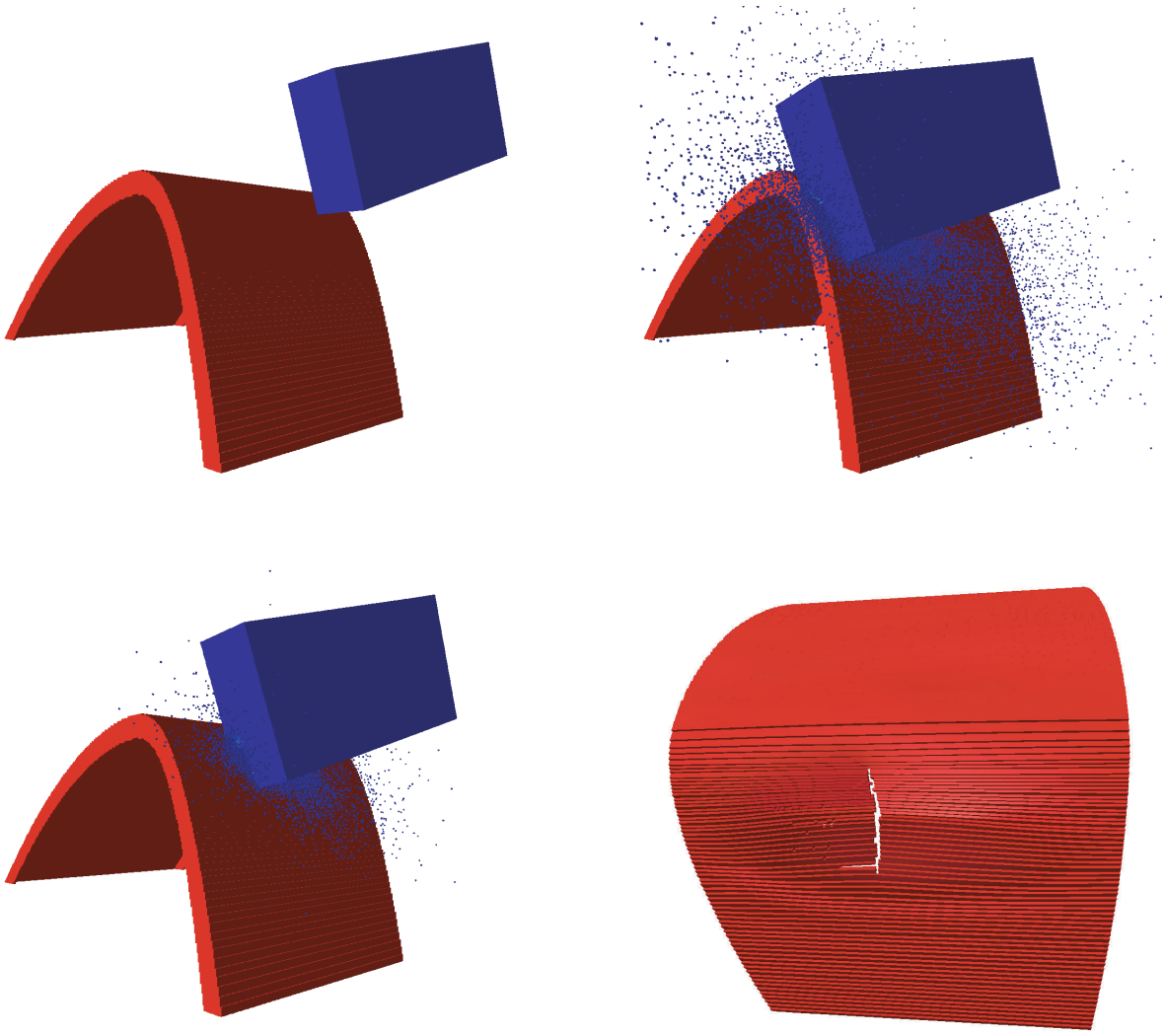

Figure 6. Simulation results for the RCC edge impact case.

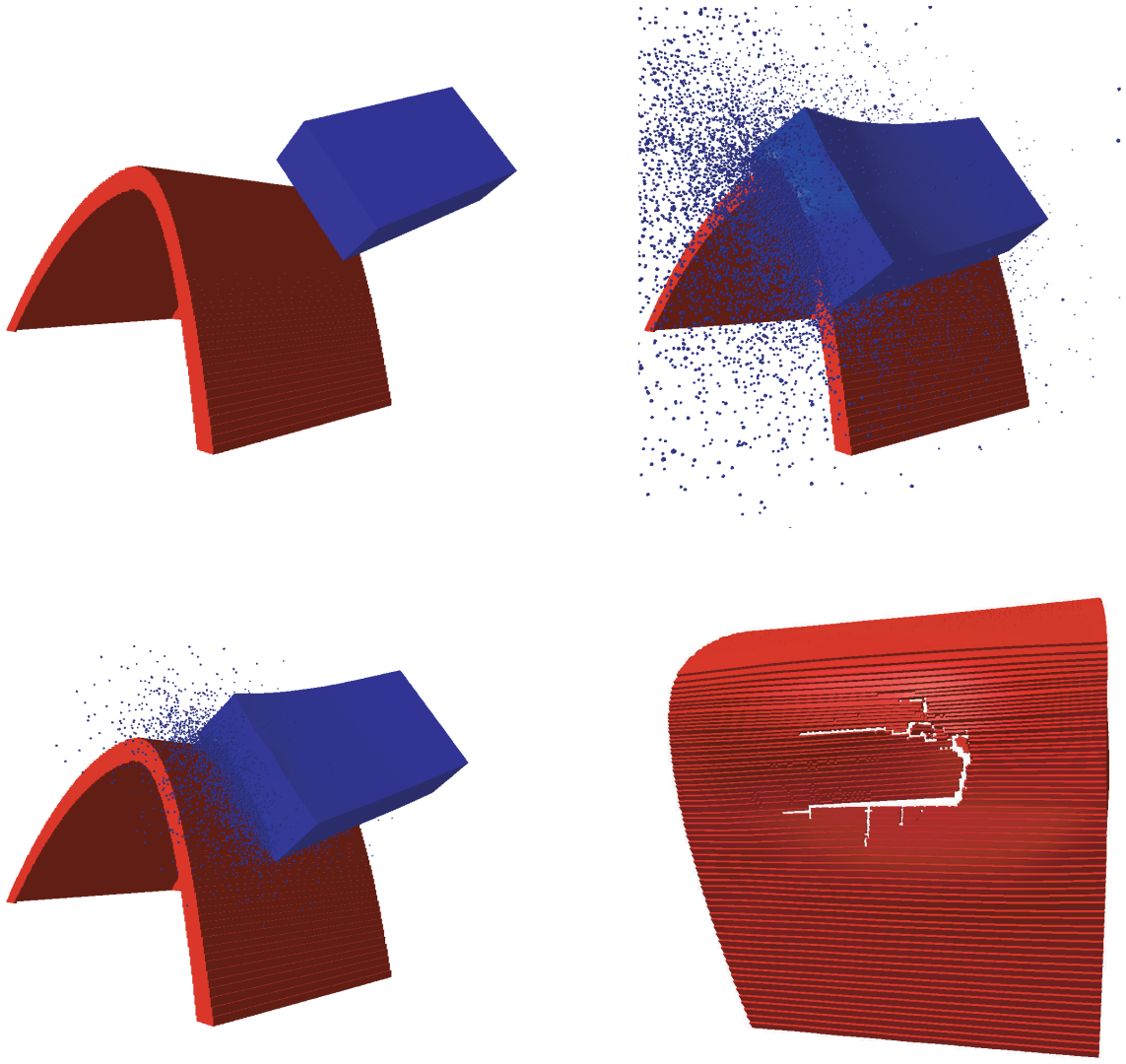

CONCLUSIONS

The design of manned spacecraft for future space exploration missions will require consideration of micrometeoroid and orbital debris impact effects. The debris environment in low earth orbit presents a significant hazard, and has mandated the development of hypervelocity impact shielding for the International Space Station. Although exposure times for the Space Shuttle are much less than that for the space station, the shuttle routinely suffers limited orbital debris impact damage. Hence next generation spacecraft intended to operate, even for limited periods, in low earth orbit must be designed with the orbital debris impact threat in mind. For operations beyond earth orbit, the principal impact threat is due to micrometeoroids. Micrometeoroid impacts typically involve lower particle masses and densities, but higher impact velocities, than those associated with man-made debris in low earth orbit. As a result, shielding designed for low earth orbit projectiles may not be optimal to address the significant micrometeoroid hazard. Although considerable previous work has focused on the hypervelocity impact shielding problem, the development of next generation spacecraft is likely to require significant new experimental and computational research efforts. There are two principal reasons. The first is that the current knowledge base is focused heavily on projectiles, shielding, and spacecraft structures composed of metals. The second is that current experimental methods are not able to address the full impact velocity and kinetic energy range of interest. Although previous experimental and computational studies of debris shielding have involved composites, work to date has served to highlight the increased complexity and cost of experimental and computational impact work involving advanced materials. The research described here on hypervelocity impact effects in reinforced carbon-carbon illustrates a design methodology likely to apply in future development of manned vehicles for space exploration missions. Coordinated experimental and computational efforts will likely be required to address orbital debris and micrometeoroid related design requirements for new space exploration systems.

APPENDIX 1

Simulation Data for Reinforced Carbon-Carbon

Simulation number	D (cm)	v (km/s)	ϕ (deg)	N_e	Equation of state	D_p (cm)	Error (%)	D_c (cm)	Error (%)
200	0.628	7.01	45	8	Mie Gruneisen	2.60	10.3	3.74	15.0
219				8	SESAME 3715	2.65	8.6	3.60	18.2
211				16	Mie Gruneisen	2.66	8.3	4.05	8.0
218				24	Mie Gruneisen	2.67	7.9	4.08	7.3
201	0.478	6.96	30	8	Mie Gruneisen	2.12	3.6	2.95	21.3
220				8	SESAME 3715	1.97	10.5	2.95	21.3
212				16	Mie Gruneisen	2.00	10.0	3.38	9.9
221				24	Mie Gruneisen	2.10	4.5	3.48	7.2
191	0.123	7	30	8	Mie Gruneisen	0.159	na	nr	na
192		10		8	Mie Gruneisen	0.390	na	nr	na
193		13		8	Mie Gruneisen	0.536	na	nr	na
188	0.240	7	30	8	Mie Gruneisen	0.95	na	nr	na
189		10		8	Mie Gruneisen	1.21	na	nr	na
190		13		8	Mie Gruneisen	1.54	na	nr	na
185	0.360	7	30	8	Mie Gruneisen	1.41	na	nr	na
186		10		8	Mie Gruneisen	1.84	na	nr	na
187		13		8	Mie Gruneisen	2.22	na	nr	na
224	0.360	7	30	8	SESAME 3715	1.50	na	2.00	na
223		10		8	SESAME 3715	1.83	na	2.75	na
222		13		8	SESAME 3715	2.33	na	3.17	na

na = not available (no corresponding experiment)

nr = not recorded (accurate coating spall results require $N_e = 16$)

D = projectile diameter (aluminum sphere)

v = impact velocity; ϕ = impact obliquity (normal impact is zero degrees)

N_e = number of elements across the target plate

D_p = perforation diameter; D_c = diameter of the spalled coating region